Alma Mater Studiorum · University of Bologna

School of Science
Department of Physics and Astronomy
Master Degree in Physics

Study of the timing response of SiPM in direct detection of charged particles for the TOF System of ALICE 3

Supervisor:
Prof. Gilda Scioli

Co-supervisor:
Dr. Francesca Carnesecchi

Submitted by:
Bianca Sabiu

Academic Year 2021/2022

Abstract

Silicon PhotoMultipliers (SiPMs) are an established photon detectors of choice in many areas, from LiDAR (Light Detection and Ranging) applications to Time-of-Flight (TOF) medical techniques. In this thesis, SiPMs are studied for their potential application also in direct detection of charged particles. The study showed promising results. Through Cherenkov light emitted in the protection layer above the sensor, the SiPM shows a high detection efficiency and an excellent intrinsic time resolution which improves thanks to the several SPADs signal associated to a single charged particle. The SPAD (Single Photon Avalanche Diode) is the SiPM unit microcell. For a charged particle, more than 6 SPADs may have signals giving a time resolution of around 20 ps together with an increased detection efficiency, if compared with a simple geometrical efficiency. The excellent time resolution of SiPMs reported in this thesis paves the way to their application in different research areas where a high precision timing information is essential: from medical and engineering applications, to experiments in space and multi-purpose detectors at colliders. Indeed, the SiPM represents a possible candidate for the future ALICE 3 experiment at the LHC proposed for Run 5: this experiment, which will study mainly high energy proton-proton and ion collisions, is planned to be a compact multi-purpose detector that features excellent vertexing, tracking and timing capabilities in order to do Particle IDentification (PID). In this contest, a new concept of a TOF and RICH (Ring-Imaging Cherenkov) detectors merged into one could benefit from the SiPM capability of single photon detection and charged track timing response.

Contents

Introduction **5**

1 ALICE 3: a next-generation LHC heavy-ion experiment **7**
- 1.1 ALICE recent upgrades and limits 8
- 1.2 ALICE 3 main physics goals 10
- 1.3 Detector layout 13
  - 1.3.1 Detector technologies 14
  - 1.3.2 Timing layers 14
  - 1.3.3 RICH 17
  - 1.3.4 RICH and TOF as a single detector 17

2 Solid state detectors for timing applications **19**
- 2.1 Silicon detectors 19
- 2.2 Particles through Silicon detectors 21
  - 2.2.1 Charged particles 23
  - 2.2.2 Photons 25
- 2.3 Silicon for timing 26
  - 2.3.1 Timing system components 27
  - 2.3.2 Gain 28
- 2.4 SiPM Silicon PhotoMultiplier 29
  - 2.4.1 AP, APD and SPAD 30
  - 2.4.2 SiPM structure and working principles 31
  - 2.4.3 PDE 34
  - 2.4.4 Noise 35
  - 2.4.5 Signal shape 37
- 2.5 SiPM response to charged particles 39

3 SiPM studies **43**
- 3.1 Detectors under study 43
  - 3.1.1 SiPM studied in July 2022 beam test 45
  - 3.1.2 SiPM studied in November 2022 beam test 45
- 3.2 Preliminary measurements 45
  - 3.2.1 IV curve 46
  - 3.2.2 CV curve 48
  - 3.2.3 Dark Count Rate 48
- 3.3 Beam test studies 50
  - 3.3.1 Experimental setup 50

3.3.2 Signal selection 51
3.3.3 Evaluation of the time resolution 52
3.4 Results: understanding direct detection of charged particles with SiPMs . 54
3.4.1 Crosstalk 55
3.4.2 Time resolution 57
3.5 Results: measurements of the Cherenkov effect in direct detection of charged particles with SiPMs 58
3.5.1 Position scan of single SiPM 58
3.5.2 Signal amplitudes 61
3.5.3 SiPM response at lower beam energies 61
3.5.4 Time resolution 66

Conclusions **72**

Appendix: Cherenkov radiation **73**

Bibliography **75**

Introduction

In this thesis, Silicon PhotoMultipliers (SiPMs), solid state photodetectors made of an array of hundreds or thousands of integrated Single-Photon Avalanche Diodes (SPADs), are studied in direct detection of charged particles. The SiPM is nowadays an established photon detector of choice for a variety of applications, from TOF-PET (Time-of-Flight Positron Emission Tomography) medical diagnostic technique to lifetime fluorescence spectroscopy in biology, from distance measurements through the LiDAR (Light Detection And Ranging) technology to astrophysics applications [1] [2]. All these years, SiPM has always been considered coupled to scintillators in order to detect photons, in particular in Ring-Imaging CHerenkov (RICH) applications or space-born experiments. Nevertheless, recent studies show that SiPMs are able to directly detect charged particles.

As a matter of fact, following a recent paper results [3], a pioneer study is developed in this thesis with the aim of understanding SiPMs behaviour in direct detection of charged particles and evaluating their timing response. Indeed, after its characterization in the Bologna laboratories, the SiPM performance in terms of principle of operation and time resolution is studied for different types of SiPMs with data collected at two different beam tests performed at the CERN T10 beam line.

The analysis starts from the observation of an increased number of firing SPADs when particles traverse the sensor with respect to the usual crosstalk count rate. By virtue of this study, the effect was understood in terms of production of Cherenkov light inside the protection resin. Indeed, on top of the SiPM a layer of epoxy or silicon resin is usually placed to protect the sensor. Next, a detailed study of the response of sensors with different, in thickness and material, resin protection layers was carried out. A benefit of the emission of Cherenkov light in the protection layer is, among others, an improvement of the time resolution for MIPs (Minimum Ionizing Particles) by means of larger signals that are associated to a high number of fired SPADs.

In light of this thesis results, the SiPM, with its excellent time resolution, could be used in direct detection of charged particles. Therefore, the SiPM represents a possible candidate for timing applications without the need of using the device coupled to scintillators. The properties of the SiPM could then constitute a benefit in every field of R&D whenever the time resolution plays a major role, from TOF systems in space to medical and engineering applications.

An example of a possible application of SiPMs used in direct detection of charged particles could be in the contest of the TOF and RICH subdetectors of ALICE 3, a compact next-generation multipurpose detector proposed for Run 5 around 2033 at the LHC [4] to be located where the ALICE experiment is currently installed [5].

The timing layers of ALICE 3 require a time resolution of at least $\simeq 20$ ps in order to be able to do Particle IDentification (PID) i.e. discriminate π/K/p up to 2 GeV/c and hadrons/electrons up to 500 MeV/c. This objective could be achieved with a TOF silicon based detector system that is being developed considering as possible candidates fully-depleted Complementary Metal-Oxide-Silicon (CMOS) Monolithic Active Pixel Sensors (MAPS), Low Gain Avalanche Detectors (LGAD) or SiPMs.

In Chapter 1, the main physics goals addressed by the ALICE experiment at the LHC are presented together with its limits. Consequently, an overview of ALICE 3 physics potential and detector concept, together with the detector layout and the main technologies involved, is presented. Particular attention will be dedicated to the timing layers and the RICH detector.

In Chapter 2, after the explanation of the main features of silicon solid state detectors and different particles interaction mechanisms in silicon, silicon detectors timing applications are described with a focus on the SiPM technology, structure, signal shape, noise and main figures of merit. Moreover, the main results obtained in recent studies with SiPMs directly detecting charged particles are illustrated since they constitute the starting point of this thesis studies.

Chapter 3 goes through the SiPM studies which are at the heart of this thesis. First of all, the type of SiPMs under study produced by FBK (Fondazione Bruno Kessler) are illustrated, together with the prototypes main features. Next, preliminary measurements to characterize the sensors on current, capacity and dark count made in the Bologna laboratories are reported. In the end, the main studies on SiPMs performed at two experimental beam tests at the CERN T10 beam line are reported: the chapter goes through the experimental setups, the methods to select the SiPM signal and to evaluate its time resolution, to the final leading results on the time resolution of the sensors.

Chapter 1

ALICE 3: a next-generation LHC heavy-ion experiment

ALICE 3 experiment concept consists of a compact next-generation multipurpose detector at the CERN LHC which will study the production of heavy-flavour hadrons and of soft electromagnetic and hadronic radiation produced in high-energy proton-proton (pp) and nuclear (AA and pA) collisions [4]. The experiment will be located where ALICE [1] [5] is currently installed at the LHC and will be assembled during Long Shutdown 4 (LS4) starting from around 2033-34, as can be seen in the LHC long term schedule of Figure 1.1. ALICE 3 is planned to be composed of a barrel detector and endcaps with very low material budget. The proposed subdetectors layers consist of different type of silicon sensors. The detector layout features superb pointing resolution, excellent tracking and particle identification over a large acceptance and high readout-rate capabilities.

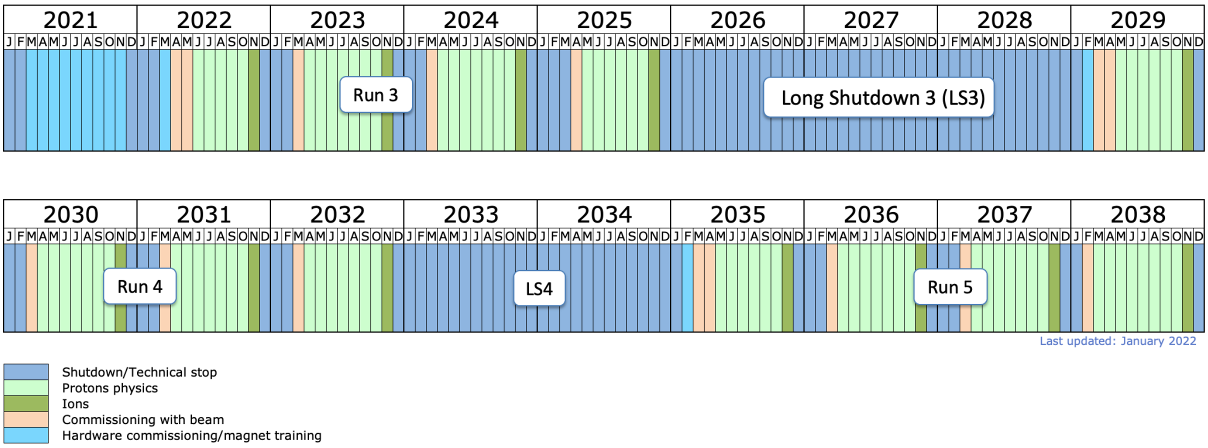

Figure 1.1: Long term schedule of the LHC: during LS3 many updates are planned, while ALICE 3 is planned to be installed during LS4 [6].

ALICE 3 will feature excellent vertexing capabilities over a wide momentum range down to a few tens of MeV/c and will provide PID via a TOF detector which requires a time resolution of the order of $\simeq$ 20 ps. In this contest, the SiPM is being evaluated as a possible technology for the timing layers.

---

[1] A Large Ion Collider Experiment.

In this chapter, ALICE main recent upgrades and limits will be briefly illustrated. Consequently, ALICE 3 detector principal physics goals and improvements, its layout and technologies, with a particular focus on the timing layers, will be described.

1.1 ALICE recent upgrades and limits

The goal of ALICE physics programme is understanding and determining the properties of strongly interacting matter and to discern how they arise from the underlying interactions described by QCD (Quantum ChromoDynamics). A unique experimental access to the highest-temperature and longest-lived QCD medium that is the quark-gluon plasma (QGP) can be provided by collisions of heavy-nuclei which produce heavy-flavour probes at the LHC. In particular, with ultra relativistic heavy-ion collisions, it is possible to recreate conditions similar to those of the early universe.

The ALICE collaboration has just completed a major upgrade programme targeted at the physics of ultrarelativistic nuclear collisions [7]: in particular, during Runs 3 and 4, ALICE, with an increased readout rate from below 1 kHz to 50 kHz in Pb-Pb collisions and a pointing resolution of 5 μm, aims to improve the precision of heavy-flavour production measurements and to measure for the first time the thermal emission of dileptons in heavy-ion collisions covering transverse momenta from ~ 100 MeV/c to 100 GeV/c.

One of the main physics goals of ALICE is the study of heavy quarks propagation and hadronisation [8] [9]. The transport and the thermalisation of heavy quarks, which lead to the QGP hadronisation, can be exploited in two ways: by measuring single-particle momentum spectra of charm and beauty hadrons to very low transverse momenta and by looking at the relative abundances of the different heavy-flavour species, including hadrons containing multiple heavy-flavour quarks.

Heavy charm and beauty quarks, with masses of $m_c \sim 1.3$ GeV and $m_b \sim 4.2$ GeV respectively, are produced in the early stage of the collision on a time-scale shorter than the QGP thermalisation time which is of the order of a few fm/c [10]: therefore, heavy quarks production is limited to initial hard scatterings or gluon splittings on short time scales. The number of heavy quarks is conserved through the QGP evolution. Heavy quarks interact with the constituent of the medium through inelastic (radiative energy loss via gluon radiation) and elastic (collisional energy loss) processes. The interactions between heavy quarks with the QGP are described by transport models in terms of drag and p_T diffusion coefficients: in the limit $p_T \to 0$, elastic scatterings with the QGP give rise to a Brownian motion process that determines the long-wavelength diffusion properties of the QGP. In low-momentum regime, D_s is the drag coefficient. D_s is related to the relaxation time τ_Q for a heavy quark of mass m_Q in a medium at temperature T by

$$\tau_Q = \frac{m_Q}{T} D_s. \tag{1.1}$$

Consequently, because $m_b \sim 3m_c$, beauty quarks approach equilibrium three times slower than charm quarks, thus they provide a better theoretical control of D_s. The latter has been constrained in the recent years to the interval $1.5 < 2\pi D_s T_c < 4.5$ with

$T_c = 155$ MeV/c as the transition temperature of the QGP. This estimate is limited by uncertainty. A more precise estimation of D_s in Runs 3 and 4 from charm-hadron measurements will be performed. However, the inclusion of high-precision data at $p_t \simeq 0$ of beauty mesons and baryons is required.

The hadronisation mechanism belongs to the non-perturbative domain of QCD and a first-principle description of these processes is missing for both light and heavy-flavours. The hadronisation of a final state parton is usually considered independent from the surrounding partons density. However, existing LHC measurements suggest the presence of new hadronisation mechanisms, whereby quarks that are close in phase space can combine into colourless hadrons. In heavy-ion collisions, where partons may travel freely over distances much higher than the hadron sizes and a dense system of partons close to thermal equilibrium is formed, such mechanisms becomes dominant, making the production of heavy-flavour species, including hadrons containing multiple heavy-flavour quarks, more favourable than in pp collisions.

In Runs 3 and 4, these studies will be extended to the charm sector but such measurements will be limited to baryons containing only one charm quark. The improved pointing resolution and readout rate of the upgraded ALICE allows to measure baryon-to-meson ratios in the charm sector, with sufficient precision to disentangle charm transport and hadronisation effects and to constrain transport coefficients of charm quarks in the QGP. With ITS3 upgrade [11] during LS3, ALICE experiment will also perform in Run 4 first measurements with beauty hadrons: beauty quarks are not expected to reach full thermal equilibrium, thus, they provide not only a test of heavy quarks transport, as previously mentioned, but also of hadronisation far from equilibrium. However, the precision of Runs 3 and 4 results in the beauty sector is limited and a new step in pointing resolution, acceptance and event rates is needed.

In the massless limit, QCD Lagrangian is symmetric under chiral transformations between left- and right-handed states. However, the mass spectrum of hadrons indicates that symmetry is strongly broken: lattice QCD calculations show that the deconfinement phase transition takes place at a temperature close to the chiral phase transition. Dilepton ($l^- l^+$ with $l = e, \mu$) production from the medium at temperatures near T_c is sensitive to effects of chiral symmetry restoration through the mesons spectral functions that mediate the interactions in the medium. The prime probe is represented by the $\rho(770)$, whose spectral function broadening has been observed at SPS [12] and is consistent with chiral symmetry restoration. However, an unambiguous way to observe chiral symmetry restoration would be measuring ρ and its chiral partner a_1 mixing impact on the thermal dilepton spectrum. The effect is expected to be in the mass region 0.85-1.2 GeV/c where the vector spectral function would present a pronounced dip in the a_1 mass range, as there is no direct coupling of a_1 to the dilepton channel in vacuum. The expected magnitude of this effect is of the order of 15% with a needed experimental accuracy of 5%: with the current ALICE experiment, this precision is not expected to be reached, as in the mass range above the ρ peak a background due to correlated dileptons that originate from heavy-flavour decays is present.

Electromagnetic radiations is emitted continuously during all phases of the collision with photons and dileptons (virtual photons). Since thermal emission rates increase strongly with the temperature, real and virtual photons measurements are probes of the early stages of the collision [13], thus they provide a constraint on the transport coefficients of the QGP as a function of time and temperature. In Runs 3 and 4, ALICE will perform a first measurement of thermal dilepton emission. ALICE will strongly constrain initial conditions and geometry of the collision, but qualitative steps in the vertex detector performance are needed in order to reduce the expected systematic uncertainties from hadronic decays background.

Despite the wide physics programme covered by ALICE in Runs 3 and 4, some key answers will still remain open: this is where ALICE 3 comes into play.

1.2 ALICE 3 main physics goals

ALICE 3 main goal is to achieve a complete understanding of the phenomenology of QCD matter: to do so, a novel experimental approach is required. Some key examples of the physics areas targeted by ALICE 3 are:

- **High precision beauty measurement**. As introduced in Section 1.1, a connection between parton transport and QGP hadronisation mechanism can be exploited by measuring single-particle p_T spectra of charm and beauty hadrons to very low transverse momenta. It is worth noticing that, while a significant fraction of charm hadrons originate from beauty decays, the beauty sector presents a much cleaner field of study with less feeddown contribution. ALICE 3 would allow to perform high-accuracy measurements of beauty mesons and baryons, as B and Λ_b, down to $p_T = 0$. This calls for very high read-out capabilities combined with secondary verteces and decay chains reconstruction capability far exceeding those of the present ALICE inner trackers.

- **Azimuthal decorrelation of $D\bar{D}$**. Measurements as the correlations in the azimuthal angle $\Delta\phi$ between charm hadron pairs, as $D\bar{D}$, with respect to $\Delta\eta$ would allow to discriminate between the different regimes of in-medium energy loss and provide novel constraints on the mechanism of heavy quarks propagation. The measurements of back-to-back pairs are limited with the current ALICE rapidiy coverage of $|\eta| < 0.9$ but come into reach with ALICE 3: with a $|\eta| < 4$, ALICE 3 would allow to detect back-to-back $D\bar{D}$ with very high efficiency down to very low p_T, pushing the impact parameter resolution down to the technological limit. In addition to this, high signal purity is needed to reduce the background i.e. the ability to operate at rates that significantly exceed ALICE capabitilies.

- **Multi-charm baryons, P-wave quarkonia, exotic hadrons**. The formation of multi-charm baryons via combination of uncorrelated quarks, predicted to be enhanced in AA with respect to pp collisions, would provide a direct window on hadronisation from deconfined QGP: these studies are severely limited by the reliance on hadrons, for which other hadronisation mechanism, like string fragmentation and initial production, are significant. Indeed, an unambiguous access to QGP hadronisation requires a capability to measure the production of particles for which the production by other mechanisms is severely suppressed, by at least 2 orders of magnitude for hadrons with two charm quarks, such as Ξ_{cc}, and up to 3 orders of magnitude for three charm quarks hadrons, such as Ω_{ccc}. To achieve then high statistics, an unprecedented pointing resolution, ultra-low material thickness, a PID over a wide momentum range and high readout rates are needed in order to track all multi-heavy-flavour hadrons decay products. In addition to this, a large acceptance is required, not only for statistics reasons, but also to investigate the dependence of the production of multi-heavy-flavour hadrons on the variation of heavy quark density with η.

The suppression of the production yields of charmonium and bottomonium in heavy-ions collisions with respect to pp or pA ones represents another experimental signature of deconfined quarks and gluons: this because the attractive force between a q and an $\bar{q}$ in the QGP medium weakens via a Debye-like screening, possibly leading to a dissociation of the bound state. These can then travel freely and form quarkonium states via regeneration of heavy q-$\bar{q}$ pairs produced in independent hard scatterings. In particular, the access to P-wave (L=1) states, like χ_c and χ_b, would provide stronger constraints on the spectral properties of bound states in the QGP and would allow, comparing S-wave and P-wave states, for a precise characterization of the early-time evolution of relativistic heavy-ion collisions. ALICE 3 is planned to target the reconstruction of L=1 quarkonium states with ability to go down to $p_t = 0$ and excellent performance for low energy photons, enabling accurate measurements of $\chi_c \to J/\Psi\gamma$ and $\chi_b \to \Upsilon\gamma$ in pp and heavy AA collisions over the widest kinematic range at the LHC.

The study of "exotic" hadrons is also a goal for ALICE 3 which aims to measure the production of $\chi_{c1}(3872)$ in Pb-Pb collisions at energies down to $p_T \lesssim$ 5-6 GeV/c, a region not accessible with other LHC experiments. This requires a muon identification down to $p_T \sim 1.5$ Gev/c at $\eta = 0$ and a high efficiency in detection of hadronic decay products in a large η acceptance.

- **Electromagnetic radiation**. In order to access to the full time evolution of fundamental QGP transport parameters, hence their temperature dependence, a complete study of the azimuthal asymmetry of the production of dileptons (virtual photons) as a function of their p_T and their mass is needed. The measurements of photons and dileptons from thermal radiation has low rate compared to hadronic processes: ALICE 3 provides improvement in these measurements by combining a very thin and light tracker to minimize the background from photon conversion. Thermal radiation of real photons is measured via conversion in the tracking system and an electromagnetic calorimeter. The low p_T capabilities of ALICE 3 enable a precise determination of the decay photon background leading to a reduction of systematic uncertainties.

- **Chiral symmetry restoration**. As already explained in Section 1.1, the deconfinement phase transition is expected to be accompanied by a partial restoration of chiral symmetry leading to a modification in the dilepton spectrum of ρ. High statistics and low-background capabilities are here essential and are addressed with ultra-low mass detectors and very high resolution vertexing capabilities.

- **Ultra-soft photons**. The measurement of ultra-soft electromagnetic radiation in the region of 1 MeV/$c < p_T <$ 100 MeV/c is of primary interest as in quantum field

Observables	Kinematic range
Heavy-flavour hadrons	$p_T \to 0$, $\lvert\eta\rvert < 4$
Dielectrons	$p_T \approx 0.05$ to 3 GeV/c, $M_{ee} \approx 0.05$ to 4 GeV/c^2
Photons	$p_T \approx 0.1$ to 50 GeV/c, $-2 < \eta < 4$
Quarkonia and exotica	$p_T \to 0$, $\lvert\eta\rvert < 1.75$
Ultrasoft photons	$p_T \approx 1$ to 50 MeV/c, $3 < \eta < 5$
Nuclei	$p_T \to 0$, $\lvert\eta\rvert < 4$

Table 1.1: Key physics object and kinematic ranges of interest for ALICE 3 [4].

theories the production of these photons is linked to the so called "soft-theorems", in particular Low's theorem [14], which states that it is possible to relate hadron momenta produced in a high energy collision to the number of produced soft photons. Until now only soft photons energies up to 1 GeV have been exploited because measurements require very high statistics and very low background. A tracker with extremely low material budget to minimize photon conversion, a very high pointing resolution to reject photons coming from the decays of heavy-flavour particles and a specially optimized detector in the forward direction to exploit the longitudinal boost at $3 < \eta < 5$, as the one proposed for ALICE 3, could address this uncharted physics area.

An overview of the key physics objects and the respective kinematic ranges of interest for ALICE 3 is reported in summary in Table 1.1: as previously mentioned, to pursue such a rich physics programme, a novel experimental approach should be adopted. With this aim, ALICE 3 features high-speed silicon tracker with very high resolution of $\sim$ 2 μm/p [GeV/c], minimum mass very close to the interaction point and four times the pseudorapidity coverage of the current ALICE. An ultimate pointing resolution is required to reconstruct secondary vertices and decay chains, but also to reject heavy-flavour background for di-electron measurements.

ALICE 3 will allow to study pp and AA collisions at 20-50 higher luminosities than those achievable with the current ALICE detector. So far, the LHC has operated with Pb ions, that, while they provide the largest possible collision system with strongest QGP effects, have limited luminosity. Lighter ions, which are predicted to be used in the following years, because of their lower charge allows the injection of bunches with higher intensity thus providing higher nucleon-nucleon luminosities. This increase in luminosities enables ALICE 3 physics programme. To meet the needs of this programme, the experiment should be operated in pp collision at an instantaneous luminosity of $L = 3.0 \times 10^{32}$ cm^{-2} s^{-1} and an integrated luminosity per month of operation of $\mathcal{L}_{pp}^{\text{month}} \sim 0.5$ fb^{-1}. For the heavy-ion programme, Runs 5 and 6 will allow to study more than five times the nucleon-nucleon luminosity available with Pb-Pb collisions in Runs 3 and 4: in the most challenging scenario of Pb-Pb collisions at $\sqrt{s_{NN}} = 5.52$ TeV, ALICE 3 will deal with a luminosity integrated per month of operation of the order of $\mathcal{L}_{AA}^{\text{month}} \sim 5.6$ nb^{-1}.

1.3 Detector layout

ALICE 3 experimental apparatus consists of a barrel, covering the pseudorapidity region of $|\eta| < 1.4$, and two end-caps, which extend the rapidity coverage to $|\eta| < 4$. The detector has a compact layout with radial dimension of ~ 1.2 m and longitudinal dimension of ~ 4 m. A view of the experiment is reported in Figure 1.2. The apparatus is embedded in a solenoidal superconducting magnet whose field of 2 T ensures high tracking efficiency at a few tens of MeV/c transverse momenta while maintaining good resolution ($\sim 2\%$) at high transverse momenta (~ 30 GeV/c).

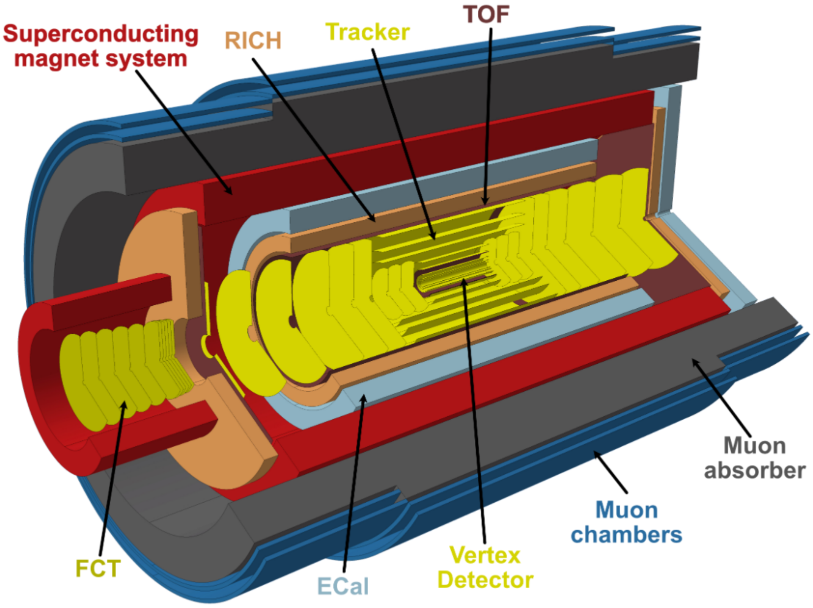

Figure 1.2: ALICE 3 detector concept [4].

The tracker is installed in the volume of 80 cm radius and ±4 m lenght around the interaction point and consists of an inner (vertex) layer and an outer tracker part. ALICE 3 vertexing and tracker system will consist of MAPS sensor that will be complemented by PID detectors TOF and RICH, all housed in a superconducting magnet system. In order to achieve the required pointing resolution, a rectractable inner layer is designed to be placed at just 5 mm from the interaction point during data taking at collision energy. The retractable vertex detector is made of 3 barrel layers and 2×3 forward disks mounted inside a secondary vacuum with a material budget to reduce multiple scattering on the first layer of only 0.1% of a radiation length, X_0, and a position resolution of 2.5 μm. The outer tracker will consist of 8 barrel layers and 2×9 forward disks. The outer tracker target 1% of X_0 per layer and features a position resolution of 10 μm. The power consumption predicted for the vertex and the tracker are respectively of 70 mW cm^2 and 20 mW cm^2. The maximum radiation load per year will be about 10^{15} 1 MeV n_{eq}/cm^2 on the first vertex layer. A superconducting solenoidal magnet will provide a field of 2 T which leads to a p_T resolution of about 0.6% at mid-rapidity and $\sim 2\%$ at $|\eta| = 3$.

The tracker is complemented by systems for PID whose exact specifications are still in their R&D phase: a TOF detector, a RICH detector, an ECal (Electromagnetic Calorimeter), a Forward Conversion Tracker (FCT) and a Muon Identifier are employed.

In the following sections, the first two detectors will be explained with more details.

The reconstruction of photons with very low transverse momenta, down to 1 MeV/c, could be achieved with the tracking of $e^{\pm}$ pairs from photon conversion with the FCT, an array of silicon pixel disks installed in the forward direction at $3 < \eta < 5$ and housed in a dedicated dipole magnet. For the identification of muons, a steel-absorber of 70 cm is installed with two layers of muon detectors to detect and match the tracks in the tracking pixel system.

1.3.1 Detector technologies

ALICE 3 vertexing, tracking and timing detectors will be based on ultra-thin silicon detectors technology. Most sensor requirements may be met with technologies available today but significant R&D phase is required in several areas from here until 2033.

At the heart of ALICE 3 there is charged particle reconstruction based on a silicon pixel tracker arranged in a barrel and forward disks. The layers of the tracker are entirely based on CMOS MAPS transistor technology: these solid-state imaging devices show very good performance in terms of functionality, power, radiation hardness and rate capability [15]. Continuous improvement in the technology, aiming at reducing the dark current and improving the electronic noise, have made CMOS sensors largely available nowadays [16]. CMOS MAPS technology features a high integration density, a reduction of MAPS thickness to values of 20-40 μm - at which the silicon chips become flexible - and the possibility to develop wafer size MAPS with an area up to 20×20 cm^2 [17]. Indeed, the retractable vertex detector inside the beam pipe is planned to have an unprecedented material budget of only $0.1\% X_0$ per layer with pixel sensor area of about 10×10 μm^2 and position resolution of 2.5 μm. The sensors in the most exposed region of the vertex detector must be able to read out average hit rates of 35 MHz cm^{-2}. The outer tracker (placed outside the beam pipe) has a material budget of $1\% X_0$ for each layer, pixel pitch of about 50 μm and spatial resolution of about 10 μm. In the outer tracker, the expected rates are of the order of a few kHz cm^{-2}.

1.3.2 Timing layers

In order to reconstruct heavy-flavour decays, the timing layers should provide hadron π/K/p separation for transverse momentum up to a few GeV/c and hadrons/electrons discrimination up to 500 MeV/c. These requirements are foreseen to be met with three TOF layers:

- a TOF layer outside the tracking detector at a radius of 85 cm (bTOF2) with 20 ps time resolution;
- an inner TOF (bTOF1) at 20 cm, for particles below 300 MeV/c which do not reach bTOF2, with again 20 ps time resolution;
- TOF disks in the forward direction at about 0.5-1.5 m from the interaction point.

The simulated response of the barrel TOF systems for simulated Pb-Pb events in a magnetic field of 2 T is reported in Figure 1.3: due to the larger occupancy, the fake hit association is larger for the bTOF1 causing an increase on the background due to track-TOF mismatch. The momentum thresholds for the particle species are visible as well as the effect of the improved momentum resolution.

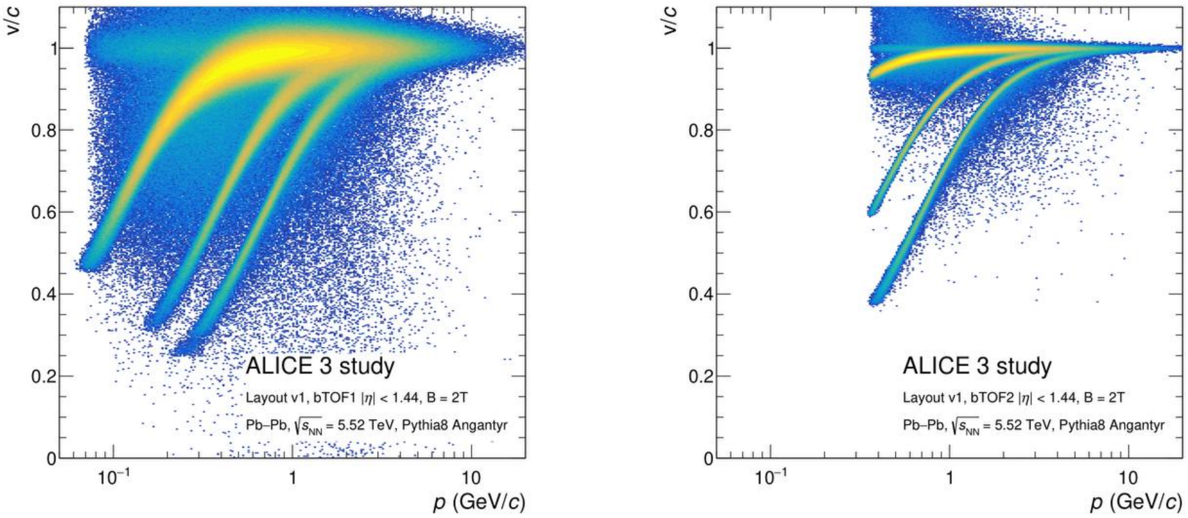

Figure 1.3: Simulation of the momentum dependent distribution of the particle velocity in bTOF1 (left) and bTOF2 (right) in Pb-Pb collisions with B=2 T configuration [4].

The main stringent need for all TOF layers is the achievement of a time resolution of the order of 20 ps - including also the front-end and readout electronics - in order to achieve the required PID. In Figure 1.4 the separation power $n_{\sigma_{TOF}}$ over a 1 m track length, about the distance from the beam pipe of the bTOF2, as a function of momentum is shown with respect to three different time resolutions σ_{TOF}: if the goal of $\sigma_{TOF} = 20$ ps is achieved, π/K separation at 3σ will be performed up to 2.6 GeV/c and K/p separation up to 4 GeV/c [18].

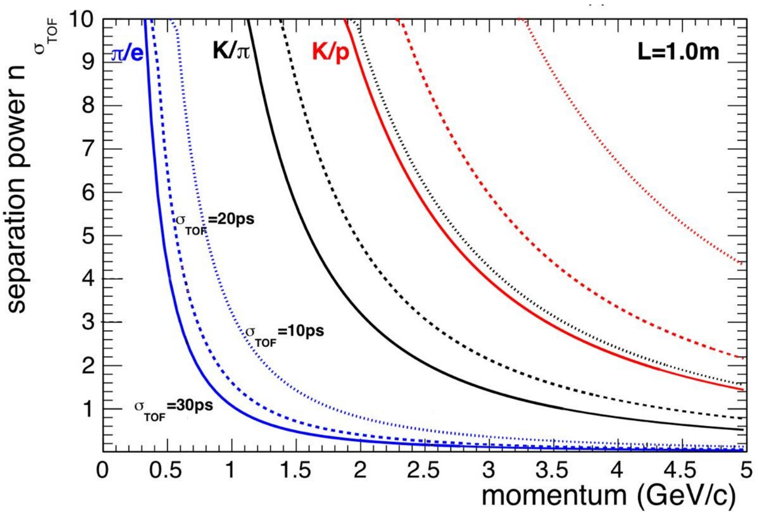

Figure 1.4: Simulation of the separation power in terms of σ as a function of the momentum for different particles in the ALICE 3 bTOF2: at same separation power, with decreasing intrinsic TOF resolution PID is possible for higher momenta [18].

The main TOF specifications for the bTOF1, the bTOF2 and an additional Forward

Parameter	bTOF1	bTOF2	Forward TOF
Radius (m)	0.19	0.85	0.5-1.5
Surface (m^2)	1.5	30	14
Granularity (mm^2)	1×1	5×5	1×1 to 5×5
Hit rate (kHz/cm^2)	74	4	122
NIEL (1 MeV n_{eq}/cm^2)/month	1.3×10^{11}	6.2×10^{9}	2.1×10^{11}

Table 1.2: ALICE 3 timing layers specifications [4].

TOF disks are given in Table 1.2 where the NIEL is Non-Ionizing Energy Loss scaled to an equivalent reference value of 1 MeV neutron damage. Here the NIEL is considered in the worst case of pp collisions at an instantaneous luminosity of $L = 3.0 \times 10^{32}$ cm^{-2} s^{-1}. For all the TOF layers, the key requirements are a material budget of the order of $1\%X_0$-$3\%X_0$ and a power density of 50 mW/cm^2. The physical cell size of the layers will be decided based on the sensor capacitance and related noise.

The main challenges of the timing layers are at the sensor level but also at the sensor to front-end interfaces: to make realistic assessments and appropriate choices, sensor simulations are under development. There are three different candidate technologies currently under study for the TOF silicon surface: fully-depleted CMOS MAPS sensors, Low-Gain Avalanche Diodes (LGAD) and Single Photon Avalanche Diodes (SPADs).

Fully-depleted CMOS sensors, with small pixel size, low noise and low power consumption, could provide an optimal coverage with just a single layer. Good timing performance can be achieved only with fast charge collection i.e. fully-depleted sensors: nevertheless, their time resolution, up to now of the order of 100 ps with 200 μm of thickness, is compromised by non-uniform electric fields and needs to be improved significantly with dedicated R&D. A promising solution may be the introduction of a thin gain layer inside the CMOS sensor, as it is done in LGADs, to increase the signal-to-noise ratio i.e. they would become CMOS LGADs. The timing performance of a fully-depleted MAPS will result from the optimization of the sensor thickness and collection electrode area.

LGADs, which have already been developed for the upgrades of ATLAS [19] and CMS [20], are silicon avalanche pad detectors based on Avalanche PhotoDiodes (APD) and offer excellent time resolution of $\sim$ 30-20 ps. LGADs exploit internal gain through the addition of a highly-doped p-layer close to the n-p junction to create a high electric field. They work below their breakdown voltage resulting in a lower cross-talk, easier segmentation and lower dead time. Thinner sensors are performing better, however, since this means a higher detector capacitance, the noise also increases: an optimization between detector capacitance, gain and power consumption needs to be pursued. State-of-the-art LGADs are produced on sensor-grade wafers and require dedicated readout electronics so LGADs are considered now a fall-back solution. The option of realising a monolithic LGAD sensor using a CMOS process can be addressed as the CMOS MAPS with internal gain described above.

SPADs in an array configuration in SiPMs could represent other candidates for the TOF layers. More details on SPADs and their development for SiPMs will be given in Chapter 3, in particular in Section 2.4.1 and Section 2.4.2. Indeed, the behaviour and timing response of the SiPM are the objects of this study. It is worth noticing that also SPADs fabricated in CMOS technology could be developed as a monolithic solution, although the use of a single layer is less obvious because of dark count, i.e. the sensor firing in absence of photons, and fill factor.

1.3.3 RICH

Cherenkov radiation can be used to extend the PID to momenta out of reach for the outer TOF: the refractive index of the radiator, which determines the range of measurable p_T, ensures continuity in the measurements. For this reason, a 2 cm aerogel tile of $n = 1.03$ with an expansion gap of 20 cm, relying on proximity focusing, could be implemented. In the forward region a smaller refractive index will be adopted to account for the Lorentz boost. The predicted resolution of the Cherenkov angle is about 1.5 mrad.

The RICH, placed behind the TOF, would extend the TOF limit of 500 MeV/c e/π separation to 2 GeV/c, the charged π/K separation of 3σ up to 10 GeV/c and K/p up to 16 GeV/c. In Figure 1.5 the simulated 3σ separation in terms of p_T of the barrel TOF and the RICH detectors for Pb-Pb events as a function of rapidity η is shown.

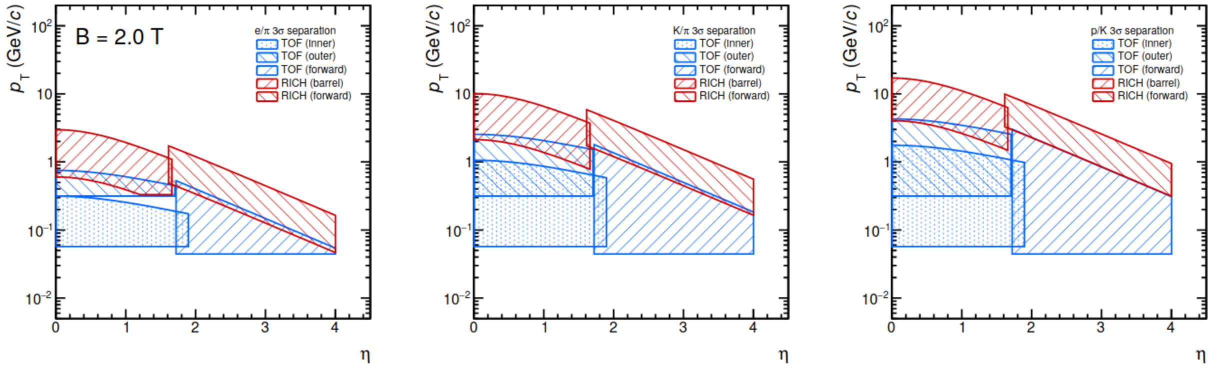

Figure 1.5: Analytical calculations of the $\eta - p_T$ regions in which particles can be separated at 3σ for ALICE 3 PID systems with 2 T magnetic field [4].

1.3.4 RICH and TOF as a single detector

A new idea, starting from the first studies of SiPMs in direct detection of charged particles [3], has emerged together with this thesis studies: the possibility to combine the PID via the Cherenkov angle and the timing information from the outer TOF merging them into a single detector to enlarge sensitivity and precision of the two detectors. As the SiPM can detect both MIPs and single photons with high efficiency and good timing, it represents a valid candidate for the two subdetectors.

The timing properties of TOF detectors based on Cherenkov light would benefit from this type of emission because of its faster emission time: this is of the order of 1 ps with respect to about 2 ns of scintillation [21]. A reduction in time fluctuations of photon emission results in a better time resolution. Further more, SiPM application to RICH counters, thanks to SiPM technologies developed on purpose to detect Cherenkov light, has shown the first rings [22] [23]. In Figure 1.6 a possible implementation of RICH and

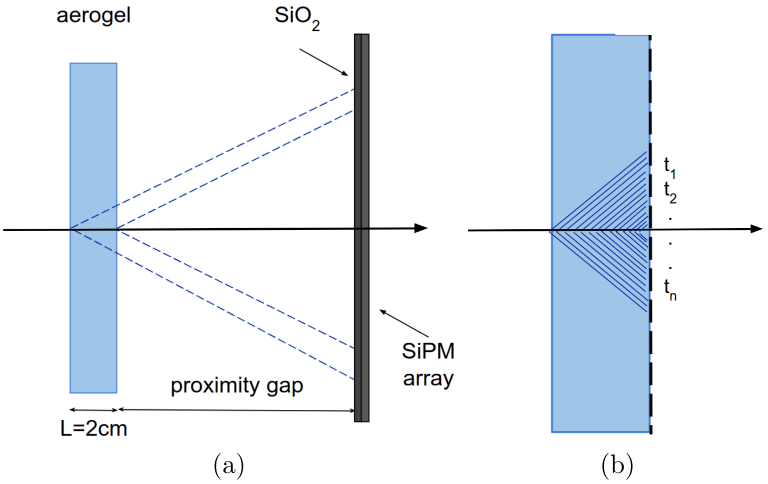

Figure 1.6: (a) Possible setup of a combined RICH and TOF detector; (b) the SiPM array with time information for every sensor.

TOF with SiPMs as a combined detector is shown.

The advantages of merging the RICH and TOF detectors are many: from a performance improvement of TOF by having an increased distance to do PID which would go from about 0.85 m to 1.1 m, to a smaller Cherenkov angle resolution by increasing the proximity gap from 20 to 25 cm. In addition to this, a reduction of cost and material budget would be possible: if separated, TOF and RICH surfaces would consist of about 70 m^2, while, if merged into a single detector, would require the construction of an area of about 30 m^2. A SPAD-based system could also allow merging the TOF and RICH readouts.

Chapter 2

Solid state detectors for timing applications

Solid state detectors are ionization chambers based on semiconductors material, mainly Si (silicon) and Ge (germanium). Solid state detectors are widely used in High Energy Physics (HEP) and in many other fields, like in medical and engineering technology areas, as they are excellent light and charged particles detectors. Due to silicon large availability and the possibility to operate it at room temperature, silicon applications have been studied for years making it the standard material adopted for experiments of HEP.

In this Chapter, after a brief explanation of silicon solid state detectors and of the main interactions of different particles in silicon, the specific case of silicon detectors application to timing is reported. In particular, the SiPM device is introduced: the SiPM is a silicon detector optimized for light detection which is traditionally used coupled to scintillators or Cherenkov chambers. In this chapter, the description of the SiPM is given, together with its main features and figures of merit. A particular focus is dedicated to recent developments that see SPADs, the SiPM unit microcell, and SiPMs used in direct detection of charged particles. Indeed, these recent results constitute the starting point of the SiPM studies at the heart of this thesis.

2.1 Silicon detectors

A silicon detector is a semiconductor device which is basically a solid state ionization chamber. The highest energy band is the conduction band, where electrons are free to move. The below band is the valence band, where electrons are tightly bound. In solid state lattices, atomic levels merge to energy bands: the properties of a material come from the gap between the two bands. While for conductive materials there is no gap and for isolators it is > 5 eV, semiconductors materials feature an intermediate situation with a band gap of 1.12 eV at 300 K. For this reason, electrons can be excited by simple thermal energy to the conduction band.

Each silicon atom of the lattice shares four valence electrons with the neighbor atoms. At temperatures near 0 K all the electrons are bound, but at $T > 0$ K thermal vibrations break some of the bonds, making electrons available for conduction (electron conduction). The remaining open bonds are holes in the valence band of the crystal lattice: an electron within the valence band may fill the hole, leaving another hole in its place. In this way holes appear to move (hole conduction). The intrinsic concentration of electrons in the conduction band, n, and holes in the valence band, p, in an intrinsic semiconductor is the same at T=300 K [24]:

$$n_i = n = p = 1.45 \times 10^{10}\mathrm{cm}^{-3}. \tag{2.1}$$

Charged carriers are then transported through diffusion and drift. For fields up to 10^4 V/cm, drift is proportional to the applied electric field E. Indeed, the drift current densities for electrons, which drift against the electric field, and holes, which drift with the electric field, are respectively

$$J_{n,drift} = (-q)nv_D = (-q)n(-\mu_n E) = qn\mu_n E \tag{2.2}$$

$$J_{p,drift} = (+q)pv_D = qp\mu_p E \tag{2.3}$$

where $\mu_n \sim 1350$ cm^2 V^1 s^{-1} and $\mu_p \sim 450$ cm^2 V^1 s^{-1} are the electron and hole mobility at 300 K while v_D is the drift velocity.

The diffusion current is proportional to the gradient of the carrier density: electrons diffuse down the concentration gradient but carry negative charge i.e. the electron diffusion current points in the direction of the gradient. On the other hand, holes diffuse down the gradient but carry positive charge. The diffusion density currents are then

$$J_{n,diff} = qD_n \nabla n \tag{2.4}$$

$$J_{p,diff} = -qD_p \nabla p \tag{2.5}$$

where D_n and D_p are the diffusion coefficients which depend on temperature and mobility.

The total current density of charge carriers for electrons and holes is in the end the sum of the two above mentioned contributions:

$$J_n = J_{n,drift} + J_{n,diff} = q(n\mu_n E + D_n \nabla n) \tag{2.6}$$

$$J_p = J_{p,drift} + J_{p,diff} = q(p\mu_p E - D_p \nabla p) \tag{2.7}$$

For fields $> 10^4$ V/cm, $\mu \to 1/E$ and the drift velocity $v_D = \mu E$ saturates reaching a value of 10^7 cm/s. This determines in 300 μm of silicon 10-30 ns of collection time respectively for electrons and holes.

Silicon is a semiconductor with an indirect band structure: because phonons are needed in order to have momentum conservation when the electron goes from the valence to the conduction band, the energy needed to create an e-h pair is higher that the energy gap and amounts to $\sim$ 3.62 eV. Then, if we consider a mean ionization energy $I_0 = 3.62$ eV, a silicon thickness $d = 300$ μm and a MIP $dE/dx = 4$ MeV/cm, we obtain that the signal of the MIP in the detector is:

$$\frac{dE/dx \cdot d}{I_0} \simeq 10^4 \ \mathrm{e^-h^+} \text{ pairs}. \tag{2.8}$$

While, if we look at charge carriers thermally created in intrinsic silicon with same thickness and area $A = 1$ cm^2 at 300 K we have

$$n_i d A \simeq 10^8 \text{ e}^-\text{h}^+ \text{ pairs.} \tag{2.9}$$

These thermal pairs have then to be reduced: for this reason, intrinsic silicon crystals are not used but a depleted zone, free from charge carriers, is developed through the doping of silicon. Atoms of silicon, which belongs to the IV group of the periodic table, are replaced with atoms of the V group, such as Phosphorus, that determines a weakly bound valence electron (donor), and atoms of the III group, as Boron, which leaves an open bond in the lattice (acceptor). This results in a N-type and P-type silicon interfaces. When these two interfaces are placed in contact, a P-N junction, as the one shown in Figure 2.1, is formed.

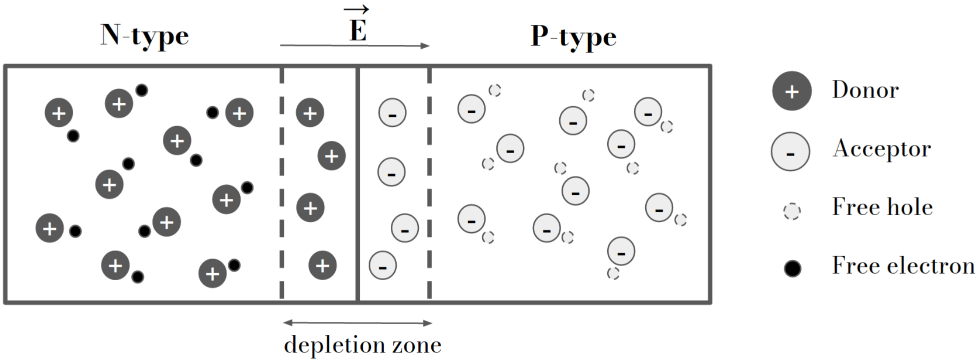

Figure 2.1: Scheme of a P-N junction.

Here, a diffusion of charge in excess to the other material is obtained until thermal equilibrium is reached: the positive ions of the N-type interface and the negative ions of the P-type interface create an electric field $\vec{E}$ which stops further diffusion. This process determines a space charge region free of charge carriers called depletion zone.

The application of an external voltage can increase or decrease the width of the depletion region: a forward bias voltage means a narrower depletion zone, while a reverse bias voltage pulls out electrons and holes increasing its width as illustrated in Figure 2.2. The latter results in a small reverse current flowing through the diode and a higher number of carriers produced by the passage of a particle. Semiconductor detectors are then operated in reverse bias mode.

P-N junctions are usually highly asymmetrical in doping concentration. A highly asymmetrical junction is called a one-sided junction, either an n^+p junction or a p^+n junction, where n^+ and p^+ denote the heavily doped sides. The depletion layer penetrates primarily into the lighter doping side, and the width of the depletion layer in the heavily doped material can often be neglected.

2.2 Particles through Silicon detectors

The operating principle of a p-on-n type silicon detector is illustrated in Figure 2.3: usually this detector features a P-N junction with heavily doped p^+ and n^+ electrodes. In the middle there is a lightly doped n^- type bulk. In reverse bias voltage condition, the

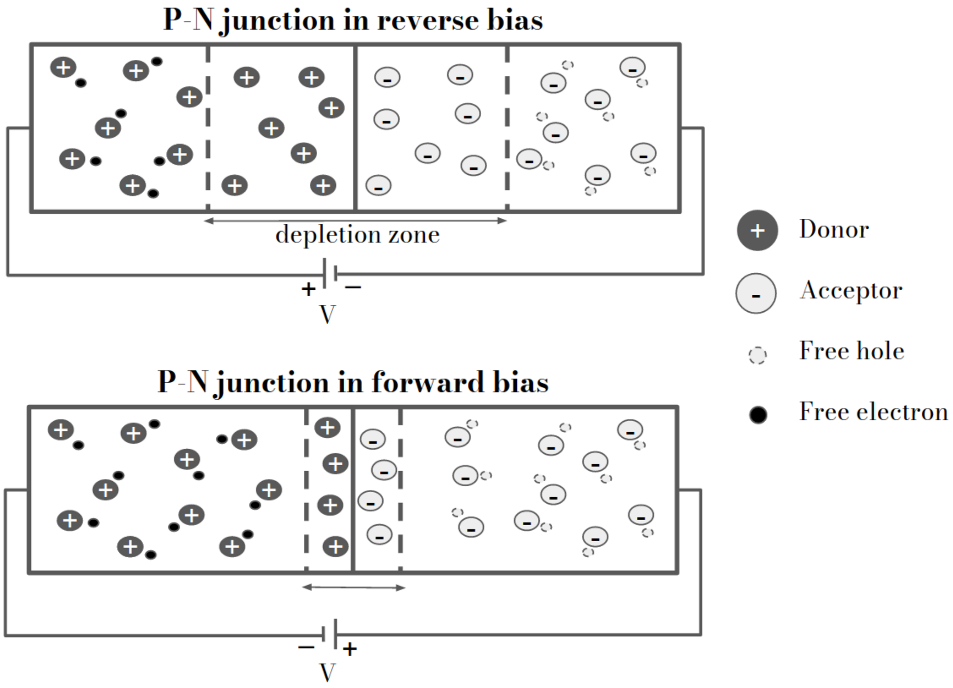

Figure 2.2: P-N junction in reverse and forward bias voltage scheme.

n^+ electrode is connected to the anode, while the p^+ electrode is coupled to the cathode. Once the depletion region has formed, charged particles or photons will interact with the sensor creating electron-hole pairs, which, being the only mobile charges, induce a current that will be measured. The signal starts when the carriers start to move and ends when all of them have reached their collection electrodes. Under an $E > 10^4$ V/cm, electrons travel 1 μm of silicon in 15 ps while holes do so in 30 ps. A tipical silicon detector of 300 μm is then travelled by electrons in $\sim$ 10 ns and by holes in $\sim$ 25 ns.

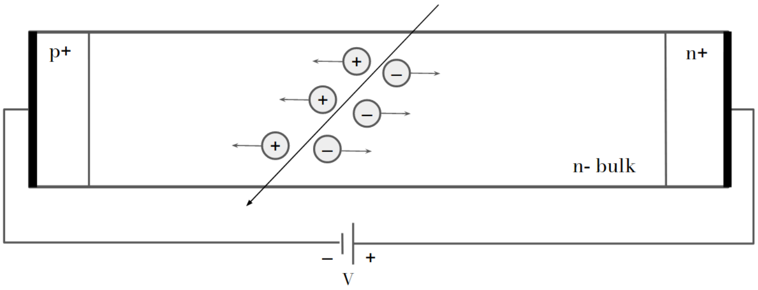

Figure 2.3: P-on-n type junction principle of operation.

In the next section, particle-silicon interaction mechanisms will be briefly illustrated with a particular focus on heavy charged particles (i.e. particles heavier than the electron, for example muons, pions, protons and light nuclei), electrons/positrons and photon interactions.

2.2.1 Charged particles

Ionization energy loss

When a heavy charged particle passes through the silicon detector, it mainly interacts through electromagnetic interactions with the atomic electrons, in particular with inelastic collisions [25]. Upon entering the detector medium, the particle immediately interacts simultaneously with many electrons via Coulomb force: depending on the proximity of the encounter, the impulse may be sufficient to raise the electron to a higher-lying shell within the absorber atom (excitation) or to remove it completely via ionization [26]. In most of the cases, ionization through electron stripping takes place. For 90% of all encounters the energy transferred to the electron in a single collision is less than 100 eV [27], so, since the energy required to form a pair for silicon at room temperature is ~ 3.6 eV, as the MIP transverses the detector it produces several e-h pairs. This process is called primary ionization: primary interaction products can interact again creating secondary ionization and, for high values of electric field usually associated to a reverse bias above the breakdown voltage V_{bd}, an avalanche multiplication process can occur.

The energy deposited within the medium can be calculated from

$$\Delta E = -\left\langle \frac{dE}{dX} \right\rangle d \tag{2.10}$$

where d is the absorber thickness and $\langle dE/dX \rangle$ is the linear stopping power averaged over the energy of the projectile particle. The linear stopping power in MeV/cm for moderately relativistic charged heavy particles with $0.1 \lesssim \beta\gamma \lesssim 1000$ is defined by the well known Bethe-Bloch formula

$$-\frac{dE}{dx} = K\rho \frac{Z}{A} \frac{z^2}{\beta^2} \left[\ln \frac{2m_e \gamma^2 v^2 W_{MAX}}{I^2} - 2\beta^2 - \delta - 2\frac{C}{Z} \right] \tag{2.11}$$

with $K = 0.1535$ MeV cm^2/g, ρ the material density in g/cm^3, Z and A atomic number and weight, z the charge of the incident particle in units of e, γ the particle Lorentz factor, W_{MAX} the maximum energy transfer in a single collision and $I = I_0 Z$ the mean excitation potential. For intrinsic silicon, Z= 14, A= 28.085 a.m.u. and $\rho = 2.329$ g/cm^3 [28]. The parameters δ and C accounts for density and shell effects, which are due respectively to a polarization of the medium and to the case in which $v_v \lesssim v_e$.

The possibility of large energy transfers in a single collision adds a long tail to the high energy side of the energy loss probability distribution of particles traversing thin detectors: this distribution can be modeled by the Landau-Vavilov straggling function. As shown in Figure 2.4 for 500 MeV pions in silicon, the position of the maximum of this distribution Δ_p defines the most probable energy loss. The latter is shown in Figure 2.5 for several silicon detector thicknesses scaled to the mean loss at minimum ionization ~ 1.664 MeV g$^-1$ cm^2.

For electrons and positrons the formula reported in Equation 2.11 is modified due to their small masses and indistinguishibility: because the projectile and the target have same mass, the energy loss in a single collision is much higher than in the case of a heavy

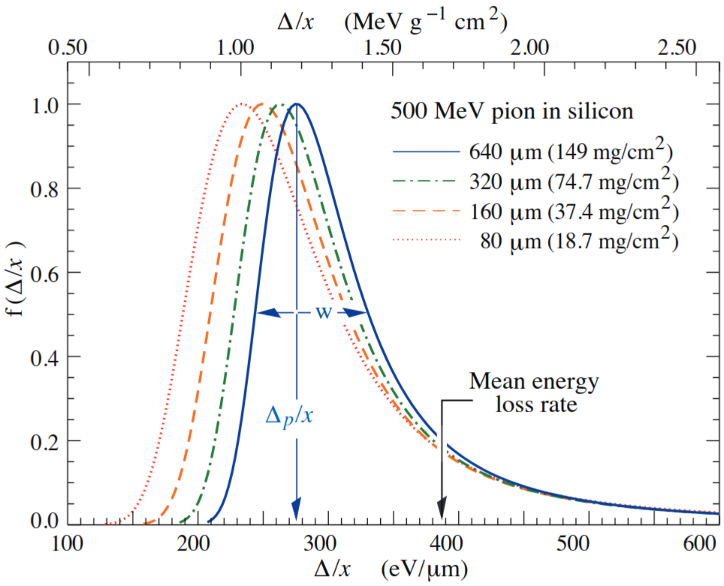

Figure 2.4: Straggling functions in silicon for 500 MeV pions, normalized to unity at the most probable value Δ_p/x. The width w is the full width at half maximum [28].

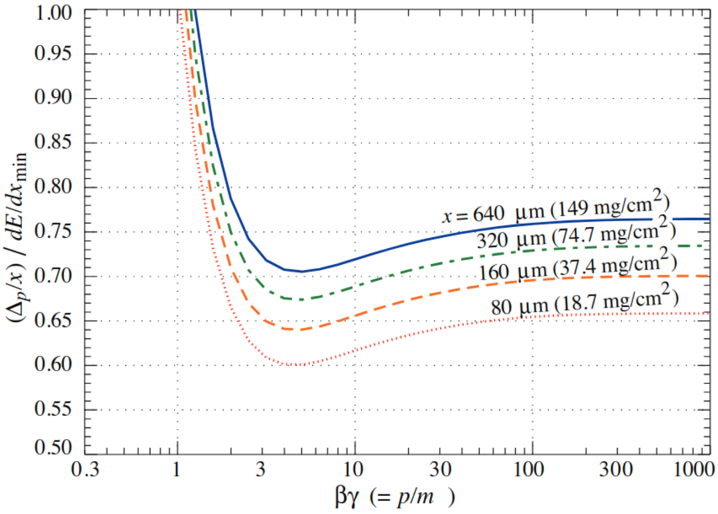

Figure 2.5: Most probable energy loss in silicon, scaled to the mean loss of a MIP 388 eV/μm [28].

charged particle. In addition to this, electrons and positrons lose energy via Bremmstrahlung by emitting photons when deflected through electromagnetic interaction with the nucleus. The total energy loss for electrons and positrons is then composed of a ionization and a radiative term:

$$\frac{dE}{dx} = \left(\frac{dE}{dx}\right)_{coll} + \left(\frac{dE}{dx}\right)_{bremss} \tag{2.12}$$

with

$$-\left(\frac{dE}{dx}\right)_{bremss} = \frac{E}{X_0} \tag{2.13}$$

where X_0 (in g/cm^2) is the radiation length of the material and E the energy of the incident particle. The radiation length is then defined as the mean distance over which the electron energy is reduced by a factor $1/e$ via radiative losses: for silicon $X_0 = 21.82$ g/cm^2 [28].

2.2.2 Photons

The main interaction mechanisms of photons in matter depend on the energy of the photon and are: photoelectric effect ($\gamma + atom \rightarrow e^- + atom^+$) at low energies, Compton scattering ($\gamma + e^- \rightarrow \gamma + e^-$) at about 1 MeV and pair production ($\gamma + nucleus \rightarrow e^+ + e^- + nucleus$) for high energy γ-rays. The relative contributions of the three different processes to the cross section in silicon is shown in Figure 2.6. The dominant process at energies below 100 keV is the photoelectric effect: through this reaction the photon completely disappears and, in its place, an electron (called photoelectron) is ejected by the silicon atom from one of its bound shells.

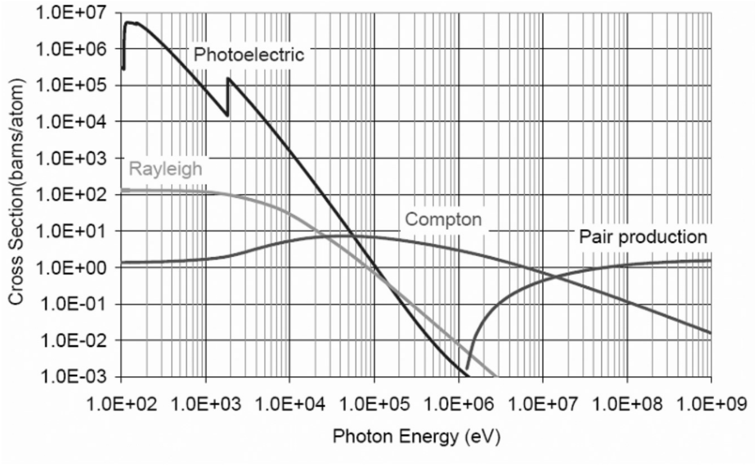

Figure 2.6: Photon total cross section as a function of the photon energy in silicon: atomic photoelectric effect, Compton scattering and pair production in the nuclear field are the main interaction mechanisms [29].

A photon beam of intensity I_0 traversing a material is then attenuated only in intensity through the above mentioned processes according to

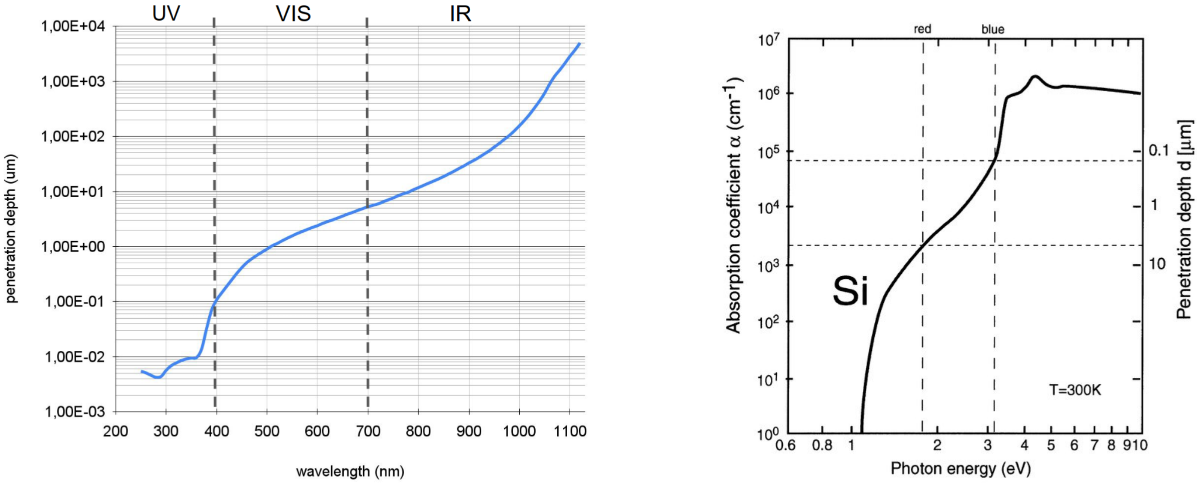

(a) (b)

Figure 2.7: (a) Penetration depth d of intrinsic silicon at 300 K as a function of the incident wavelength, data from [30]; (b) Absorption coefficient α and penetration depth d of light in silicon at 300 K [31].

$$I = I_0 \mathrm{e}^{-\alpha x} = I_0 \mathrm{e}^{-x/d} \tag{2.14}$$

where α is the absorption coefficient which is equal to the inverse of the mean free path of a photon i.e. the penetration depth d.

If the energy of the photon is below 1.12 eV, which corresponds to 1110 nm, the photon can be absorbed only from free electrons. For energies between 1.12 eV and 3.6 eV, which is the energy required to form an e-h pair, the reaction needs a phonon of high momentum to occur so the absorption probability is low. For energies above 3.6 eV, which corresponds to a wavelength of 344 nm, a direct transition is possible and the absorption becomes more probable. For this reason, larger λ can penetrate in the whole detector thickness without absorption, while smaller λ are immediately absorbed. These two contributions limit the sensitivity of the detector.

The average d for standard silicon at 300 K in the range $\sim$ 200-1110 nm as a function of incident light wavelength is shown in Figure 2.7a. Here, d is $\sim$ 0.1 μm at 400 nm at N-UV wavelenghts, $\sim$ 2.5 μm at 600 nm visible light wavelength and $\sim$ 10 μm at $\sim$ 780 μm IR wavelengths. A wavelength in the N-UV of 300-400 nm which corresponds to energies of 4-3 eV is absorbed in silicon in the first 0.1 μm as can be seen in Figure 2.7b where α and d are shown as a function of the photon energy in eV.

2.3 Silicon for timing

As introduced in Section 2.2, an electric field $> 10^4$ V/cm makes electron and holes velocities saturate: in this condition, electrons travel 300 μm of silicon in only 10 ns, while holes do so in 25 ns (collection time). This peculiarity, together with others that will be described in this section, makes silicon detectors ideal for timing applications.

2.3.1 Timing system components

The basic detector timing channel is shown in Figure 2.8 [32] [33]. The timing measurement is mainly related to the signal-to-noise ratio (SNR) and to the slew rate:

$$\frac{dV}{dt} = \frac{S}{t_r} \tag{2.15}$$

where t_r is the rise time of the signal and S the signal amplitude [34]. Large SNR and fast rising edge are then fundamental in order to increase the time resolution of a detector.

The main components that affect these variables are:

1. The detector, which can be schematized as a current generator in parallel with a capacitance. The current is produced when a particle deposits energy in the detector sensitive volume and starts to move.
2. A series of amplifiers, that, with appropriate coupling and impedance, amplify the detector signal.
3. A discriminator (or leading edge trigger), that compares the analog signal to a threshold voltage reference level giving a normalized logic pulse with a well defined time relationship to the input signal.
4. A time digitalizer (Time-To-Digital Converter or TDC), which measures the time difference between the detector signal and a reference start channel, for example a second detector.

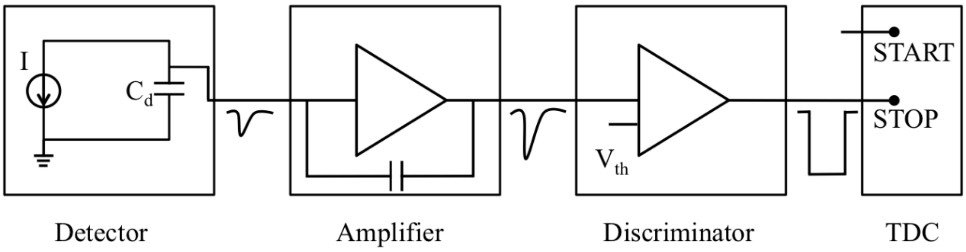

Figure 2.8: Scheme of the basic elements of the measurement chain [33].

The final time resolution of the system can then be expressed as:

$$\sigma_t^2 = \sigma_{jitter}^2 + \sigma_{TDC}^2 + \sigma_{current}^2 + \sigma_{TS}^2. \tag{2.16}$$

The jitter term σ_{jitter}^2 is due to the presence of noise: when the signal is rising, the threshold comparator can trigger early or late depending on how the noise affects the rising edge. This term is then directly proportional to the RMS of noise, σ_N, and inversely proportional to the slope, $\left|\frac{dV}{dt}\right|$, near the threshold value V_{th}:

$$\sigma_{jitter} = \frac{\sigma_N}{\left|\frac{dV}{dt}\right|_{V_{th}}}. \tag{2.17}$$

The TDC, a combination of a clock generator with a counter, determines a constant term which can be expressed as

$$\sigma_{TDC} = \frac{TDC_{bin}}{\sqrt{12}} \tag{2.18}$$

with TDC_{bin} the time width of the least significant bit of the TDC.

The Landau term $\sigma^2_{current}$ is due to an intrinsic statistical nature of the energy deposited by the MIP in the silicon, whose distribution in thin detectors is a Landau distribution: everytime the energy release changes i.e. every signal is different both in amplitude and in shape. In addition to this, the uniformity of the electric field may cause changes in the signal shape.

The time slewing term σ^2_{TS} is associated to the amplitude of the signal i.e. the deposited charge, which can exceed before or after the chosen threshold. Thus, this term is strictly related to the analog to digital conversion of the signals: this effect can be corrected by analyzing the maximum amplitude or the charge of the signal.

Being related to the particle-matter interactions and the structure of the detector, the last three terms can be considered together as an intrinsic resolution of the detector. Equation 2.16 can then be written as

$$\sigma^2_t = \sigma^2_{intrinsic} + \sigma^2_{jitter} + \sigma^2_{TDC}. \tag{2.19}$$

According to the Shockley-Ramo's theorem [35] [36], the initial current in a silicon detector does not depend on the thickness d of the sensor:

$$i_{max} \propto nqv_{sat}\frac{1}{d} = Ndqv_{sat}\frac{1}{d} = Nqv_{sat} \tag{2.20}$$

where $v_{sat} \sim 10^7$ cm/s and $N = n/d \simeq 75$ are the e-h pairs created per μm. The maximum current is of the order of$\sim 10^{-6}$ A. For this reason, increasing the thickness of the detector is not a solution for better timing: on the contrary, considering $v_{sat} \sim 10^7$ cm/s of charge carriers, deeper detectors correspond to longer collection times.

2.3.2 Gain

As already explained, for timing applications the electric field should be of the order of 10^4 V/cm in order to allow electrons and holes to saturate their velocities: 1 μm is associated to a collection time for electrons and holes of 15-30 ps respectively, thus a 300 μm is travelled in 10 ns by electrons and 25 ns by holes. The electric field must also be as uniform as possible: to do this, detectors must have a geometry as close as possible to flat capacitors, with the area of a single cell much larger than the sensor thickness.

Even if all the above conditions are met, silicon detectors have limited time resolution due to the presence of noise. For this reason, an internal avalanche process is often exploited in silicon timing application as a source of gain to increase the amplitude of the signal i.e. the jitter. The different operation modes for solid state detectors is shown in Figure 2.9. Usually avalanche Photo-Diodes (APDs) have a gain of 50-500 with mainly electrons able to sustain an avalanche. SPADs (Single Photon Avalanche Diodes) are Geiger-mode APD: they work at higher values of V_{bd}, the breakdown voltage, above which the avalanche starts, due to both electrons and holes, in a self-sustained process with gain $> 10^4$. SiPMs are made of arrays of SPADs and will be explained in detail in the next section.

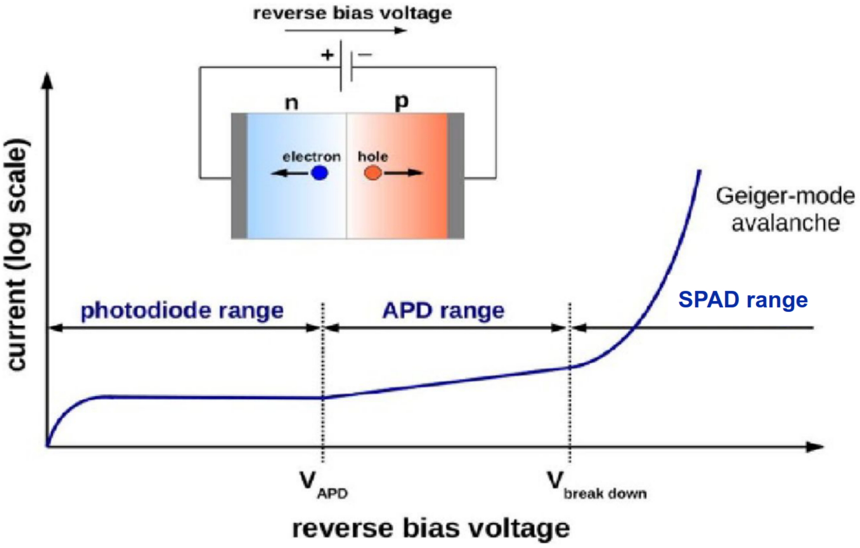

Figure 2.9: Different operation modes for solid state silicon detectors showing: Photodiode (linear, no gain), Avalanche PhotoDiode APD (linear, gain of 50-500) and Geiger mode APD i.e. SPAD (gain $> 10^4$) [2].

2.4 SiPM Silicon PhotoMultiplier

The Silicon Photomultiplier is an established device of choice for a variety of applications, from TOF-PET to lifetime fluorescence spectroscopy in biology and physics, from distance measurements in LiDAR applications to astrophysics and HEP [1] [2]. A solid-state detector can improve design flexibility, cost, miniaturization, integration density, reliability and signal processing capabilities in photodetectors with respect to older devices such as Photomultipliers (PMT) or Microchannel Plates (MCP) [37]. SPADs, fabricated by conventional planar technology on silicon and biased above breakdown (the so called Geiger mode regime) give excellent single-photon sensitivity thanks to the avalanche caused by impact ionization of the photogenerated carriers. The number of carriers generated as a result of the absorption of a single photon determines the optical gain of the device.

The SiPM, or MPPC, Multi-Pixel Photon Counter, is an array of a few mm^2 of $10^2 - 10^4$ SPADs [38]. In order to fully benefit from the good performance of the SiPM, in particular its sensitivity, the dynamic range and its intrinsically fast timing properties as a solid state semiconductor detector, it is necessary to understand the structure of a SPAD, i.e. the SiPM unit microcell, and its integration in an array, i.e. the SiPM, together with its main variables: photon detection efficiency, signal response, gain fluctuation, dark count rate, primary and correlated noise.

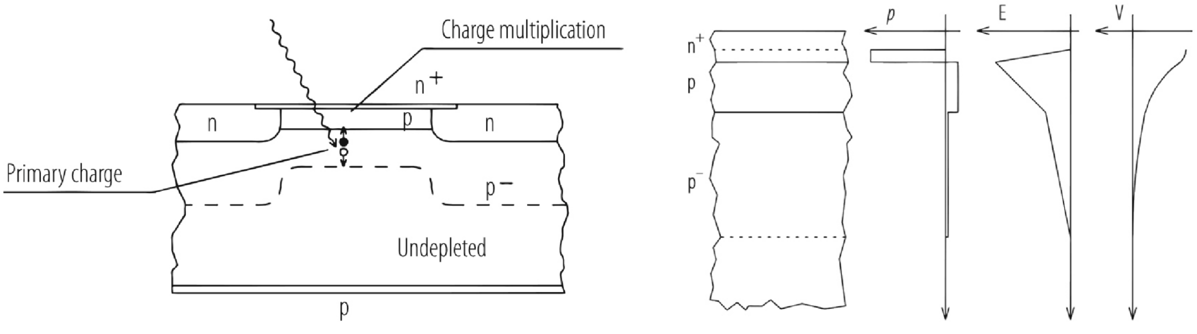

(a)

(b)

Figure 2.10: (a) N-on-p type AD; (b) amplification region with charge density, electric field and potential profile [39].

2.4.1 AP, APD and SPAD

The Avalanche Diode (AD) is a shallow p-n junction operated in reverse bias condition. The schematic of a n-on-p AD is shown in Figure 2.10a: the structure consists of a highly doped n-type layer (n^+) and a moderately doped p-type layer (p). The region with the highest electric field corresponds to the avalanche region: a detail of the amplification region is shown in 2.10b, where charge density ρ, electric field E and potential V are also reported. Under the p layer, there is a thick substrate lowly doped p^-. The p^- substrate is completely depleted in the upper part, determining the drift zone. The n^+ layer overlaps the p layer to form a virtual guard ring that is necessary to prevent premature edge breakdown allowing above breakdown operation of the active area. Recent technologies see the addition of other layers in order to have an electric field as uniform as possible and avoid pads border effects.

The avalanche process increases with the applied voltage. The AD can work in linear mode or in Geiger-mode when the applied voltage exceeds the breakdown voltage. The avalanche goes on until stopped by statistical fluctuations or a sufficient decrease of E. When the detector works in Geiger-mode, it is not possible to have a signal proportional to the charge released by the incident particle but single photons can be detected.

An APD (Avalanche PhotoDiode) is an AD for photons detection: in the APD mainly electrons generate secondary e-h pairs, resulting in a linear gain of $\sim$ 50-500. The SPAD (Single Photon Avalanche Diode) is a particular type of APD operated above its breakdown voltage i.e. in Geiger mode. In this way, single photon detection is possible. Differently from APD, in the SPAD holes also have enough kinetic energy to participate in secondary e-h pairs production: for this reason, the gain of a SPAD is $> 10^4$.

SPAD can be n-doped on p-doped SPAD (n-on-p type) for enhanced red/N-IR photosensitivity, or p-doped on n-doped SPAD (p-on-n type), for enhanced UV/blue photosensitivity, as shown respectively in Figure 2.11a and 2.11b. The different structure and width of the layers are made according to the absorption depht of silicon with respect to the photon wavelength at $T \sim 300$ K: UV photons, with $\lambda \sim 450$ nm, interact near the surface in the first μm of silicon, while IR photons with longer wavelenghts, ~ 750 nm, interact deeper in about 10 μm (see Section 2.2.2).

The difference in photosensitivity is then associated to the distance that the electron,

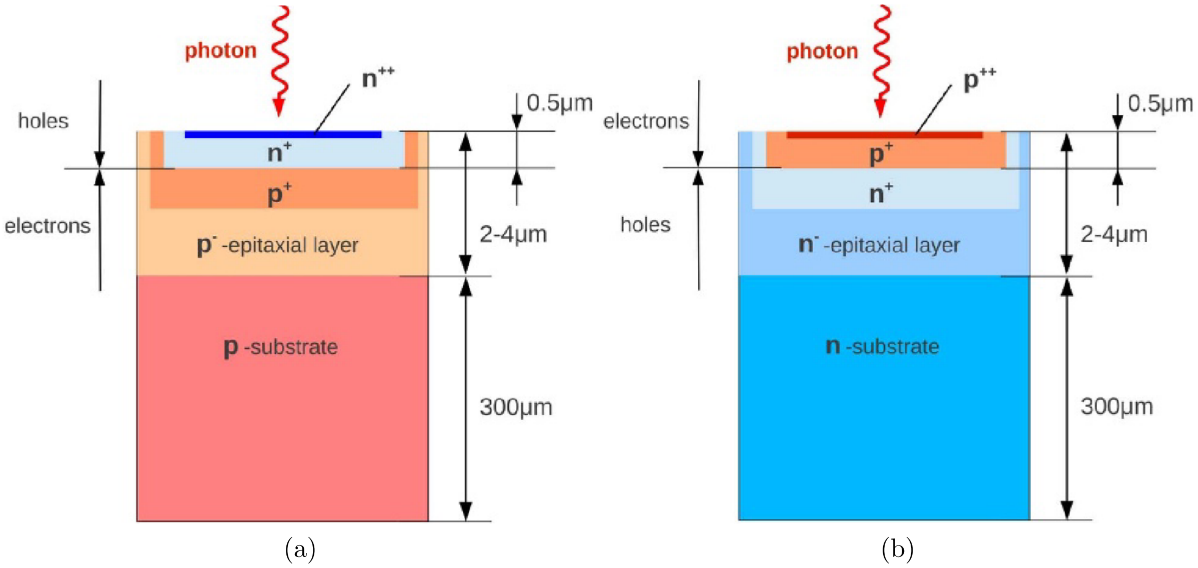

(a) (b)

Figure 2.11: The n-on-p SPAD (a) is more sensitive in the red spectrum region while the p-on-n SPAD (b) is more sensitive to the blue and near UV spectrum region [2].

which has greater ionization efficiency and avalanche probability than a hole, must travel within the depletion layer before being collected. This results in a different avalanche triggering probability P_T, whose profile along the junction can be observed in 2.12.

As previously said, photons in the blue to UV are absorbed closer to the surface of the SPAD: in the p-on-n structure this means that blue light will predominantly generate photoelectrons close to the surface, which will then traverse the junction towards the n-doped region [2]. Contrarily, red light will generate electron-holes deeper in the bulk: electrons traverse less material and are collected quickly, with a lower chance of triggering an avalanche. The PDE for a p-on-n SPAD is then lower in the red part of the spectra and higher in the blue. The contrary happens for a n-on-p SPAD, for which a schematic avalanche rapresentation is reported in Figure 2.13.

2.4.2 SiPM structure and working principles

The SiPM is an array of a few mm^2 of 10^2-10^4 SPADs that have a pitch of 10-100 μm. A photo of a SiPM can be seen in Figure 2.14.

The equivalent circuit of a SPAD is reported in Figure 2.15a. A SPAD can be modeled as a resistance R_d of about 1 kΩ and a capacitance (representing the depletion region) C_d of about 10 fF in parallel. In order to stop the avalanche, a series quenching resistor R_q of 10 kΩ-10 MΩ in parallel with a parasitic capacitance C_q of the order of fF is introduced for each SPAD. The passage of a particle closes the switch of the equivalent circuit: this causes an exponential voltage drop in the node between C_q and C_d, which starts to discharge according to the discharge time constant

$$\tau_d = R_d(C_q + C_d) \tag{2.21}$$

(neglecting the influence of R_q, which usually is highly resistive). At the same time C_q has been charging through R_d. The two processes end when the current through R_d

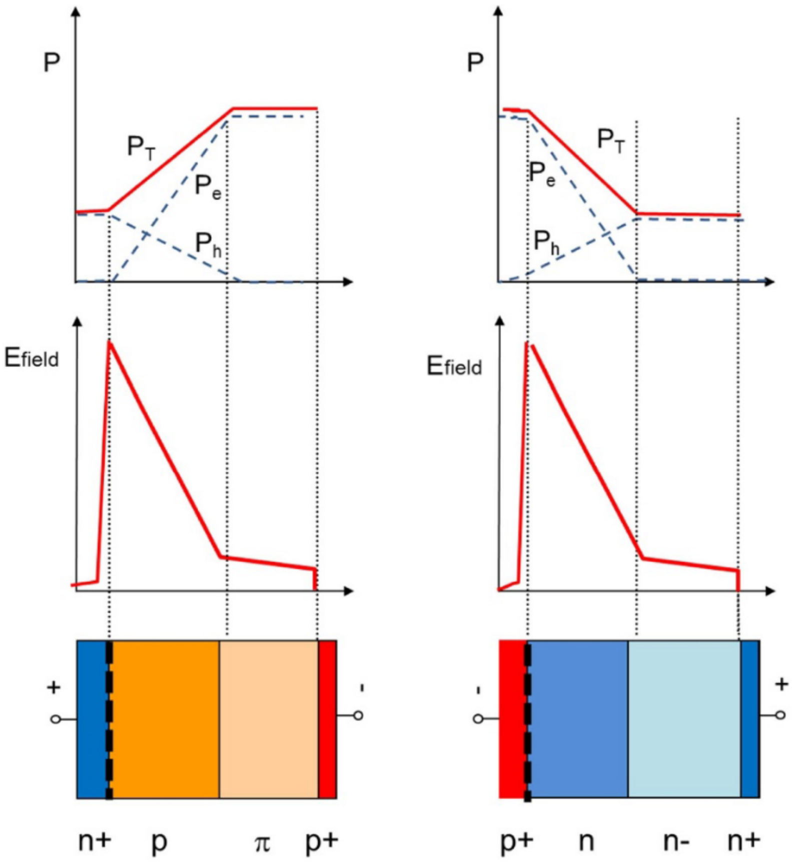

Figure 2.12: Electric field and avalanche triggering probability for the two types of SPADs. The maximum electric field is at the junction [2].

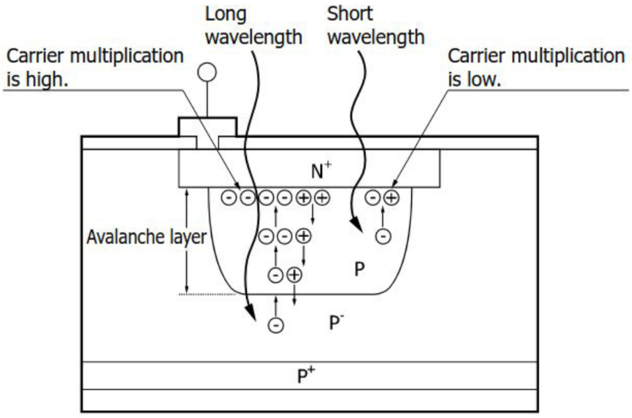

Figure 2.13: Visualization of absorption of short and long wavelengths of light in a red/near-IR enhanced n-on-p SPAD [40].

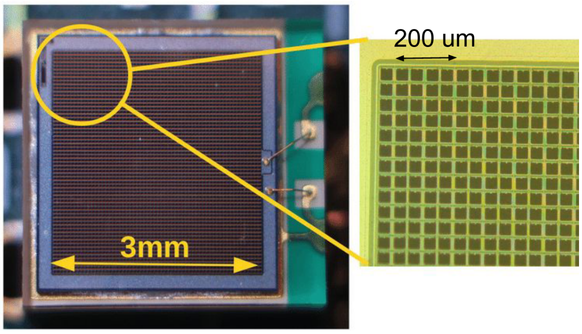

Figure 2.14: Photo of a SiPM with photographic enlargement of pixels (SPADs).

reaches the “threshold current” I_d

$$I_d \simeq \frac{V_{ov}}{R_q + R_d} \sim \frac{V_{ov}}{R_q} \tag{2.22}$$

where

$$V_{ov} = V_{bias} - V_{bd} \tag{2.23}$$

is the overvoltage (OV). At this point, the avalanche is “quenched” and the cell recoveries with a recharge time constant

$$\tau_r = R_q(C_q + C_d). \tag{2.24}$$

The total charge which has to be provided from the outside via the SPAD is given by $V_{ov}(C_q + C_d)$, which, divided by the electron charge q, gives the gain of the SPAD:

$$G = \frac{(V_{bias} - V_{BD})C_d}{q}. \tag{2.25}$$

The gain is of the order of 10^6 in analog SPADs and produces a single photon signal well above the electronic noise level.

In analog SiPMs, all pixels are independent and connected to a common readout in parallel as shown in Figure 2.15b resulting in a final signal that is proportional to the number of triggered SPADs. The output signal allows then to count fired SPADs by its amplitude.

A single pixel can be approximated by a parallel plate capacitor, whose capacitance is

$$C_{pix} = \epsilon_0 \epsilon_r \frac{A}{d} \tag{2.26}$$

with A the area of the plates and d their distance. Consequently, it is expected that its capacitance increases with decreasing distance of the two plates which corresponds to an increase of the depletion zone i.e. higher overvoltages. The total SiPM capacitance C can then be approximated, at high voltages so that parasitic and quenching capacitance of the pixels are negligible, according to

$$C = C_{pix} \cdot N_{pix} \tag{2.27}$$

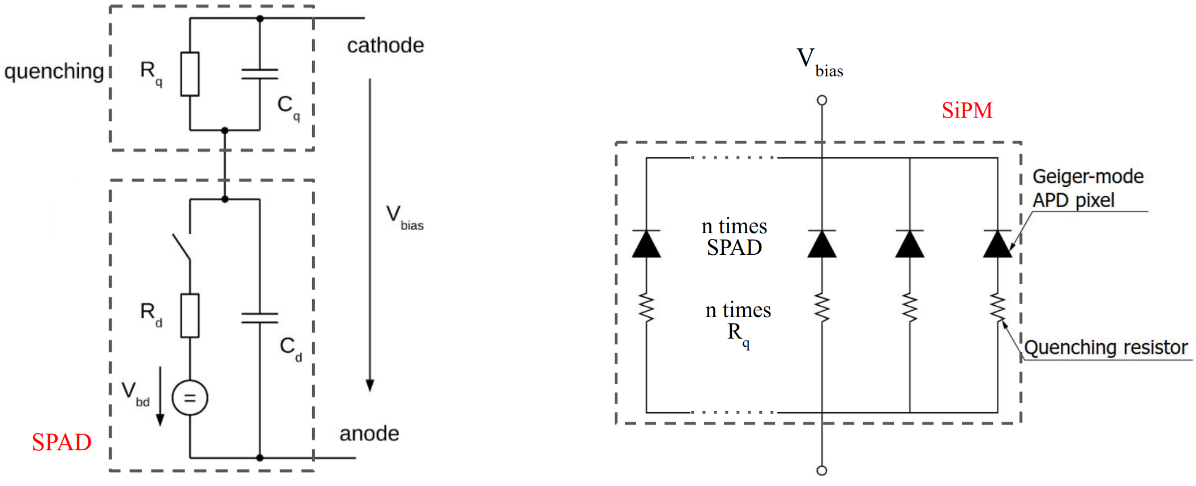

(a) (b)

Figure 2.15: (a) Equivalent circuit of a SPAD; (b) equivalent circuit of a SiPM.

where N_{pix} is the number of pixels.

With respect to Figure 2.9, the APD current increases proportional to the impinging light flux on the device: because the electric field is still below the breakdown voltage, electrons travel through the active layer of the detector creating an avalanche until a natural self-quenching occurs with no need of an external circuit. Increasing the reverse voltage V_{bias} above the breakdown voltage V_{bd} allows holes to perform impact ionization and participate to the avalanche in Geiger-mode operation. The signal is not proportional to the charge released by the impinging particle, but it allows to detect single photons as 10^4-10^6 charges for each SPAD are produced. The avalanche diverges and must be quenched by an external passive quenching circuit as previously mentioned.

To collect the charge signal from the detector a pre-amplifier with low noise of charge-sensitive type is generally used.

2.4.3 PDE

SiPM main feature is its particular sensitivity down to single photon detection, described by the PDE (Photon Detection Efficiency). This is defined as the ratio between the detected photons of wavelength λ and the actual photons impinging on the detector hence by the relation:

$$PDE(V_{ov}, \lambda) = QE(\lambda) \cdot P_T(V_{ov}, \lambda) \cdot FF(V_{ov}, \lambda) \tag{2.28}$$

where QE is the quantum efficiency i.e. the probability for an impinging photon to create a primary electron–hole pair in the active volume, P_T the avalanche triggering probability (already mentioned in Section 2.4.1), V_{ov} the overvoltage and FF the geometrical fill-factor [41]. The FF is defined as

$$FF = \frac{\text{Active area}}{\text{Cell area}} \tag{2.29}$$

where the active area is the area of the photo-sensitive cell. The FF is about 30-80% and depends on the SiPM technology and the SPAD design. The ideal P_T is 1 but it can

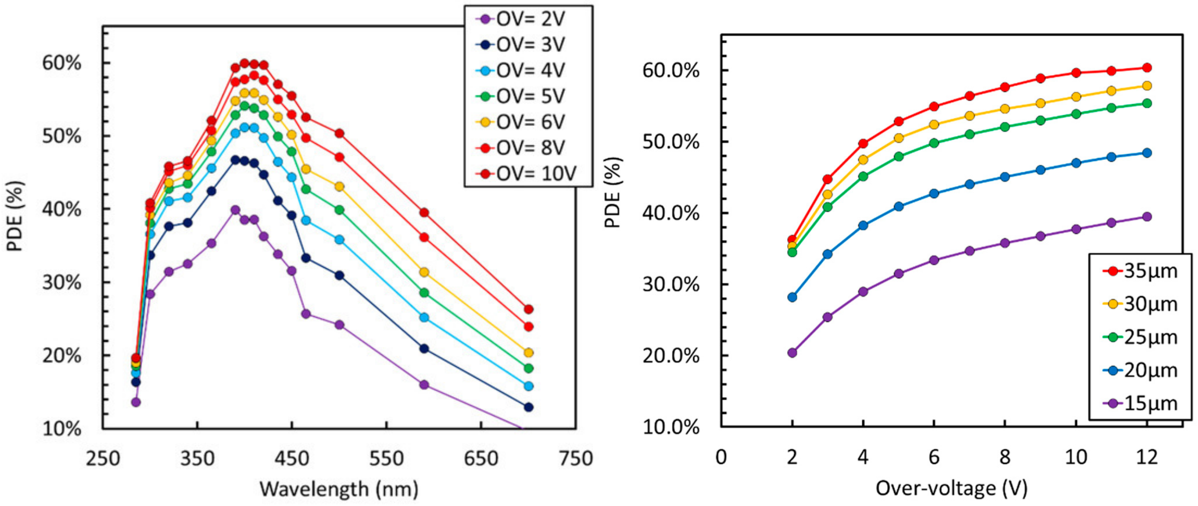

(a) (b)

Figure 2.16: (a) PDE as a function of wavelength at different values of V_{ov} (OV) for FBK prototypes; (b) PDE at 420 nm as a function of the OV measured on different cell pitches [42].

be lowered due to doping dishomogeneities for example related to radiation exposure.

The QE of silicon is dependent on the wavelength λ as illustrated in Section 2.2.2: for this reason, for UV applications protective coatings above the sensor are used in order to optimize the QE at small λ. For example, in Figure 2.16a the behaviour of FBK (Fondazione Bruno Kessler) SiPM NUV-HD (Near-UV sensitive High Density) prototypes with respect to wavelength of impinging photons is shown. The detector is covered with a protective silicon resin which is transparent down to 300 nm. The PDE at 6 V OV for these prototypes is about 40%-55% in the N-UV range 300-400 nm, making FBK NUV-HD SiPM technology well suited for Cherenkov light detection [42]. In Figure 2.16b the PDE as a function of OV for the same type of SiPM but with different cell pitches, i.e. different FF, is shown.

2.4.4 Noise

The primary source of noise in SiPM is identified by avalanche pulses triggered by thermally generated charged carriers or carriers generated due to tunneling in the high-field of the p-n in the bulk. These effects depend on the quality of the silicon, the volume of the depleted region, the fill factor of the cells and the temperature.

The rate of the avalanche pulse generation in dark conditions is called dark count rate (DC rate or DCR). A signal due to DC is indistinguishable from one that would have resulted from photon absorption. DCs are random and always present regardless of the light level illuminating the SiPM. DCR is proportional to temperature: DCR halves every ~ 8°C and, as can be seen in Figure 2.17, increases with OV. Being DCR a noise due to deep-levels into the silicon, it is crucially affected by radiation damage: in Figure 2.18 it is shown an increasing value of DCR that reaches a saturation with respect to proton irradiation [44].

In addition to primary noise, there is the so called correlated noise which identifies an

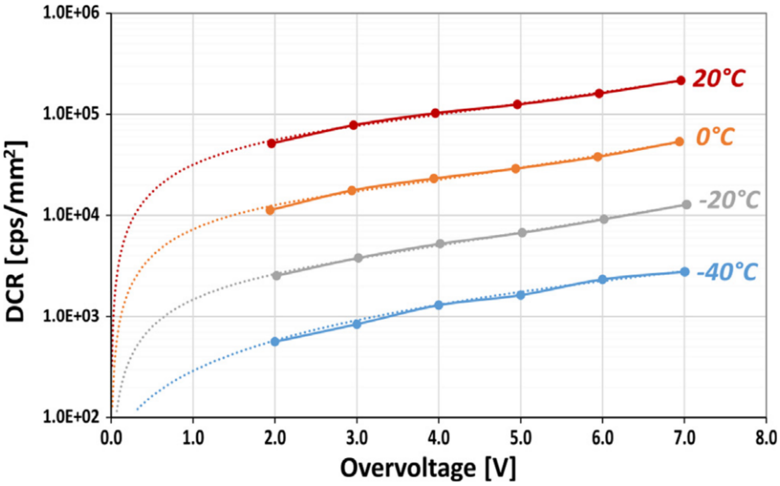

Figure 2.17: Example of measured DCR of a SiPM per unit area (1 mm ×1 mm) as a function of the overvoltage at different temperatures [41].

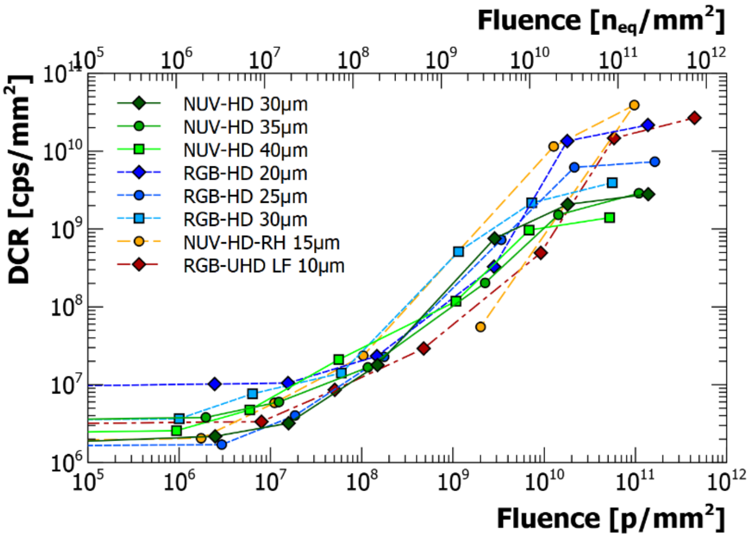

Figure 2.18: Primary DCR for different SiPM technologies and different pitch as a function of proton fluence at $V_{ov} \sim 5$V [44].

avalanche pulse generated because of the primary event, thus a subsequent noise. These are due to afterpulsing in the same cell or crosstalk in nearby cells of the SPADs array.

Afterpulse is due to trapping and subsequent release of carriers in the high field region, generating a secondary spurious avalanche. Afterpulse probability depends on the number of effective traps and on their release time constant with respect to the recovery time of the SPAD: a possible solution is to adjust the recovery time constant to have the traps released when the microcell is not yet completely recharged. Afterpulsing can also not be related to traps but to re-absorption of secondary photons of the avalanche in the neutral region beneath the active region, triggering again a secondary spurious avalanche: a solution here can be an inverted-doping substrate which originates a second p-n junction and blocks all photo-generated carriers to diffuse towards the avalanche region.

Secondary photons emission during the avalanche discharge is isotropic and can trigger new discharges in the adjacent cells: this is the so called "prompt" crosstalk (CT) which can be written as

$$\mathrm{CT} = \frac{\text{DCR with} \geq 2 \text{ SPADs firing}}{\text{DCR with} \geq 1 \text{ SPADs firing}}. \tag{2.30}$$

The CT is due to photons created in the avalanche that can trigger new avalanches and induce a fake signal in the adjacent cell. Indeed, in an avalanche breakdown ~ 3 photons $/10^5$ carriers are produced that can give rise to pulses two or three times the single-cell amplitude. Photons in the 850-1100 nm range are especially critical.

A "delayed" crosstalk is also possible, caused by e-h pairs in the bulk or in the neutral region near the depletion zone. This kind of crosstalk happens with a delay of ns-μs.

2.4.5 Signal shape

The signal produced by a SiPM is made of two components: a fast component, associated to Geiger discharge through the parasitic capacitance of the quench resistor, and a slow component, related to the SiPM recharging time. The rapid rise in the first stage of signal formation is associated to short drift and high drift speed. The slow component depends on the pixel capacitance and the quenching resistor as the overvoltage on the junction is gradually reestablished via the quench resistor after the avalanche.

An example of signal can be seen in Figure 2.19a. Considering also noise contributions as crosstalk and afterpulse, a SiPM signal under dark conditions can be observed in Figure 2.19b.

Considering the different kinds of observable noise events (primary events, prompt crosstalk, afterpulsing and delayed crosstalk), the SiPM output signal on a long time interval can be represented as reported in Figure 2.20.

Due to all these noises, the signal integral i.e. the charge of the particle is not associated to the number of firing SPADs given by the MIP alone. Thus, increasing the OV means increasing noise sources, as can be seen in Figure 2.17 of Section 2.4.4 for what concerns DCR.

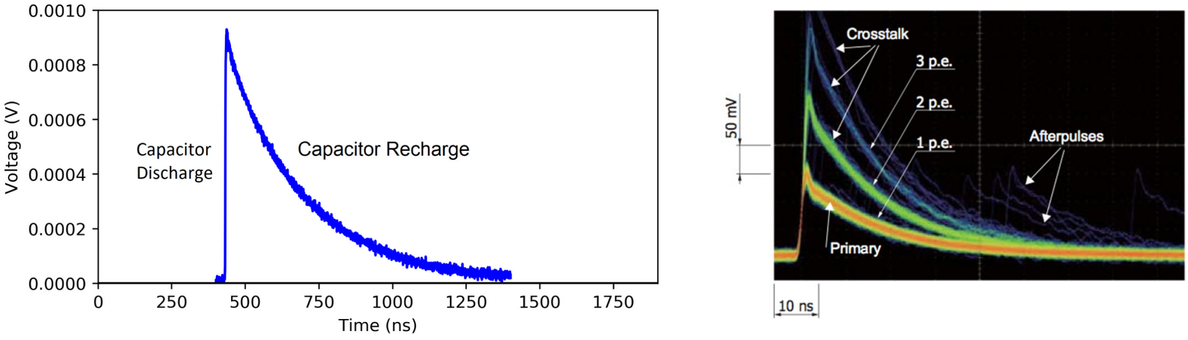

(a) (b)

Figure 2.19: (a) Illustration of a Geiger APD waveform [45]; (b) An oscilloscope trace (with the display set to persistence mode) of output waveforms due to noise from a SiPM under dark conditions: primary waveforms are due to dark count (1 p.e.), higher pulses (2 p.e., 3 p.e.) are due to CT [40].

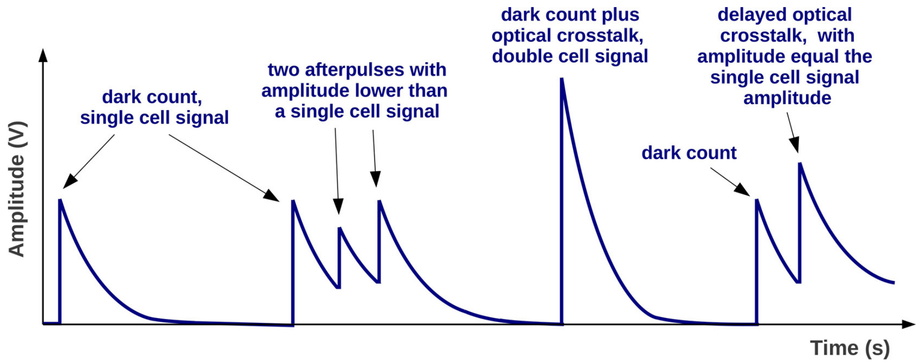

Figure 2.20: Analog SiPM output signal rapresentation of all the different noise contributions [41].

2.5 SiPM response to charged particles

In a series of recent studies, the detection of charged particles with SiPMs have been performed with promising results.

FBK NUV-SiPMs were tested in [46] with a beam of relativistic ions of $1 \leq Z \leq 28$ at energies 13-30 GeV/a.m.u. at CERN SPS. Here, SiPMs were directly exposed to the ion beam in order to study their capability to trigger an avalanche in response to particle ionization inside the device. The detector consisted of an array of discrete SiPM sensors with active area 1.4×1.4 mm^2 and pitch 50 μm. A photo of the array is shown in Figure 2.21. A charge tagging with high purity was provided thanks to a silicon beam-tracker that collected multiple dE/dx measurements. The SiPM were operated at 2 V OV to avoid the sensor saturation due to large ionization produced by high Z ions.

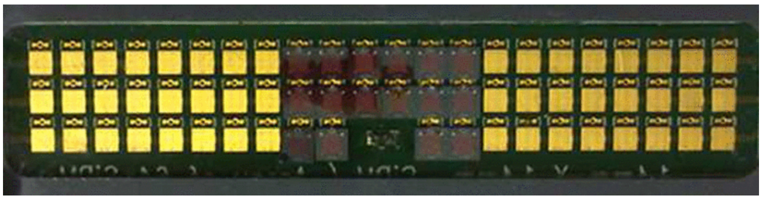

Figure 2.21: Photo of the SiPM array mounted in the middle of the 64 channels PCB used by [46] to directly detect charged particles.

The impact coordinate of He nuclei weighted by the pulse height of the SiPM having the largest signal in the event was reconstructed and it is shown in Figure 2.22: the pattern matches the geometry of the SiPM array providing a first qualitative evidence that the SiPM, although designed as a photodetector, can generate an avalanche upon the passage of a charged particle. An average efficiency with a threshold value of 0.5 p.e. of $\sim$ 59% and $\sim$ 81% was evaluated for ^{2}H and He respectively, indicating an effective detection area larger than the one expected on the basis of the optical fill-factor $\sim$ 42% of the NUV FBK SiPM prototypes under test.

While DCR prevents the use of single devices as position sensitive detectors, the coincidence between two or more SiPMs has been exploited in this direction by [47] with vertically-aligned avalanche cells put in coincidence. With this aim, Avalanche Pixel Sensor (APiX), basically a double-layered avalanche sensor, with embedded digital readout electronics on chip was implemented. The validity of an APiX structure detection principle was tested with a pair of SiPM sensors (of 1 mm^2 area each) exposed to a 120 GeV proton test beam at CERN. The SiPM have sensitive areas positioned face-to-face at a distance of the order of tens of μm. The active area of the two SiPMs is protected by an epoxy layer. A schematic view of the experimental apparatus is illustrated in Figure 2.23: the APiX prototype is placed between two scintillator counters that constitute the trigger.

The events with two coincident signals in the detectors are interpreted as MIP events. The ratio between the coincidence rate of the two SiPMs and the trigger rate of the monitor scintillators counters should be proportional to the ratio between the sensitive area of the SiPM and of the scintillator counters i.e. about 10^{-2}: indeed, the average value measured in four runs was $(1.47 \pm 0.25)\ \times 10^{-2}$. The challenges of an array of avalanche pixel sensors comprehend the $3D$ integration of such devices in CMOS technology as the

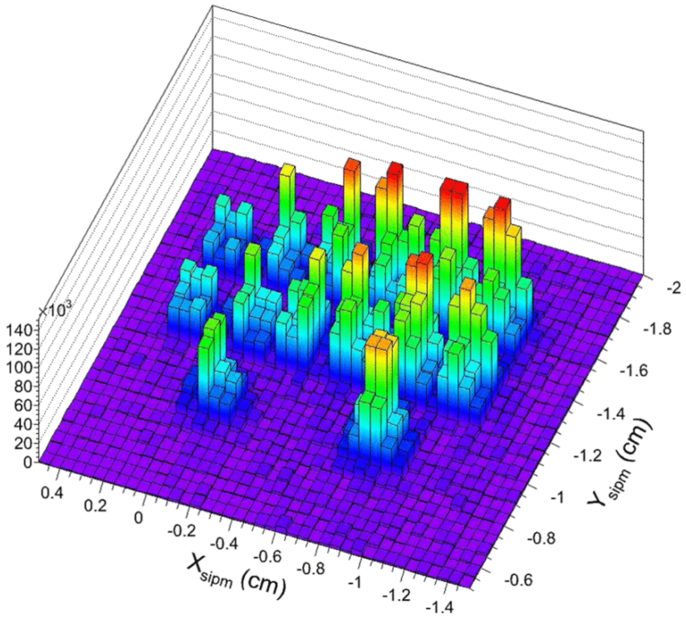

Figure 2.22: [46] reconstructed impact coordinates of tagged He nuclei weighted with the pulse height of the SiPM having the largest signal in the event.

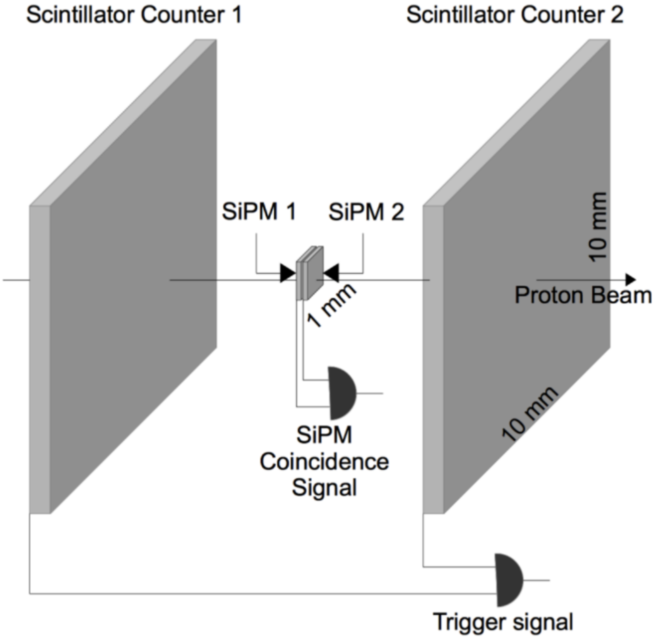

Figure 2.23: Schematic of the CERN test beam experimental setup used in [47] to test a prototype APiX structure made with two SiPMs in coincidence.

quenching network may impact the fill factor i.e. the PDE.

In [48], the time resolution of MIP via a TOF system was studied for single SPADs implemented in standard CMOS technology and integrated with on-chip quenching and recharge circuitry. The sensor used in this study integrates four independent SPAD pixels with 25 μm diameter, with a dedicated on chip front-end circuitry for every SPAD with tunable dead time ($\geq$ 3 ns). Through a complete and optimized system-on-board, all needed voltages are derived from a single 5 V power supply and a power management unit is designed to filter noise (essential for a target timing precision that approaches 10 ps). The TOF for 180 GeV/c momentum pions was measured at CERN SPS: an excellent intrinsic time resolution of 7-8 μs for a single SPAD was achieved. In the same study, radiation hardness of the SPAD was characterized with a mono-energetic beam of 100 MeV and a fluence of 10^8 protons per second. DCR increased of 3 orders of magnitude: nevertheless, SPADs were not saturated by DCR (thanks to their short dead time and high count rate) and were not affected with respect to their timing performance (the number of accidental coincidences due to DCR was suppressed by the logic AND between the SPADs used for the TOF). An improvement of the timing performance with respect to the applied OV was also noticed.

A more detailed understanding of the contribution of SPADs to SiPM total output signal, whose amplitude depends on the number of fired SPADs, was carried out in [3]: here, the direct response of SiPM being traversed by a MIP charged particle was studied for the first time in a systematic way. Using beam test data collected at CERN PS the time resolution and the CT have been measured. The study gave an unexpected result: although particles were expected to traverse only one SPAD per event, crosstalk measurements, defined as in Equation 2.30, on different SiPMs showed an higher value of fired SPADs with respect to the one related to the noise of the device. This is shown in Figure 2.24 where the response of different SiPM is evaluated at different OV. A time resolution of 40-70 ps, improving with the number of fired SPADs, was reached.

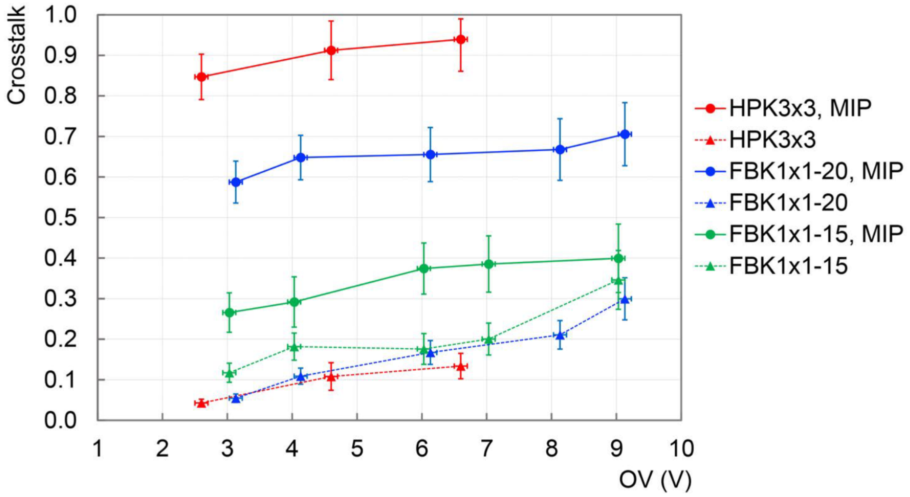

Figure 2.24: [3] measured crosstalk fraction CT versus overvoltage for beam test data (MIP, full lines) and standard evaluation via DCR (dotted lines).

The results of [3] pointed to an efficiency higher than the simple fill factor of the devices: the higher crosstalk and higher efficiency ($\sim 90\%$) indicated the presence of a mechanism inducing signal on nearby SPADs. The origin of this effect was not clear: it could have been related to internal processes in the bulk of the SPAD, to an external Cherenkov effect (see Appendix: Cherenkov radiation) or to a scintillation process. The work reported in this thesis aimed to distinguish in a quantitave way between the two options.

Chapter 3

SiPM studies

In this chapter, a description of the devices used in this thesis study is reported. A first study, carried out through the comparison of SiPMs with different, in thickness and material, resin protection layers, was performed in order to understand the direct detection of charged particles with the SiPM technology. This was done in a test beam environment during July 2022: this study confirmed the presence of Cherenkov light in the protection layers above the sensors. Next, a second study with modified prototypes with the aim of measuring in detail the identified effect and study the SiPM time resolution was carried out in another beam test setup during November 2022. All these studies have been performed in collaboration with FBK.

In both cases, preliminary measurements on the different SiPMs prototypes, performed at INFN Bologna laboratory, will be presented. Consequently, a study of the SiPM behaviour and results on the timing response with data collected at the two beam tests are discussed.

3.1 Detectors under study

Available NUV-HD-RH (Near UV-High Density-Radiation Hard) SiPM produced by Fondazione Bruno Kessler (FBK) were used in both the beam tests. NUV-HD SiPM technology was introduced in 2016 and, due to an optimized border region around each microcell, these devices have very high detection efficiency and high dynamic range [42] [43] .

NUV-HD SiPM pixels are p-on-n junction SPADs. A photo of the SiPM under test is shown in Figure 3.1 together with its main features in Table 3.1 . As explained in Section 2.4.3, the PDE is a function of the wavelength of the incident radiation. Actually, in Figure 2.16a the PDE of FBK NUV-HD SiPM prototypes was shown: at 3 V OV the PDE at 400 nm is close to 32%, while at 6 V OV it increases to 42%.

In order to study the different response of the SiPM with different protective layers, several resins have been used to cover the detector under test. In particular, two different resins have been identified, a silicon (SR) and an epoxy resin (ER), and different thicknesses of the resin itself have been used, 1 mm and 1.5 mm. The refraction index of silicon and epoxy is respectively 1.50 and 1.53. The nomenclature used in this thesis to address the different SiPMs is reported in Table 3.2 together with the main features of the protection layer. To disentangle any effect due to the resin, SiPMs without any

Figure 3.1: Microscope photograph of the FBK NUV-HD SiPM under study with hexagonal 20 μm pitch pixel.

Parameter	
Active area	1×1 mm^2
Pixel pitch	20 μm
Number of SPADs	2444
Fill factor	72%
V$_{bd}$	33.0 ± 0.1 V

Table 3.1: Main characteristics of the SiPMs under test.

Name	Resin	Thickness (mm)	Refraction index
SR15	Silicon	1.5	1.50
SR1	Silicon	1	1.50
ER1	Epoxy	1	1.53

Table 3.2: Protection layers main features of the SiPM under test during the July beam test. The protection layer characteristics determine the SiPM name.

resin protection (WR) have also been studied.

All the studied prototypes have the sensor reaching about 550 μm from the PCB on which it is mounted and the thickness of the protection layers is expressed starting from the PCB itself: the effective protection layer on top of the SiPM is then 450 μm and 950 μm for the 1 mm and 1.5 mm sample respectively. An explanatory drawing is shown in Figure 3.2.

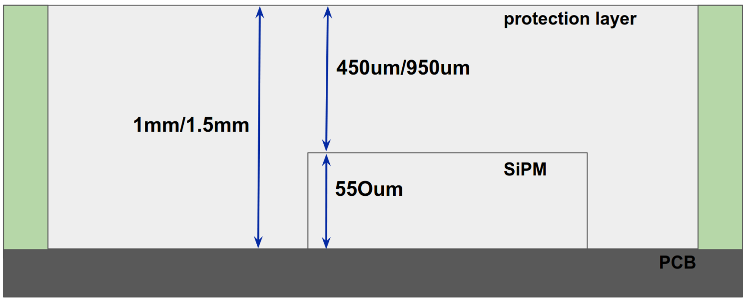

Figure 3.2: Explanatory drawing of the SiPM with protection layer under study.

3.1.1 SiPM studied in July 2022 beam test

A microscope photo of the SiPMs used during the first beam test carried out in July 2022 is shown in Figure 3.3: each sensor is part of a structure of six different, in cell pitch and geometry of the pixel, nearby SiPMs. The protection layer uniformly covers all of them. The SiPM under test corresponds to the one positioned on the top left corner of the matrix.

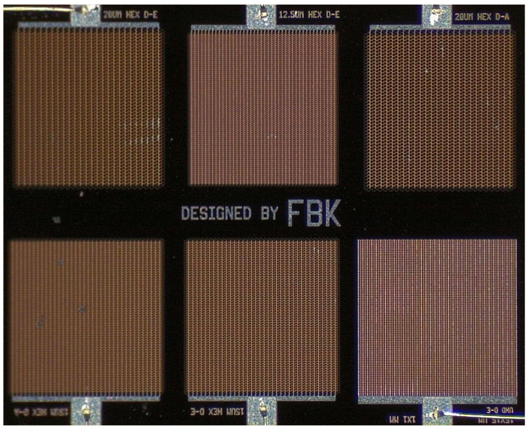

Figure 3.3: Microscope photograph of the configuration of the SiPM under study during the first beam test: a matrix of six different SiPM of area 1×1 mm^2. The protection layer uniformly covers all the six SiPMs.

3.1.2 SiPM studied in November 2022 beam test

The SiPM technology under study in the November beam test was the same as in the previous study i.e. NUV-HD-RH SiPMs introduced in Section 3.1. On the other hand, the six-SiPM structure was dropped in favour of a single-SiPM structure. This was done in order to have a more precise deposit of the resin on top of the SiPM, consequently allowing to better characterize the effect related to it. The protection layer, applied over the 1×1 mm^2 sensor, has an area of 1.7×3.5 mm^2. The longer resin side covers the wire bonding of the sensor, while the shorter side overflows the sensor of 200 μm on one side and 500 μm on the other. A photo with the reference axis and values is shown in Figure 3.4.

The sensors were produced again with three different protection layers: silicon resin of 1 mm, silicon resin of 1.5 mm and epoxy resin of 1 mm. The nomenclature used in this study is analogous to the one used for the July beam test with the addition of the suffix "-s" to account for the single configuration of the SiPM, as reported in Table 3.3. The devices under test were two for every type of sensor.

3.2 Preliminary measurements

In order to characterize the different SiPMs, IV curves, CV curves, DCR and CT measurements were performed in the Bologna laboratories. In this way, the intrinsic V_{bd} of all the samples was found together with other characteristics of the device.

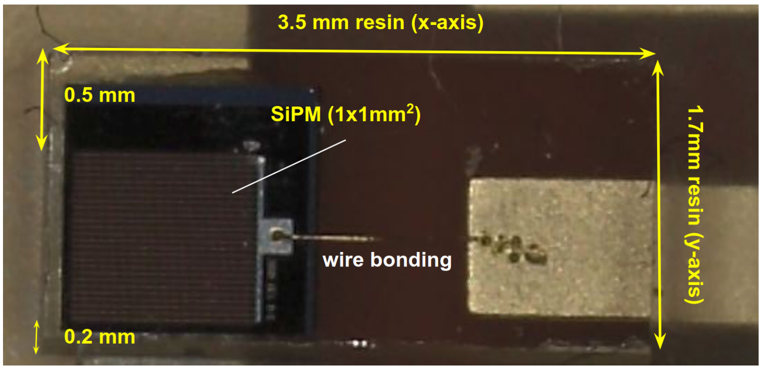

Figure 3.4: Microscope photograph of the single 1×1 mm^2 SiPM with rectangular resin on top.

Name	Resin	Dimensions (mm^2)	Thickness (mm)	Refraction index
SR15-s	Silicon	3.5×1.7	1.5	1.50
SR1-s	Silicon	3.5×1.7	1	1.50
ER1-s	Epoxy	3.5×1.7	1	1.53

Table 3.3: Protection layers main features of the single SiPMs under test during the November beam test. The protection layer characteristics determine the single SiPM name.

3.2.1 IV curve

The most important characterization measurement of silicon detectors can be extracted from a IV (current-voltage) curve of the device, which is a diode working in reversed biased condition. This measurement allows to determine the optimal working voltage of the device. For SiPM, in particular, it is important to determine the breakdown voltage, V_{bd}, at which the sensor enters in Geiger mode and starts a self-sustained avalanche process. The IVs of the SiPM used are obtained with a TDK Lambda Z100-2 power supply [49] and a Keithley 6487 picoammeter [50]. The scan was performed with a LabVIEW program. The measured IVs of the SiPM studied in the July beam test are reported in Figure 3.5a, while the IVs of single SiPMs, studied in the November beam test, are shown in Figure 3.5b with the number associate to the sample indicated between the parentheses.

The breakdown voltage can be obtained from the IV curve applying the Inverse Logarithmic Derivative (ILD) method which consists in calculating the inverse derivative of the IV curve [51]. Below the breakdown voltage, ILD shows a linear voltage dependence with a negative slope, and above breakdown, ILD starts with a linear rise, changing to a quadratic dependence at higher voltages. To extract the minimum of the ILD i.e. V_{bd}, a parabolic fit is done on 8 points around the minimal values of the IVs. The mean V_{bd} of the prototypes is measured to be of (33.3 ± 0.2) V, in agreement with the nominal value of (33.0 ± 0.1) V given by FBK and reported in Table 3.1. From now on, the term OV will be then considered with respect to this value of breakdown voltage.

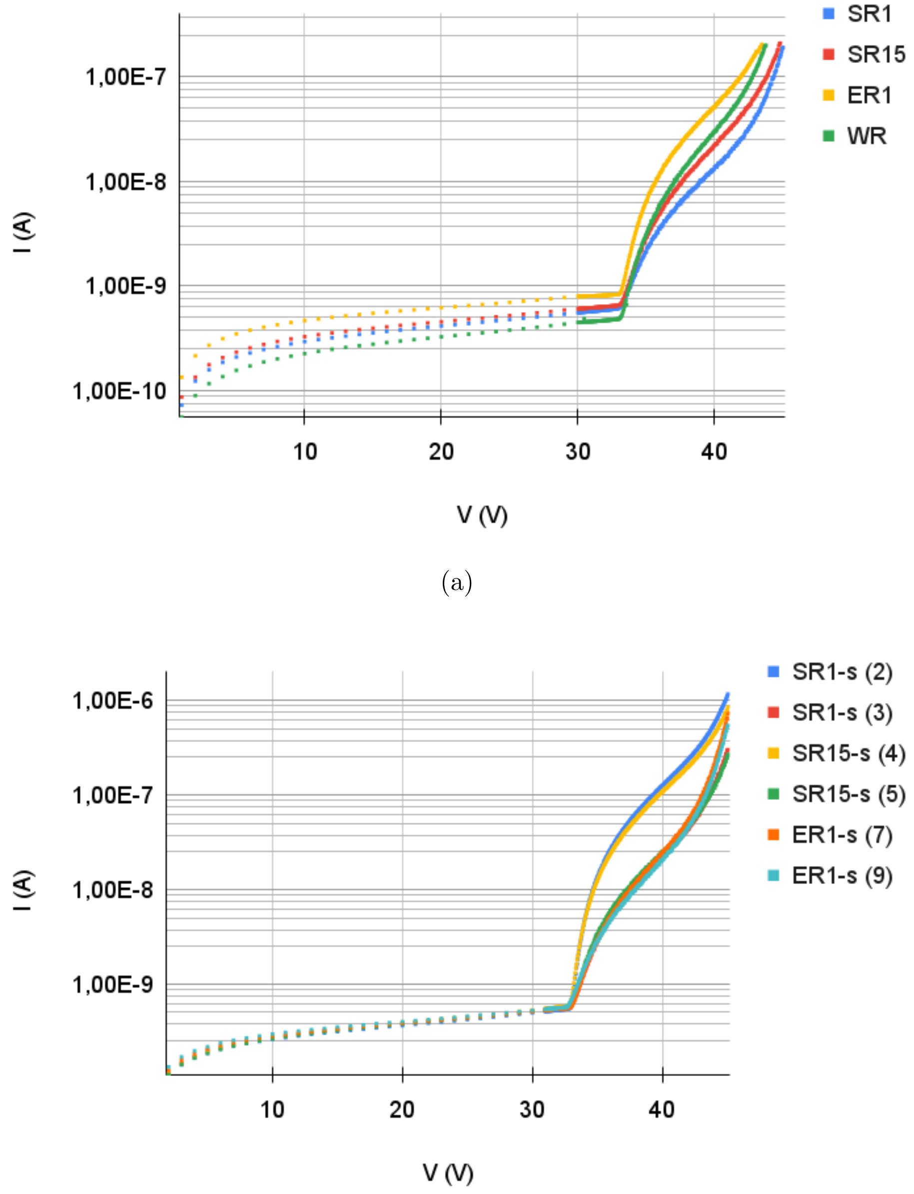

(a)

(b)

Figure 3.5: (a) IV curve of the SiPMs, part of a six sensors structure, under test during the July beam test; (b) IV curve of single SiPMs under test during the November beam test. In both cases, data near the breakdown voltage were obtained with a smaller step in V.

V$_{ov}$	2 V	3 V	4 V	6 V
SR15-s	(40 ± 6) kHz	(73 ± 13) kHz	(101 ± 19) kHz	(130 ± 25) kHz
SR1-s	(51 ± 9) kHz	(92 ± 12) kHz	(128 ± 16) kHz	(165 ± 20) kHz
ER1-s	(41 ± 2) kHz	(71 ± 6) kHz	(101 ± 9) kHz	(133 ± 16) kHz

Table 3.4: DCR for SiPMs with different protection layers evaluated with a digital oscilloscope in the Bologna laboratory at room temperature.

3.2.2 CV curve

The CV characteristic is another important preliminary measurement to perform on a silicon device. Some parameters that could be obtained are the pixel capacitance, the effective doping concentration, the electric field or the depletion voltage.

The measurement of the CV curves was performed with a Keysight impedance analyzer [52] with a frequency of 200 kHz. The measurements are obtained with a TDK Lambda Z100-2 power supply and Keithley 6487 picoammeter. The scan was performed with a LabVIEW program. The CV curves for the SiPMs under test during the July beam test and the November beam test are reported respectively in Figure 3.6a and 3.6b.

The SiPM fully depletes at ~ 40 V, which corresponds to an asymptotic value of the SiPM capacitance of 50 pF. The pixel capacitance for all the tested samples can then be evaluated via Equation 2.27 considering the nominal value of $N_{pix} = 2444$ and $C = 50$ pF: C_{pix} is ~ 21 fF, in agreement with [42].

3.2.3 Dark Count Rate

In order to better characterize the single SiPM prototypes, before the November beam test measurements of DCR at 2, 4, 6 and 8 V OV in the Bologna laboratories were performed. These were obtained putting the sensors in a dark box at room temperature. The data were taken with a Lecroy Wave-Runner 94904M-MS digital oscilloscope (500 MHz-4 GHz bandwidth, up to 40 GS/s sample rate, 4 input channels) [54] with a TDK Lambda Z100 used as power supply. SiPMs were all coupled to the same front-end which is a customized front-end made in the Bologna Laboratories with an X-LEE amplificator of 40 dB.

Trigger was set on one channel at 40 mV to avoid baseline background fluctuations (of about 10 mV). The counts of DC events considered for signals ≥ 1 SPAD were evaluated using a fixed threshold of about 50% of the signal of the first SPAD at 2 V OV. This was done with a dedicated function on the oscilloscope. Oscilloscope bandwidth was set to 200 MHz in order to avoid high-frequency noise and data acquisition was set to 10 GS/s. The amplitude scale was set to 50 mV/div and the timebase to 500 μs/div. A table with mean values of DC for every type of sample with relative protection layer is reported in Table 3.4. The values are obtained as the mean value of three independent samples available for the same SiPM: DCR is about 40-165 kHz/mm^2 between 2-6 V OV. At ~ 6 OV the mean DCR for all the samples is $\sim (110 \pm 13)$ kHz, in agreement with the [42] nominal value of ~ 100 kHz/mm^2 at same OV at room temperature.

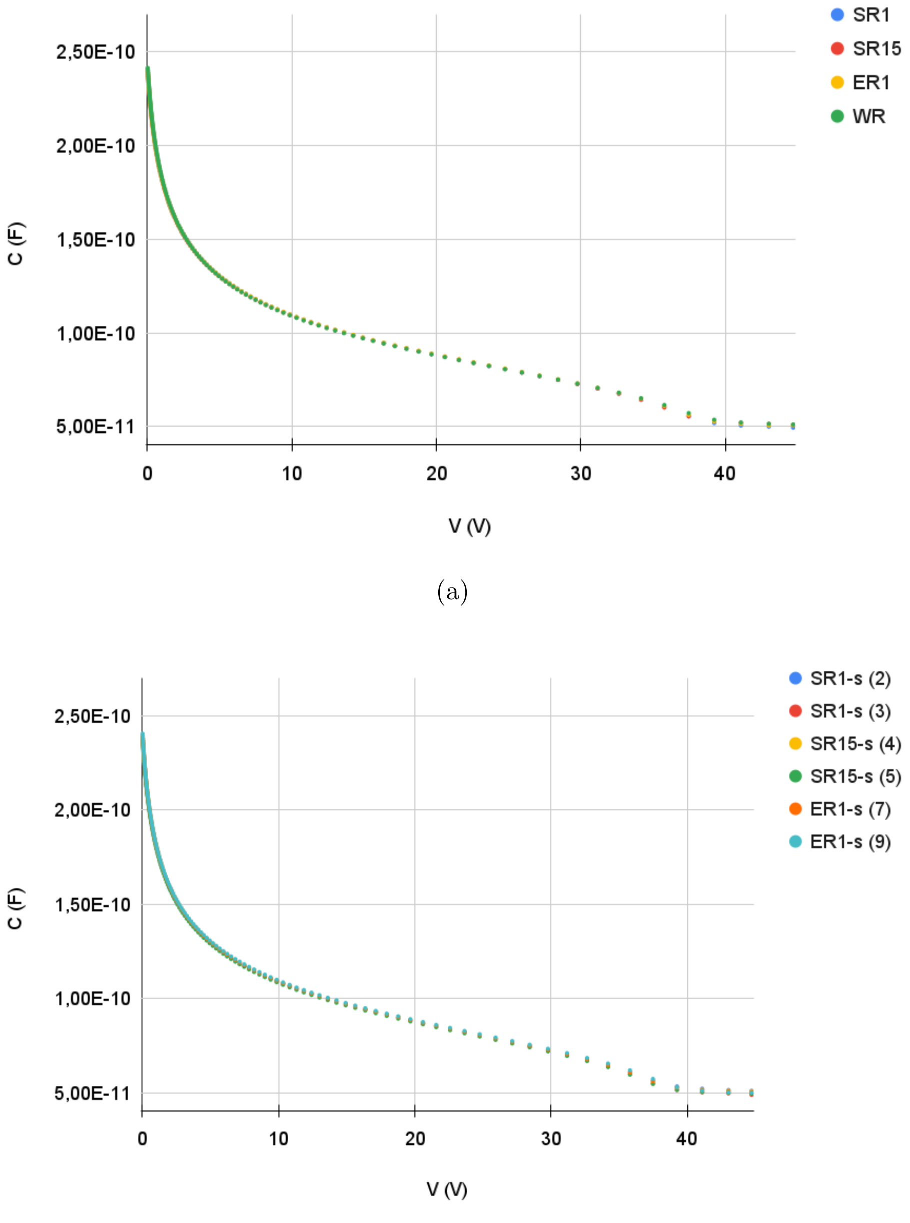

(a)

(b)

Figure 3.6: (a) CV curve of the SiPMs, part of a six sensors structure, under test during the July beam test; (b) CV curve of single SiPMs under test during the November beam test.

3.3 Beam test studies

3.3.1 Experimental setup

The study of the SiPMs response to charged particles has been carried out at the T10 beamline of CERN-PS in July and November 2022 through two different beam tests. At 12 GeV/c, the positive beam is composed mainly by protons ($\sim$ 80%) and pions ($\sim$ 20%).

The telescope used during the July beam test, which can be seen in Figure 3.7, consists of four sensors: two SiPMs under test and two LGADs detectors (1×1 mm^2 area and 35 μm or 25 μm width prototypes) [53]. The LGADs are used as trigger and as time reference t_0. As a consequence they define the active area of the beam.

The whole setup was enclosed in a dark box, as shown in Figure 3.7. It is worth noticing that, during the July beam test, the temperature ranged between 30 °C and 38 °C, higher values compared to the temperature employed for the preliminary studies of the devices.

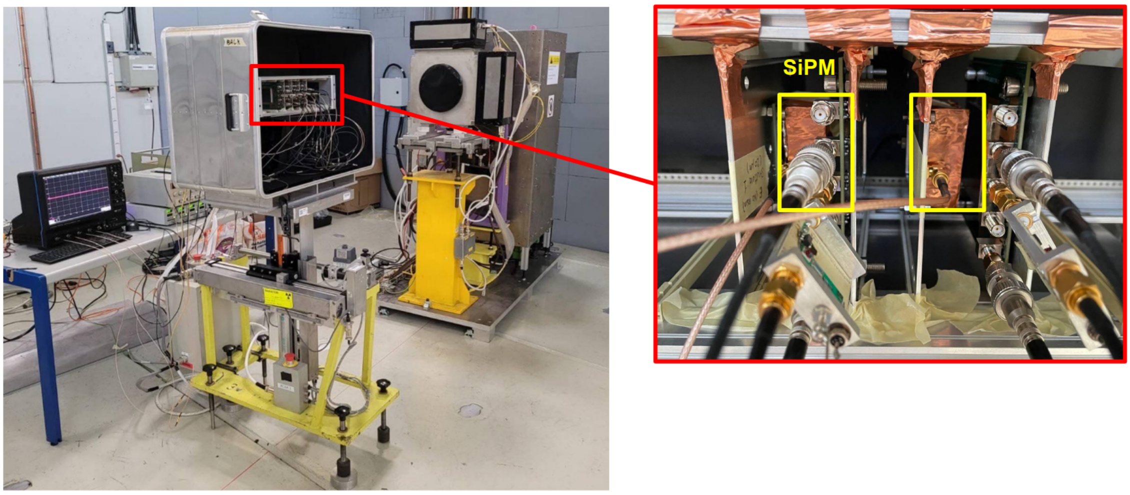

Figure 3.7: Photo of the experimental setup at the T10 CERN-PS during the July beam test with a photo in detail of the telescope. The two SiPMs under test are enclosed in a copper box.

The SiPM were independently amplified by a gain factor of 40 dB i.e. a voltage gain of 100 between 1 MHz-1 GHz signal frequencies. TDK Lambda Z100 power supplies were used for SiPMs and CAEN N1470 4CH HV for LGADs [55]. The waveforms were stored using a Lecroy Wave-Runner 94904M-MS digital oscilloscope [54] at maximum bandwidth of 4 GHz. The trigger was defined by the coincidence of the two LGADs signals in the telescope. The oscilloscope acquires the whole signal waveforms, thus the digitalization is performed at analysis level.

All instruments were remotely controlled in the control room through LabVIEW applications which allowed for data transfer and storage, setting and monitoring of V$_{bias}$ and currents, box temperature monitoring and fast online analysis to have a quick real time check on the data.

During the second beam test in November 2022, the setup was the same but with the addition of four independent micropositioners inside the box in order to remotely control SiPMs and LGADs sensors (x, y) positions with a precision of $\sim 10\ \mu$m. In addition to allow for a better alignment of the sensors i.e. maximize the number of triggered events, the positioners were needed to perform a scan in position of the single SiPMs and study the mean signal amplitude as a function of the position of the sensor with respect to the beam. A photo of the setup is shown in Figure 3.8. The positioners were controlled by an Arduino board connected to the control room with a LabView programme.

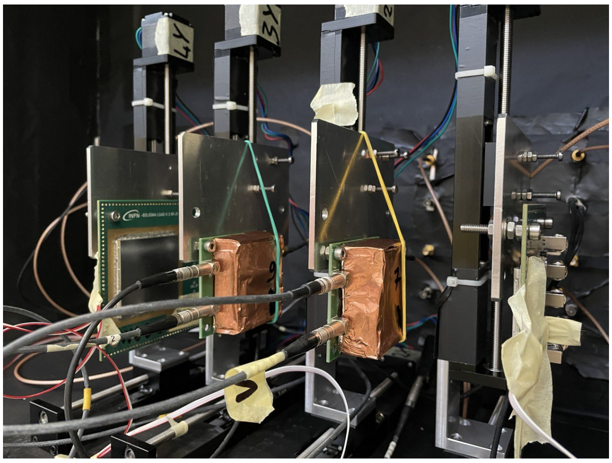

Figure 3.8: Photo of the four independent micropositioners added during the second beam test of November 2022 with two single SiPMs placed in the middle of the two LGADs. SiPMs are embedded in a copper box.

During the tests, the temperature ranged between 25 °C and 28 °C (to be noticed the lower temperature with respect to the July beam test).

3.3.2 Signal selection

Signal and DC events selection proceeded through different steps. Given the LGADs trigger condition time t_0, the signal events collected by the oscilloscope are those with a SiPM signal in a window of ± 2 ns from t_0. The DC events are defined as events with at least 1 SPAD firing in a region before the trigger (from the start of the oscilloscope time scale to -5 ns from t_0): this is used to determine the possible contamination of noise events in the signal region. DC events are estimated to be $< 5\%$ for single SPAD events and negligible for multiple SPADs events for all the SiPMs under test.

Events in a time window of 10 ns right before the signal region were used in the July beam test to evaluate the intrinsic CT from DC events, which was one the main measurements of the beam test (see Section 3.4.1).

In order to study the time resolution, a cut was applied on the SiPM signals by removing the few events with important residuals of previous signals, could they be MIP or DC events, in a time window of 8 ns before the signal zone (-10 ns to -2 ns from the trigger).

An example of all the triggered signals collected with the oscilloscope can be seen in Figure 3.9a, while in Figure 3.9b the same waveforms with selection cuts are reported.

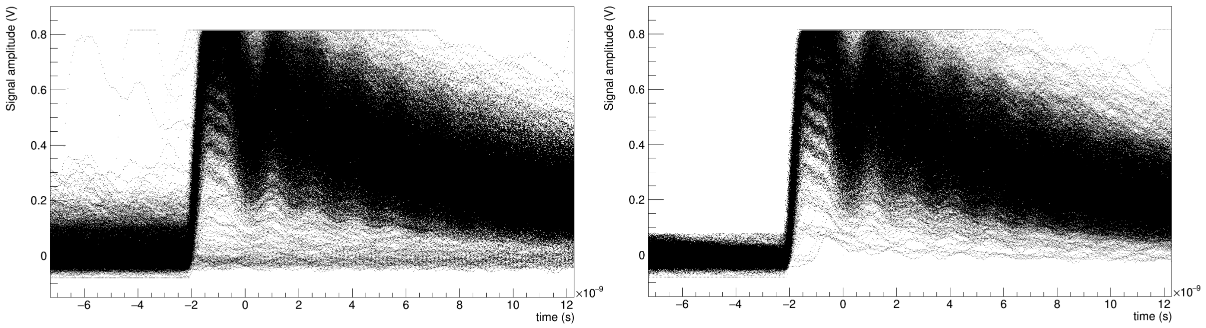

(a) (b)

Figure 3.9: (a) All triggered events on a SiPM (the sample is SR15-s at 4 V of OV); (b) offline selection of the SiPM waveforms.

The selected events are then used in the analysis of the time resolution.

3.3.3 Evaluation of the time resolution

In order to study the time resolution of the SiPM, the time associated to the LGAD signals is considered at 50% CFD while for the SiPM a fixed threshold of the amplitude of the first SPAD is used. The time resolution of a SiPM is evaluated by using the time difference between the SiPM under test and the LGAD which is nearer to the beam entrance. An example of the time difference distribution is shown in Figure 3.10.

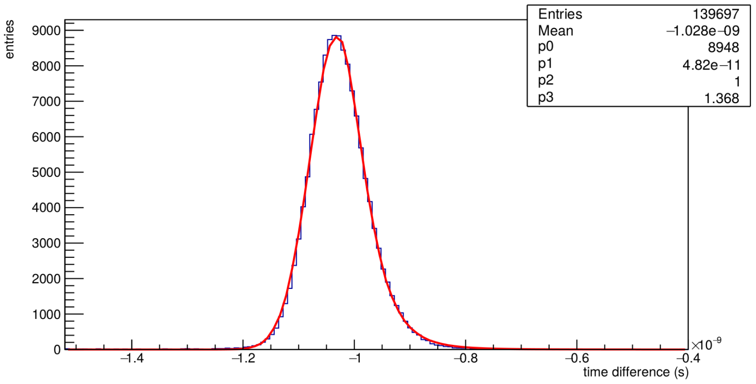

Figure 3.10: Example of histogram for the time difference between the SiPM under test (here SR15-s) and the trigger considering only events with $\geq$ 4 SPADs firing. $p1$ represents σ_{fit}.

The fit of the distribution is done with a q-Gaussian to account for its long tails. The σ of this distribution is given by the sum in quadrature of the SiPM and the LGAD contributions

$$\sigma_{fit} = \sqrt{\sigma_{SiPM}^2 - \sigma_{LGAD}^2} \tag{3.1}$$

with σ_{LGAD} the intrinsic LGAD resolution ($\simeq$ 27.1 ps at 250 V during the July beam test [53], $\simeq$ 31.2 ps at 110 V during the November beam test).

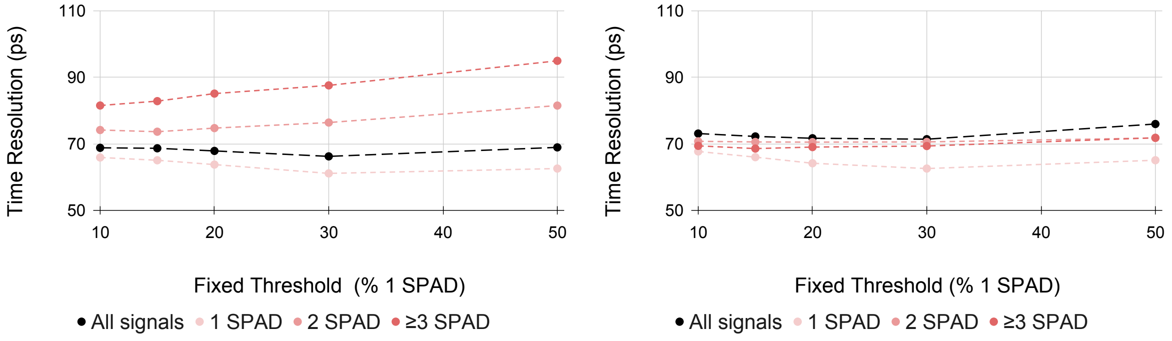

(a) (b)

Figure 3.11: Time resolution as a function of the fixed threshold at different percentage of the first SPAD amplitude for a sample of WR SiPM at an OV of (a) 4 V and (b) 6 V. The resolution values have an estimated associated error of about 6% at 1 SPAD, 8% at $\geq$ 2 SPADs.

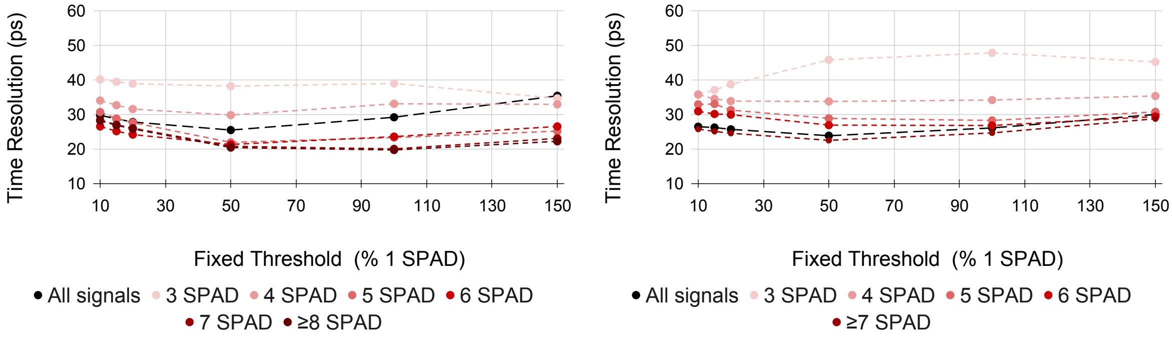

(a) (b)

Figure 3.12: Time resolution as a function of the fixed threshold at different percentage of the first SPAD amplitude for a sample of SR15-s SiPM at an OV of (a) 4 V and (b) 6 V. The resolution values have an estimated error of about 8% at 3 SPADs firing, 6% at $\geq$ 4 SPADs firing.

Thanks to a fast scan with 200k events, the optimal fixed threshold percentage on the signal of the single SPAD was evaluated for the evaluation of the time resolution. The scan is performed for a sensor which gives multi-SPAD signals, SR15-s, and a sensor which exhibits only a few SPADs firing, WR. The time resolution as a function of the threshold is then studied both for all waveforms and for a selected number of fired SPADs.

After selection, considering all signal waveforms the events become about 100k. Of these, for WR $\sim$ 85% of the selected waveforms are associated to 1 SPAD signals, while for SR15-s $\sim$ 90% of the selected signals are associated to $\geq$ 7 fired SPADs. The results are shown in Figures 3.12 and 3.11 at an OV respectively of 4 V and 6 V.

For SR15-s, it is clear that, as the number of fired SPADs increases, the time resolution decreases, going from 50-40 ps to 30-20 ps. The same trend, together with the fact that increasing the OV the time resolution for all signals slightly decreases, will be observed in Section 3.5.4. It is worth noticing that for 1 and 2 SPADs the analysis could not be carried out as the number of events was too low (< 300). The number of entries at 3 SPADs is of the order of 1000 while the majority of events happens for ≥ 6 SPADs. Indeed, at values of fired SPADs ≥ 6 the time resolution seems to be independent from the threshold.

On the other hand, the WR sensor, whose time resolution as a function of the threshold is reported in Figure 3.11, features a majority of 1 SPAD events: the time resolution is then 60-70 ps for 1 SPAD events while it increases at higher number of fired SPADs, both at 4 and 6 V OV. This may be associated to DC events that affect the time resolution at higher number of SPADs firing as they are due to intrinsic CT (more details will be given in the following Section 3.4). The difference in time resolution changing the threshold seems to be more limited at lower thresholds both for 4 and 6 V OV. In addition to this, the time resolution considering all signals is a few ps higher at 6 V OV: this trend will be confirmed when studying the time resolution in Section 3.5.4.

Because at 20% of the single SPAD signal the time resolution is optimal and the dispersion in the time resolution for different number of fired SPADs for both WR and SR15-s is reasonably limited at every value of OV, this percentage is chosen for the analysis of the timing resolution of all the SiPMs.

3.4 Results: understanding direct detection of charged particles with SiPMs

The following results are obtained with the data collected during the July 2022 beam test.

The aim of this study was understanding the origin of the excess expressed in CT on the SiPM observed in [3]. Indeed, when traversed by a MIP, the SiPM showed a higher CT with respect to the expected intrinsic CT measured via dark count events.

Considering that the probability of random pixels firing together is negligible, a possible explanation based on Cherenkov effect is investigated. Cherenkov light emission may be associated to the presence of the protection resin layer above the sensors. This would imply that the excess of CT should be present when particles impinge the detector from the front, defined as the photon sensitive side, and should be highly reduced or disappear when particles enter the detector from the back. An explanatory drawing of the front and back configurations is shown respectively in Figure 3.13a and 3.13b.

On the contrary, if the excess is related to processes inside the bulk of the sensor structure, no difference should be observed. Clearly, a simple scintillation effect in the protection resin would not cause any difference in a front or back configuration. After having addressed this effect, the time resolution of the different SiPM as a function of the number of SPADs was studied. The results of the July test beam were also published in [56].

Recall that during the July beam test the experimental setup was not yet provided with micropositioners: therefore the alignment of SiPMs was not as precise as the November beam test and the position of the SiPM could not be controlled with precision.

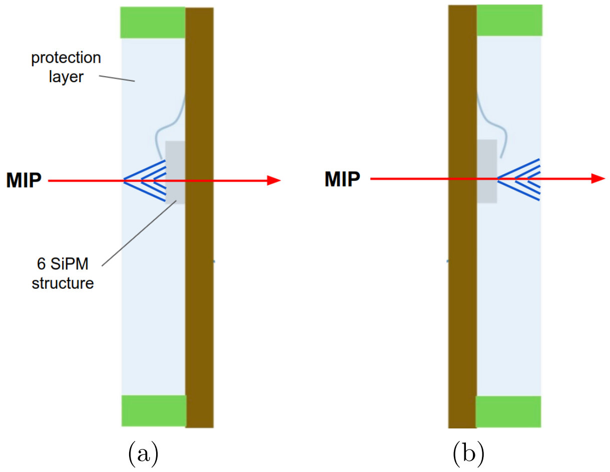

Figure 3.13: (a) Front configuration: MIP impinging the sensor from the photon sensitive side with collection of Cherenkov light; (b) back configuration: MIP impinging the detector from PCB side.

3.4.1 Crosstalk

Analogously as in [3], the CT fraction was defined as the ratio between the n firing SPADs and the total number of firing SPADs:

$$F_n = \frac{\text{events with} = n \text{ SPADs firing}}{\text{events with} \geq 1 \text{ SPADs firing}}. \tag{3.2}$$

This measurements of F_n was repeated for all the samples at different OV with particles impinging from the front and from the back of the detectors. Because of the finite scale of the oscilloscope, n can assume values up to 3 SPADs i.e. all saturated signals are associated to a $n \geq 4$.

F_n is computed in the following way: every peak from the amplitude distribution is fitted to a Gaussian distribution. Then, the cut between two SPADs i.e. two adjacent peaks are set to 3σ from the mean of the peak with higher number of events between the two (as this should be nearer to its Gaussian mean expectation value), while the error associated to F_n was evaluated considering the events in the range $\pm 1\sigma$ of the same peak around each cut. The results of F_n are reported in Table 3.5 and the same are shown in Figure 3.14. Here, the square markers indicate the intrinsic CT evaluated in a time window of 10 ns before the signal i.e. they represent intrinsic CT, the triangle markers are for data with the beam impinging the detector from the front while the circular markers are for data with the beam impinging the detector from the back.

The WR sensor shows no difference between the particle impinging from the front or the back and its intrinsic CT is consistent with the front and back measured CT indicating a majority of 1 SPAD events. This result clearly indicate that the excess of crosstalk observed in the SiPM is not associated to an effect inside the sensor bulk. On the contrary, the other sensors clearly present multi-SPAD signals when the MIP enters the SiPM from the front i.e. the photo sensitive side, with a large fraction of events with ≥ 4 SPADs firing. For particles coming from the back, it is also possible to notice

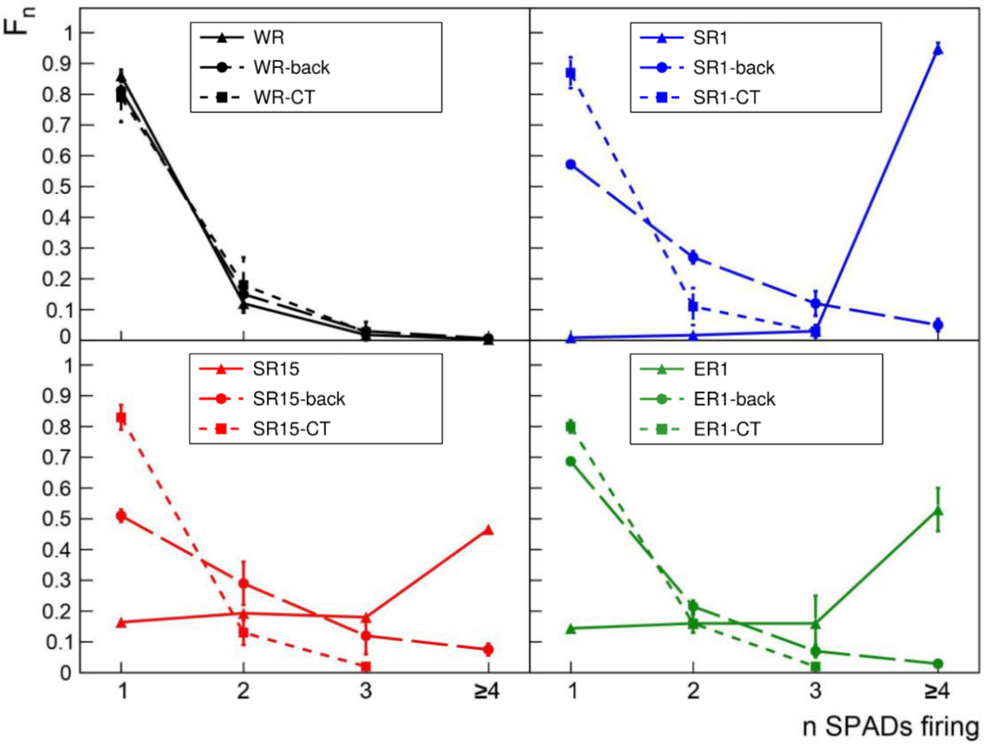

Figure 3.14: Measured CT factor F_n with respect to the number of SPADs firing for WR, SR1, SR15 and ER1 sensors at ~ 6 V OV. Square markers with long-dashed line indicate intrinsic CT measured in the region before the signal, triangle markers with continuous line indicate data with beam from the front of the sensor, circular markers with short-dashed line indicate data with beam from the back of the sensor.

	WR			SR1		
n	F_n (%)	F_n-back (%)	F_n-CT (%)	F_n (%)	F_n-back (%)	F_n-CT (%)
1	(86 ± 2)	(81.2 ± 1.1)	(79 ± 8)	(0.9 ± 0.2)	(57.2 ± 0.9)	(87 ± 5)
2	(12 ± 2)	(15 ± 4)	(18 ± 9)	(1.7 ± 0.7)	(27 ± 2)	(11 ± 6)
3	(1.8 ± 0.3)	(3 ± 3)	(2.7 ± 0.7)	(3 ± 2)	(12 ± 4)	(3.0 ± 1.0)
≥ 4	(0.35 ± 0.13)	(0.64 ± 0.15)	-	(94.9 ± 1.8)	(5 ± 2)	-
	SR15			ER1		
n	F_n (%)	F_n-back (%)	F_n-CT (%)	F_n (%)	F_n-back (%)	F_n-CT (%)
1	(16.4 ± 0.4)	(51 ± 2)	(83 ± 4)	(14.4 ± 0.5)	(68.7 ± 0.8)	(80 ± 2)
2	(19.3 ± 0.8)	(29 ± 7)	(13 ± 4)	(16 ± 3)	(21.5 ± 1.9)	(16 ± 3)
3	(17.8 ± 1.0)	(12 ± 6)	(2.0 ± 0.7)	(16 ± 9)	(7 ± 2)	(2.0 ± 1.0)
≥ 4	(46.6 ± 0.6)	(7.5 ± 1.9)	-	(53 ± 7)	(2.9 ± 1.2)	-

Table 3.5: Values of F_n for WR, SR1, SR15 and ER1 at an OV of ~ 6 V.

a shift of F_n to higher values of n with respect to the case of WR sensor: this could be related to reflections of photons inside the protection layer when the particle coming from the back traverses the resin on the opposite side. The intrinsic CT of all the SiPM are compatible.

These results clearly demonstrate the presence of Cherenkov light produced during the passage of the MIP through the protection layer. Due to the specific feature of the sensors that are built with the protection layer above all the different SiPMs of the six-SiPMs structure, a direct quantitative comparison among different samples can not be pursued as the alignment of the sensors could not be controlled with precision and particles impinging outside the sensor surface could produce a signal due to the observed Cherenkov effect.

3.4.2 Time resolution

The time resolution of the sensor was studied as a function of the number of SPADs firing in the SiPM: the results are shown for all the different samples at ~ 6 V of OV in Figure 3.15.

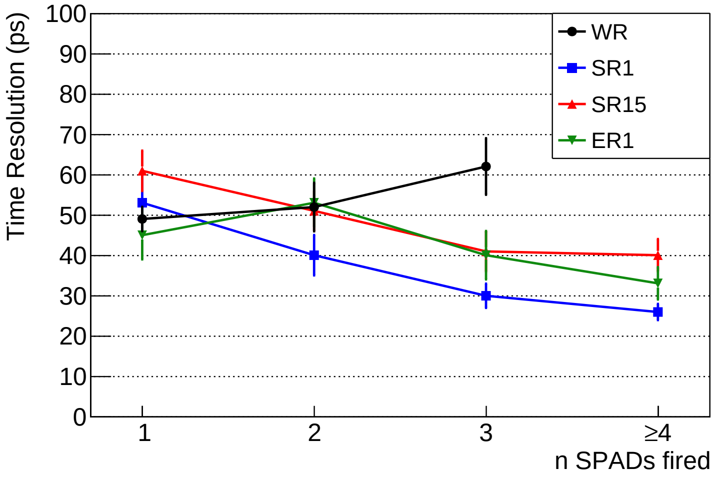

Figure 3.15: Time resolution as a function of the number of SPADs fired for the different SiPMs at an OV of ~ 6 V.

It is clear that the time resolution for the SiPMs with the protection layer improves with the number of fired SPADs since the signal amplitude is larger, reaching a value of 30-40 ps for ≥ 4 SPADs. The curve shows the same trend for all the SiPMs with protection resin. The WR sensor time resolution can be selected for at maximum 2 SPADs and the value at 3 corresponds to ≥ 3 SPADs firing. The WR is associated to a majority of single SPAD events: the time resolution of only one SPAD firing is compatible with the one obtained for the other SiPMs of $\sim$ 50-60 ps. When the number of fired SPADs increases the resolution of WR increases, showing an opposite trend with respect to the sensors with resin: this could be due to the fact that in this sensor multi-SPAD events are due only to crosstalk while in the other sensors these kind of events are associated to the Cherenkov photons produced by the MIP that trigger multiple SPADs simultaneously.

3.5 Results: measurements of the Cherenkov effect in direct detection of charged particles with SiPMs

The following results are obtained with data collected during the November 2022 beam test.

To better characterize the Cherenkov effect, a position scan of single SiPMs with different protection layers with the help of micropositioners was performed. For each type of sensor, two devices were studied. Having found the position of maximum signal with the position scan, the time resolution was studied at the proper scale on the oscilloscope. In the end, the beam energy was changed in order to evaluate the SiPM response via Cherenkov effect at lower energies.

3.5.1 Position scan of single SiPM

The position scan of SiPM was performed at 3 V of OV with a 200 mV/div scale on the digital oscilloscope to be able to detect all possible SPADs firing. The results are shown in Figure 3.16a and 3.16b for the X and Y direction respectively. The plots represent the mean amplitude of the signals as a function of the position of the sensor. Every curve is centered in the maximum of the mean signal amplitude. No cut on the minimum value of the amplitude is applied. Recall that the beam dimensions are defined by the LGAD trigger area of $1 \times 1 \text{mm}^2$. The results on the second sample tested for every type of SiPM prototype showed no measurable difference in both the X and Y directions.

It is clear that the average amplitude of sensors with protection resin is much higher with respect to the SiPM without resin, as expected with the presence of the Cherenkov effect. Even outside the sensor area, indicated by the dashed red lines at $[-0.5, +0.5]$ mm, their distributions present tails of larger amplitude with respect to WR. This happens because of photons belonging to the Cherenkov cone that are produced inside the protection layer but outside the sensor area. In addition to this, an asymmetry between the positive and the negative values of the X and Y position can be observed for the sensors with protection layer: this is due to the different border dimensions of the resin on the sensor. In particular, in the X direction the asymmetry is much more evident: a mean amplitude of 100 mV is reached on the negative values side at ~ -1 mm while on the positive values side at $\sim$ 1.2-1.4 mm. Indeed, this direction corresponds to the wire-bonding direction, along which the resin is 3.7 mm. The asymmetry along X can be noticed in particular for SR15-s, for which the Cherenkov cone has larger radius. In the Y direction, the asymmetry is less evident but still present: the mean amplitude of 100 mV is achieved on the negative values side at ~ -0.9 mm, while on the other side at ~ 1 mm, since the negative and positive values of Y respectively corresponds to 200 μm and 500 μm of resin outside the sensor area.

For the SiPMs with silicon protection, the mean amplitude of the sample with 1.5 mm resin, SR15-s, is larger than the one with 1 mm, SR1-s, on average: this is particularly evident along the X-direction outside the SiPM area, where the signal is mainly due to the contribution of the resin outside the sensor. Further more, when inside the SiPM area, the sample with epoxy resin shows a larger mean amplitude of about 100 mV with respect to the SiPM with silicon resin of same thickness, both in X and Y

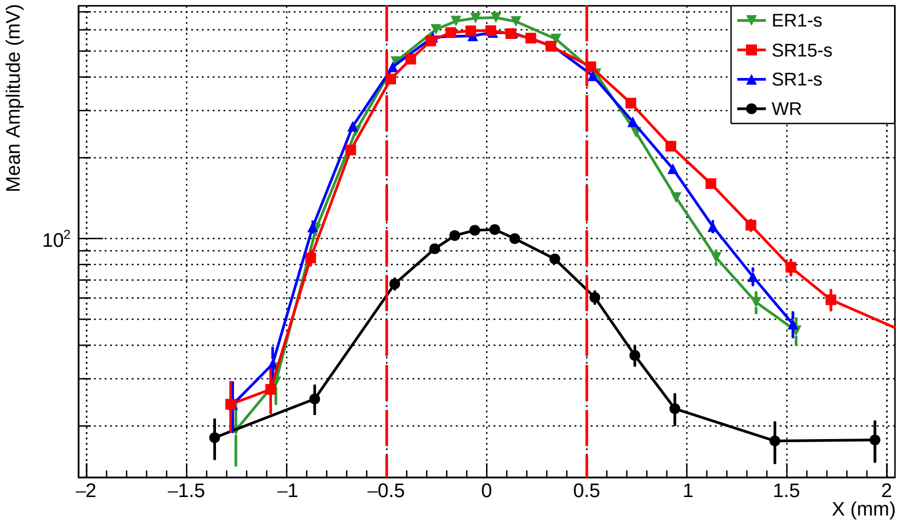

(a)

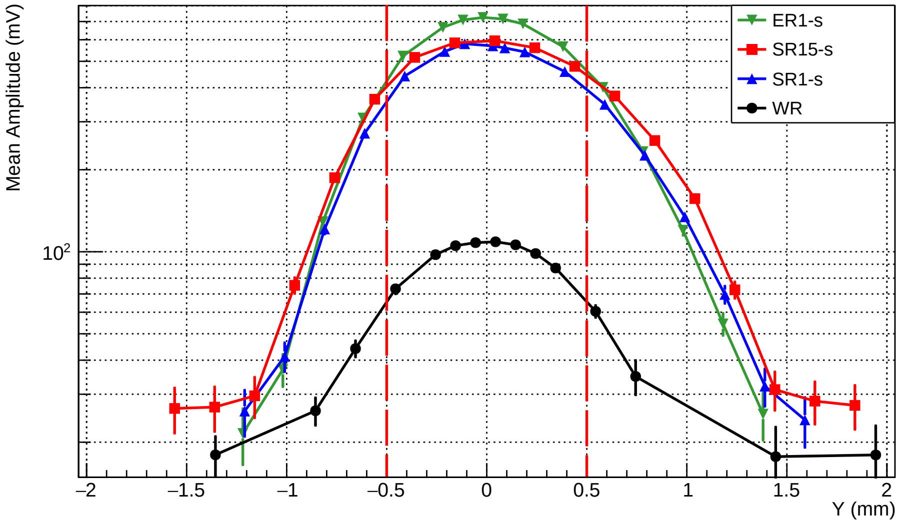

(b)

Figure 3.16: (a) Scan X of four independent single SiPMs (ER1-s, SR15-s, SR1-s and WR SiPM) mean signal amplitude along the long side of the resin (i.e. bonding direction); (b) Scan Y of four independent single SiPMs (ER1-s, SR15-s, SR1-s and WR SiPM) mean signal amplitude along the short side of the resin. The scan were performed at an OV of 3 V. The dashed red vertical lines at −0.5 mm and +0.5 mm indicate the SiPM area.

direction: this could be associated to the fact that epoxy has a higher refraction index of silicon and the Cherenkov cone produced by a MIP at same momenta has larger angle.

The WR sample is symmetric in both directions, confirming the fact that no Cherenkov light is produced i.e. only the area of the sensor and the LGAD trigger area influence the response: in Figure 3.17 a convolution of a step function built with the SiPM area and a Gaussian to account for the beam is evaluated for the scan along X. The fit, which is in good agreement with the data and shows a reasonably large probability, indicate a $\sigma_{beam} \simeq 0.42$ mm. The result is analagous and compatible within the errors for the Y direction. Considering the beam FWHM$\simeq$ 1 mm in each direction, the result is compatible with the expected area of the beam since this is associated to the LGADs trigger selection of about 1 mm^2.

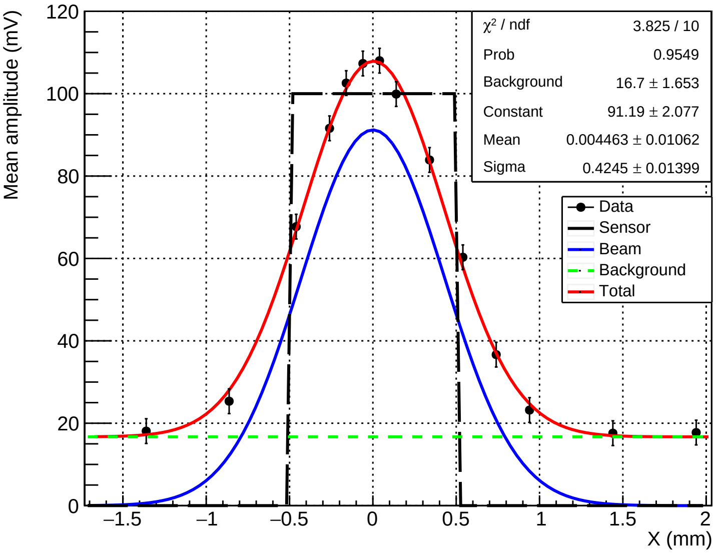

Figure 3.17: Scan X at 3 V of OV fitted with the convolution of a Gaussian function (to account for the beam spread, in blue), a step function (to account for the sensor active area, in black) and a background (due to noise and DCR, in green). The result of the fit (in red) is compared with the data.

Ideally, in Figure 3.16 the mean signal amplitudes of all the SiPMs far from the SiPM resin area i.e. the tails of the distributions should be reduced to a value made of simple DC events: however, due the whole extension of the beam along each direction considering $2\sigma_{beam}$, this results in a lit area of about $2 \times (2 \times 0.42) = 1.7$ mm hence 1.7×1.7 mm^2 which is bigger than the triggered area. For this reason, small differences can be observed among the baseline for WR sensor with respect to SR and ER SiPMs.

Thanks to the position scan, it was possible to collect the measurements of time resolution at the proper scale in the centre of the SiPM where the highest number of SPADs was firing. The time resolution study will be presented in Sec. 3.5.4.

3.5.2 Signal amplitudes

An example of signal amplitudes distribution after amplification and selection at 100 mV/div scale on the oscilloscope is shown for four single different SiPMs in Figure 3.18a and 3.18b respectively at an OV of 2 V and 4 V. The data are collected centering the beam in the middle of the sensor with the help of micropositioners after the position scan of Section 3.5.1.

The lower cut on the minimum value of signal amplitude is made considering a distance of 3σ from the mean value of the first firing SPAD. It is worth noticing that a large fraction of the signals for the sensors with resin are out of scale both at 2 and 4 V OV. The amplitudes are renormalized with multiplicative factors of the order of 15-20% of the signal amplitude of the SiPM in order to account for small differences in the gain of the samples. For this reason on the x-axis the values of amplitudes are reported in a.u.

The histograms are normalized to the total number of events. The mean number of firing SPADs for the sensors with resin at an OV of 2 V is $\sim$ 6-7, while at an OV of 4 V is ~ 8. WR mean value of firing SPADs is, in both cases, ~ 1. The difference between the sample without resin and the SiPMs with resin is clear: WR has a majority of 1 SPAD events, with some CT giving signals up to 4-5 SPADs, while ER1-s, SR15-s and SR1-s show a majority of multi-SPAD events. It is worth noticing that ER1-s shows at high number of SPADs an enhanced response with respect to SR15-s and SR1-s at both the values of OV. Indeed, because of a higher refraction index, the Cherenkov cone is lightly larger, as observed with the position scan in Section 3.5.1.

The enhanced Cherenkov effect is not as evident for SR15-s and SR1-s, even if, both at 2 and 4 V of OV, SR15-s shows a mean amplitude larger than SR1-s of about 30 mV. This difference can be appreciated also in Section 3.5.3, where SR15-s and SR1-s were tested at lower beam energies.

3.5.3 SiPM response at lower beam energies

In order to better study the Cherenkov effect produced in the protection layers of the sensors, the beam was set to momentum 1.0 and 1.5 GeV/c. The beam composition as a function of momentum strongly varies: it goes from 70-20% p/π at 10 GeV/c, to 20/50/10% p/π/electron at 2.0 GeV/c, to 15/35/35 p/π/electron at 1.0 GeV/c. A TOF measurement with the LGADs placed at $\sim$ 24 cm was then performed in order to select only protons and be able to do a comparison of the SiPM response at different energies. The experimental setup consisted then of two LGADs and two SiPMs, one SR1-s and one SR15-s. For this analysis, being the time resolution not of interest, a 90% CFD on LGAD signals was considered.

The TOF distribution at 1.0 and 1.5 GeV/c is shown respectively in Figure 3.19a and 3.19b. The curve is fitted considering the sum of two q-Gaussian distributions. The peak on the right represents protons while the peak on the left corresponds to electrons and pions. The separation at 1.0 GeV/c is $\simeq$ 290 ps while at 1.5 GeV/c is $\simeq$ 150 ps. In order to compare the response of SR15-s and SR1-s at different energies with a low background and, at the same time, a sufficient number of entries, the cut to discriminate electrons and pions from protons is made considering a distance of $3\sigma_1$ from the mean of the electrons/pions peak. At 1.0 GeV/c, for values of time difference > 0.4 ns, the

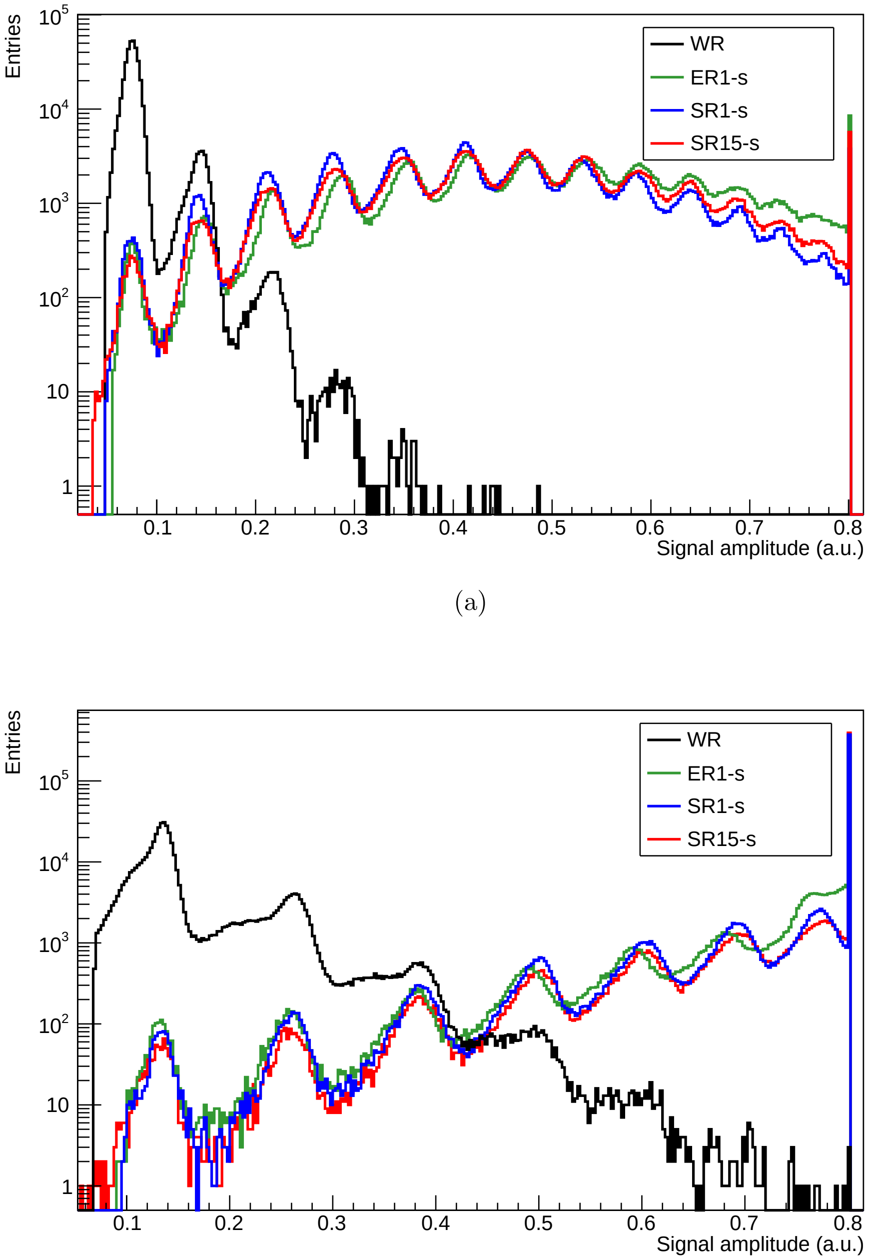

(a)

(b)

Figure 3.18: Example of MIPs signals amplitudes, after amplification and selection in the centre of the position scan, measured for single SiPM without resin (WR), SiPM with silicon resin of 1.5 mm resin (SR15-s) and of 1 mm (SR1-s) and SiPM with epoxy resin of 1 mm (ER1-s) at an OV of 2 V and (b) 4 V. The distributions are normalized to the total number of events and the lower cut is made considering 3σ from the mean of the first firing SPAD for every SiPM.

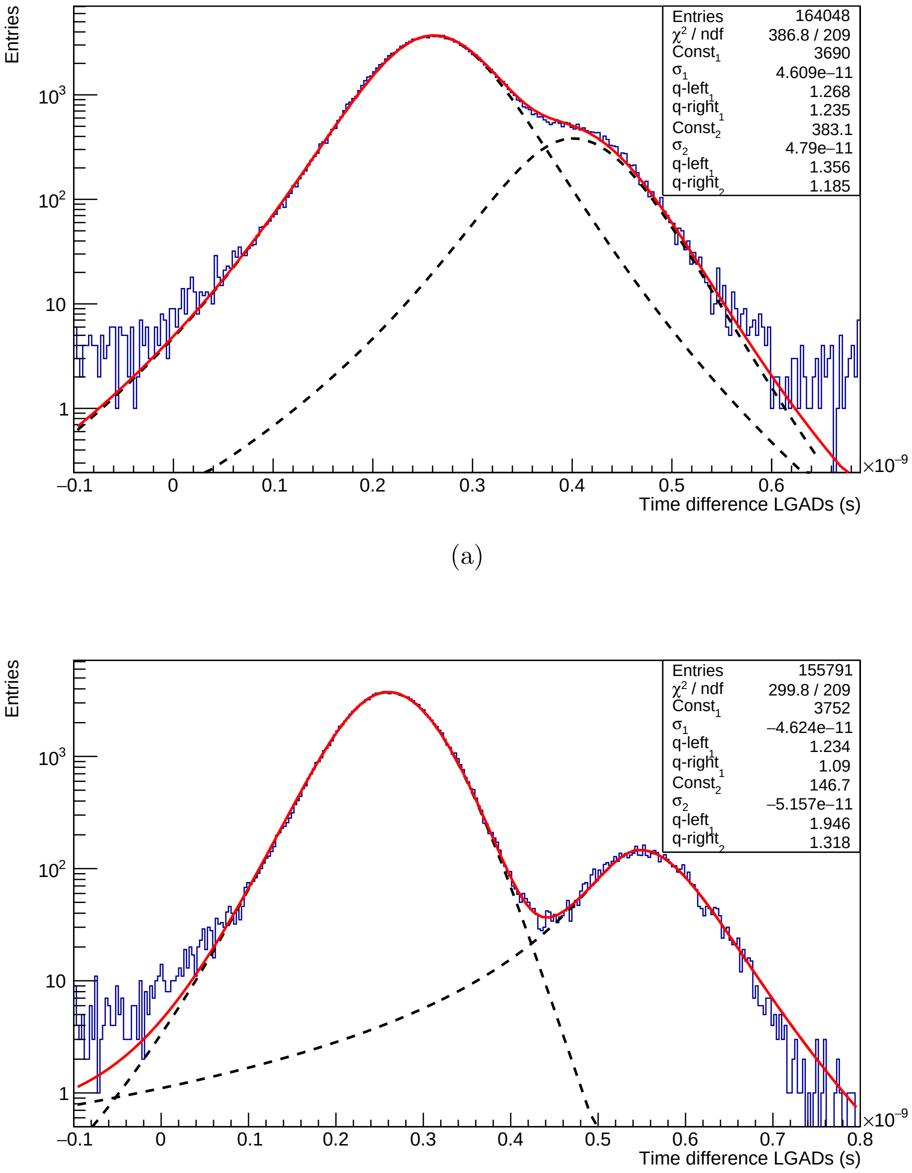

(a)

(b)

Figure 3.19: TOF of the beam particles computed as the time difference between the two LGDAS at (a) 1.5 GeV/c and (b) 1.0 GeV/c. The fit are performed with two q-Gaussians.

events associated to protons are 4017 and 4064 for SR1-s and SR15-s respectively. At 1.5 GeV/c, considering values of time difference between 0.40 ns and 0.68 ns, the tagged protons are 6420 for SR1-s and 6894 for SR15-s. Doing so, the purity of the tagged protons sample is estimated to be $\simeq 84\%$ at 1.5 GeV/c and $\simeq 82\%$ at 1.0 GeV/c.

In order to have a purer sample of protons, another study is considered evaluating also the sum of the time of arrival of the MIP in the LGADs. The resulting two-dimensional plots, which are called “2D” TOF plots, are shown in Figure 3.20b and 3.20a: here, on the x-axis there is the time difference between the LGADs signals while on the y-axis the

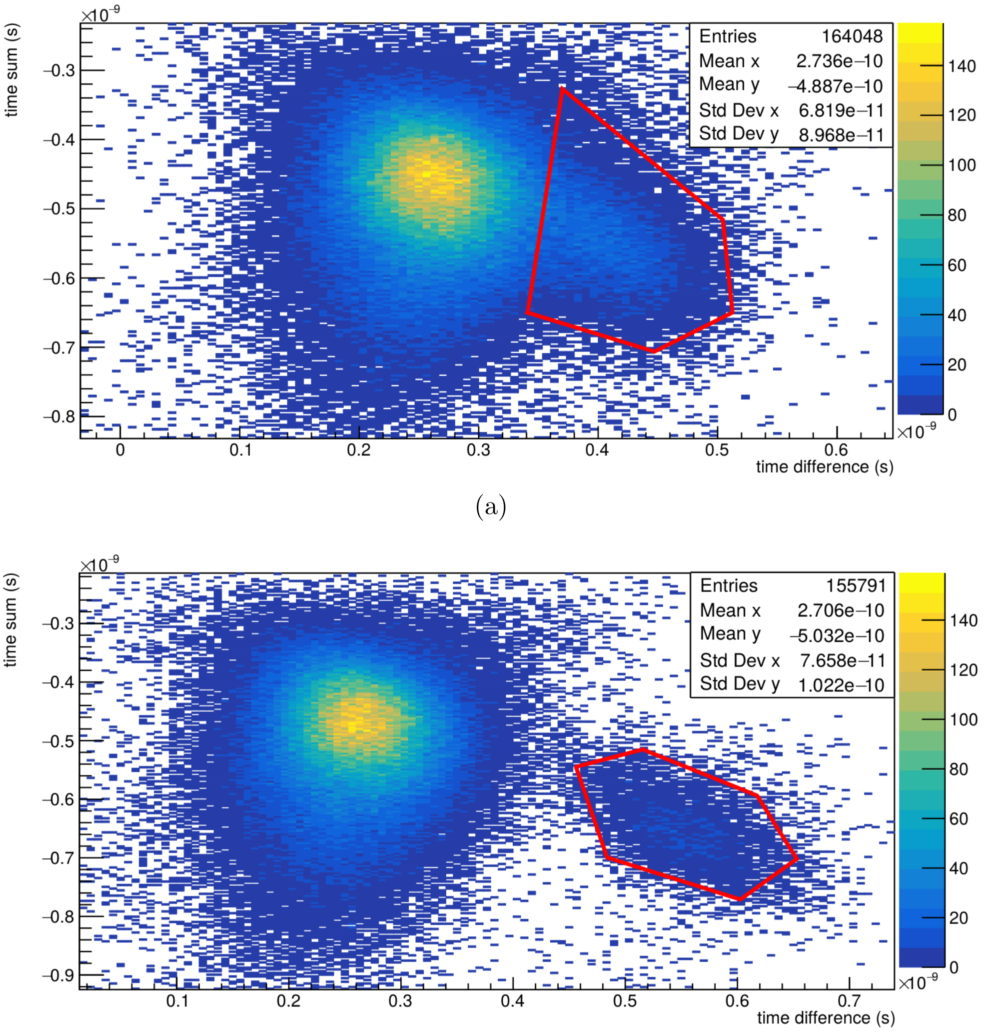

(a)

(b)

Figure 3.20: 2D TOF at (a) 1.5 GeV/c and (b) 1.0 GeV/c. On the x-axis there is the time difference between the two LGADs, on the y-axis the sum. The red polygonal line represents the cut made in order to select protons.

sum of the time of the same signals. A poligonal function is used to select only protons. This resulted for SR1-s and SR15-s respectively in 2815 and 2863 selected protons at 1.0 GeV/c, while 11123 and 12125 at 1.5 GeV/c.

Considering the events selected with 3.19a and 3.19b, the response of SiPM at the passage of tagged protons was measured: in Figure 3.21a and 3.21b the amplitudes of signals for 12, 1.5 and 1.0 GeV/c are reported respectively for SR1-s and SR15-s. For each energy, the histogram reports a number of entries equal to the number of events associated to protons at 1.0 GeV/c. Similar results are obtained using the selections of Figures 3.20a and 3.20b.

These plots show that the number of fired SPADs decreases significantly at 1.0 GeV/c, both for SR1-s and SR15-s. Indeed, the mean values of both SR1-s and SR15-s indicate at 12 and 1.5 GeV/c about 6 SPADs firing, while at 1.0 GeV/c 4 SPADs firing.

The mean values of SR15-s are slightly larger than the ones of SR1-s of $\sim$ 50 mV,

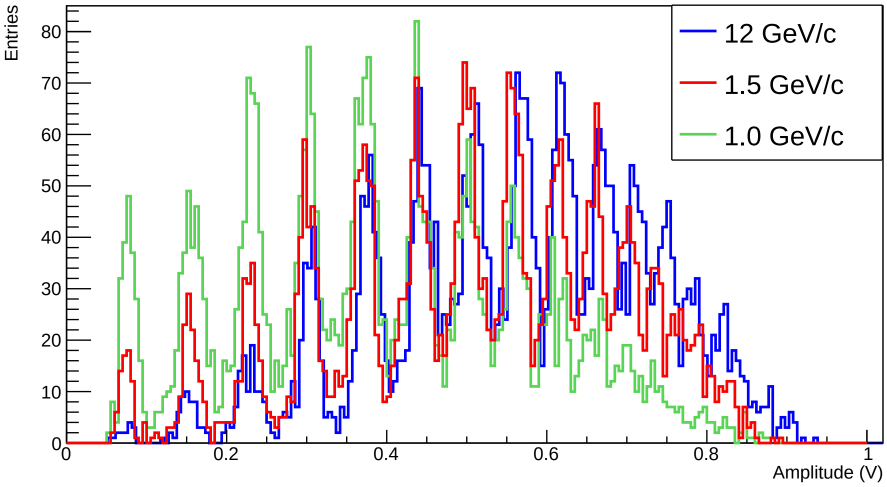

(a)

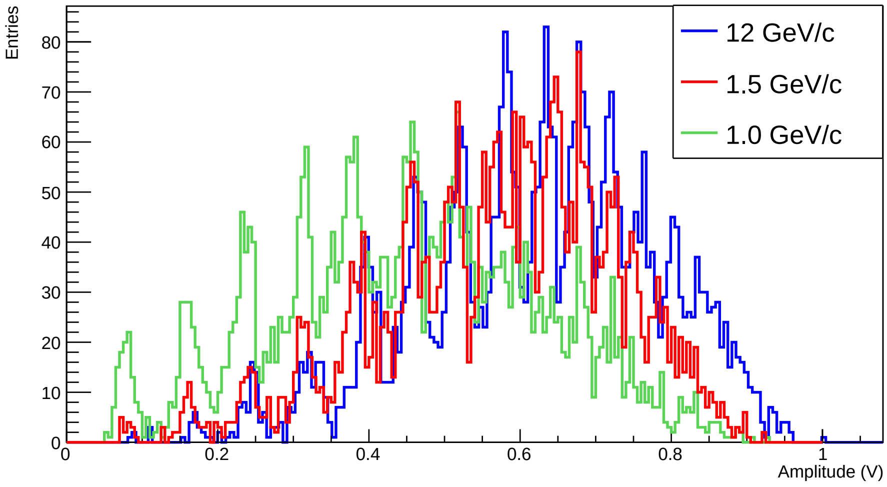

(b)

Figure 3.21: Amplitude of protons signals at different beam energies for (a) SR1-s and (b) SR15-s. The data are collected at 3 V OV with 200 mV/div vertical scale on the oscilloscope.

confirming an enhanced Cherenkov effect due to a larger width of the protection layer i.e. a larger Cherenkov cone.

3.5.4 Time resolution

At 12 GeV/c the time resolution was studied for all samples.

The timing response was studied both considering all waveforms and as a function of the number of firing SPADs. The amplitude scale on the oscilloscope was set in order to acquire a number of SPADs of at maximum ~ 8. The results on the time resolution are reported considering for every SiPM the mean of the two tested SiPMs of same type.

In Figure 3.22 the time resolution at a fixed threshold of 20% SPAD signal amplitude for the four type of independent SiPMs is reported. For the SiPM with protection resin the resolution decreases from about 40 to 20 ps as the OV increases. The sample without resin has a time resolution of about 65-75 ps. The difference in the trend of the SiPM with and without resin may be due to DCR and the type of MIP signals produced in the different SiPMs. An increase in the OV means also an increasing in DCR (see Section 2.4.4). But, as the majority of SR1-s, SR15-s and ER1-s signals are multi-SPAD events, these are not affected by a higher DCR. On the other hand, the SiPM without resin has a majority of 1 SPAD events that are more influenced by DC events (a hint of this behaviour was also observed with a limited data set during the threshold scan reported in Section 3.3.3).

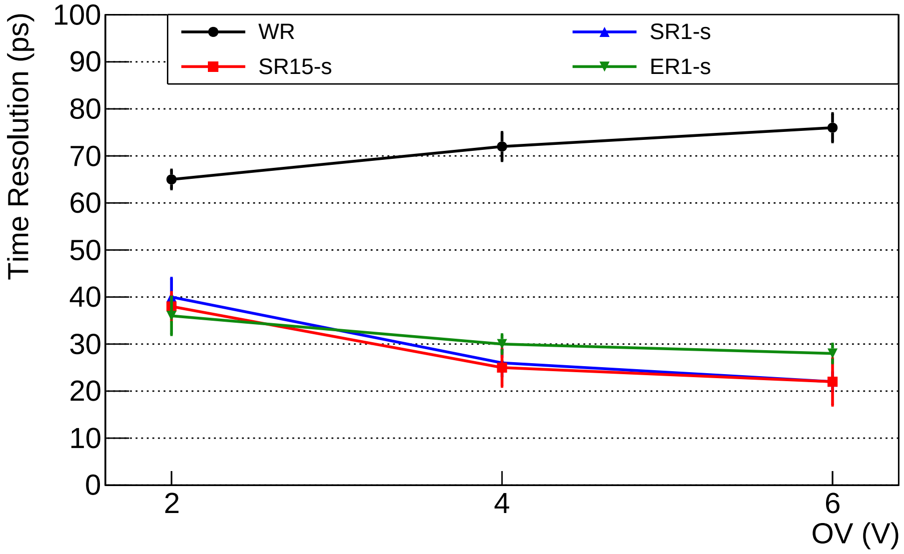

Figure 3.22: Time resolution of every tested SiPM (WR, SR15-s, SR1-s and ER1-s) at 2, 4 and 6 V of OV computed as the mean of the two samples of the same type of SiPM considering all the waveforms.

The time resolution is then studied selecting a fixed number of fired SPADs at 2, 4 and 6 V of OV. The selection of a number of SPADs is made considering the middle of the plateau between two adjacent distributions of signal amplitudes. The results at 4 V OV are shown in Figure 3.23.

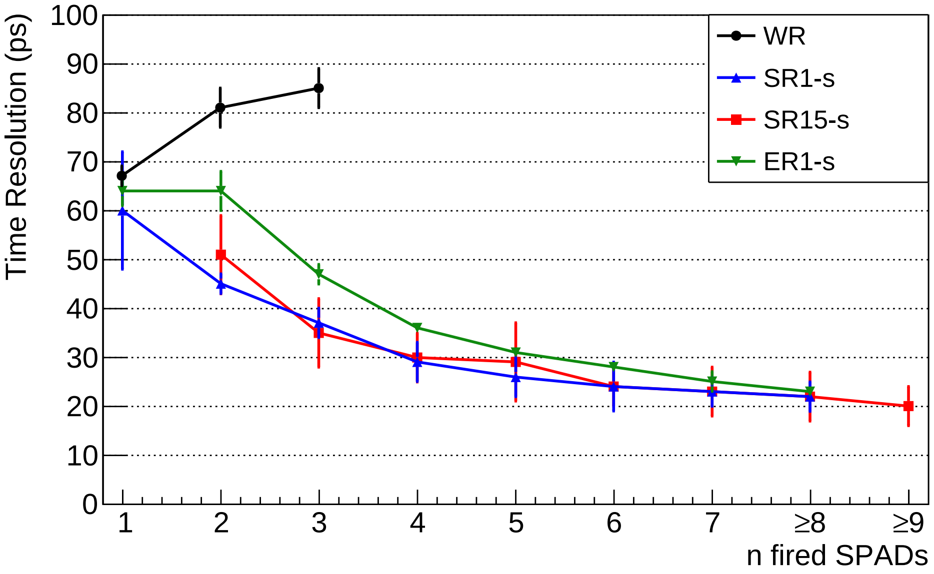

Figure 3.23: Time resolution as a function of the number of SPADs fired for the different single SR1-s, SR15-s, ER1-s and WR at an OV of 4 V. The resolution is computed as the mean of the two samples of the same type of SiPM.

In Figure 3.23, the last time resolution value with respect to the number of fired SPADs can be obtained until the number of the fired SPADs itself can be selected by looking at the signals amplitude. A higher number of fired SPADs is associated then to all the waveforms which exceed the last recognizable fired SPADs number. For example, at 4 V OV SR15-s time resolution could be clearly evaluated selecting until 8 complete SPADs, all the remaining events are then considered inside ≥ 9 fired SPADs. At same OV, SR1-s and ER1-s time resolution could be evaluated selecting at maximum 7 complete SPADs, while 8 comprehends all waveforms above this value. Clearly, the sample without resin could only be evaluated for 1, 2 and ≥ 3 fired SPADs. It is also worth noticing that the time resolution at 1 SPAD could not be evaluated for all the SiPM as there was not sufficient statistics to perform a reasonable fit on the data.

In Figure 3.24 the results of the time resolution of every type of SiPM at 2, 4 and 6 V of OV are shown, whose exact values are reported in Table 3.6, 3.7 and 3.8. In addition to the time resolutions, an estimation of the fraction of events between n firing SPADs and the total number of firing SPADs is reported in percentage. This variable was introduced in Section 3.4.1 as F_n.

For the SiPMs with protection resin it is evident that the time resolution decreases as the number of fired SPADs increases. Their time resolution value at 1 SPADs is $\sim$ 60-70 ps, a value compatible with the time resolution of the sample without resin, while for ≥ 6 fired SPADs the resolution goes down to 20-30 ps.

On the other hand, the sample without resin features a time resolution that increases as the number of fired SPADs increases: this may be associated to the fact that events

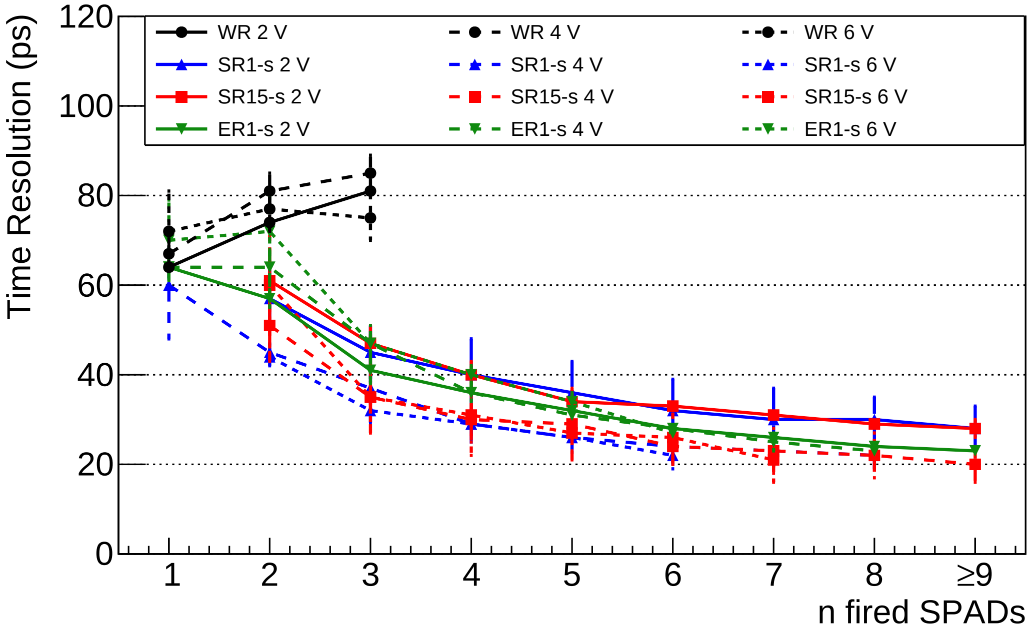

Figure 3.24: Time resolution as a function of the number of fired SPADs for the different single SR1-s, SR15-s, ER1-s and WR. Continous lines correspond to an OV of 2 V, long-dashed lines to 4 V and short-dashed lines to 6 V.

	SR15-s		SR1-s		ER1-s		WR	
n	σ (ps)	F_n (%)	σ (ps)	F_n (%)	σ (ps)	F_n (%)	σ (ps)	F_n (%)
1	-	< 1	-	< 1	(64 ± 1)	$\sim$1	(64 ± 1)	$\sim$92
2	(61 ± 7)	$\sim$2	(57 ± 7)	$\sim$3	(57 ± 2)	$\sim$3	(74 ± 1)	$\sim$8
3	(47 ± 4)	$\sim$5	(45 ± 6)	$\sim$7	(41 ± 3)	$\sim$6	(81 ± 1)	< 1
4	(40 ± 3)	$\sim$9	(40 ± 8)	$\sim$9	(36 ± 2)	$\sim$10	-	-
5	(34 ± 2)	$\sim$12	(36 ± 7)	$\sim$13	(32 ± 1)	$\sim$14	-	-
6	(33 ± 1)	$\sim$16	(32 ± 7)	$\sim$14	(28 ± 1)	$\sim$15	-	-
7	(31 ± 1)	$\sim$15	(30 ± 7)	$\sim$16	(26 ± 1)	$\sim$12	-	-
8	(29 ± 1)	$\sim$13	(30 ± 5)	$\sim$12	(24 ± 1)	$\sim$12	-	-
9	(28 ± 2)	$\sim$27	(28 ± 5)	$\sim$25	(23 ± 1)	$\sim$26	-	-

Table 3.6: Time resolution with respect to a selected number of firing SPADs of different type of SiPMs at 2 V OV. The percentage F_n is associated to the rounded mean fraction of events relative to the selected SPAD for every type of SiPM. The last time resolution value associated to a number of fired SPADs n is intendend to be for signals with $\geq n$ SPADs firing (for example, 9 stands for ≥ 9 for SR15-s).

	SR15-s		SR1-s		ER1-s		WR	
n	σ (ps)	F_n (%)	σ (ps)	F_n (%)	σ (ps)	F_n (%)	σ (ps)	F_n (%)
1	-	< 1	(60 ± 12)	< 1	(64 ± 3)	< 1	(67 ± 2)	$\sim$78
2	(51 ± 8)	< 1	(45 ± 2)	< 1	(64 ± 4)	< 1	(81 ± 4)	$\sim$18
3	(35 ± 7)	< 1	(37 ± 3)	$\sim$1	(47 ± 2)	$\sim$1	(88 ± 4)	$\sim$4
4	(30 ± 5)	$\sim$2	(29 ± 4)	$\sim$3	(36 ± 1)	$\sim$3	-	-
5	(29 ± 8)	$\sim$3	(26 ± 4)	$\sim$5	(31 ± 1)	$\sim$5	-	-
6	(24 ± 4)	$\sim$5	(24 ± 5)	$\sim$7	(28 ± 1)	$\sim$7	-	-
7	(23 ± 5)	$\sim$7	(23 ± 3)	$\sim$9	(25 ± 2)	$\sim$10	-	-
8	(22 ± 5)	$\sim$9	(22 ± 3)	$\sim$75	(23 ± 1)	$\sim$72	-	-
9	(20 ± 4)	$\sim$73	-	-	-	-	-	-

Table 3.7: Time resolution with respect to a selected number of firing SPADs of different type of SiPMs at 4 V OV. The percentage F_n is associated to the rounded mean fraction of events relative to the selected SPAD for every type of SiPM. The last time resolution value associated to a number of fired SPADs n is intendend to be for signals with $\geq n$ SPADs firing (for example, 8 stands for ≥ 8 for SR1-s).

	SR15-s		SR1-s		ER1-s		WR	
n	σ (ps)	F_n (%)	σ (ps)	F_n (%)	σ (ps)	F_n (%)	σ (ps)	F_n (%)
1	-	< 1	-	< 1	(70 ± 9)	< 1	(72 ± 9)	$\sim$75
2	(60 ± 15)	< 1	(44 ± 2)	< 1	(72 ± 8)	< 1	(77 ± 5)	$\sim$19
3	(35 ± 8)	< 1	(32 ± 3)	< 1	(47 ± 4)	< 1	(75 ± 5)	$\sim$6
4	(31 ± 9)	< 1	(29 ± 4)	< 1	(40 ± 2)	$\sim$1	-	-
5	(27 ± 4)	$\sim$1	(26 ± 1)	$\sim$1	(34 ± 2)	$\sim$2	-	-
6	(26 ± 6)	$\sim$2	(22 ± 2)	$\sim$97	(27 ± 1)	$\sim$95	-	-
7	(21 ± 5)	$\sim$96	-	-	-	-	-	-

Table 3.8: Time resolution with respect to a selected number of firing SPADs of different type of SiPMs at 6 V OV. The percentage F_n is associated to the rounded mean fraction of events relative to the selected SPAD for every type of SiPM. The last time resolution value associated to a number of fired SPADs n is intendend to be for signals with $\geq n$ SPADs firing (for example, 6 stands for ≥ 6 for SR1-s).

with ≥ 2 SPADs firing are due to intrinsic CT and not to MIP events and also to the fact that statistics drastically reduces at ≥ 3 fired SPADs (see comments at Figure 3.22).

At 6 V OV, all the time resolutions are consistent within the errors to the resolutions obtained during the July beam test reported in Section 3.4.2.

Finally, looking at Tables 3.7 and 3.8 it is interesting to notice the following. Putting a threshold corresponding to ≥ 4 SPADs, all the noise due to DCR and correlated would be excluded keeping an efficiency larger or equal than 99% for all the SiPMs with resin. This result might be of particular interest not for a direct detection of charged particles. Furthermore, if the timing layer is considered in combination with a RICH detector (see Section 1.3.4) a double-threshold method might be of interest.

Conclusions

In this thesis, a study on SiPM response to the passage of charged particles is reported. The SiPM devices were studied during two different beam tests at the CERN T10 beamline, one in July and one in November 2022.

The study performed during the July beam test aimed at understanding the origin of an unexpected higher number of the SiPM cells with signals i.e. a higher crosstalk with respect to the one associated to intrinsic noise events in the bulk of the sensor. This was originally observed in [3]. This effect could have been attributed to processes in the bulk of the sensor or to Cherenkov or scintillation effect associated to the passage of the particle through the protective layer of the SiPM.

In the July beam test, four different type of SiPMs were provided by FBK as part of a matrix structure with six SiPMs: one type without and three with different, in thickness and material, resin protection layers. By comparing the number of fired cells when the particles were impinging the detector from the photosensitive side and when impinging from the PCB side, the results clearly indicated the production of many photons via Cherenkov light emission at the passage of the MIP through the protection layer. On the contrary, a single charged particle passing through the SiPM without any protection layer gave a signal corresponding to a single SPAD firing, in addition to standard crosstalk. The higher number of SPADs firing has then an important benefit in terms of efficiency (the SiPM geometrical fill factor becomes not important) and time resolution. Indeed, the resolution reached a value of 30-40 ps for ≥ 4 number of SPADs fired in the SiPM. The results of the July beam test are also reported in [56].

During the November beam test, the Cherenkov effect was better characterized. This was done using prototypes of single SiPMs, not part of a matrix structure, with a rectangular protective layer of resin above the sensor. Again, different type of resins, in thickness and material, were provided by FBK. Thanks to an accurate position scan of the SiPM, it was possible to better study the Cherenkov light emission inside the protection layer. The measurements confirmed the strong production of photons due to the Cherenkov effect in the layers and allowed to appreciate differences related to the SiPM protection layer features: indeed, a larger production of photons was observed for thicker resin layers, related to a larger radius of the Cherenkov cone. Futhermore, the effect of the Cherenkov threshold for protons was observed reducing the beam energy from 12 to 1.5 and 1.0 GeV/c. Finally, the timing response was measured indicating a value of about 20-30 ps for ≥ 6 number of SPADs fired in the SiPM. Within the errors, this improvement of the time resolution is independent of the overvoltage applied to the SiPM.

In the future, it would be important to repeat these measurements with larger SiPM matrices in order to evaluate the amount of photons actually produced in the layer, now limited by the dimensions of the SiPM. Because the Cherenkov cone is wide, it can cover several SiPMs of the matrix built on the same board. Having the signal spread over several adjacent SiPMs may increase the signal associated to the passage of the MIP, further improving the signal to noise ratio and the time resolution. Moreover, the effect of radiation damage should be better quantified, also in terms of time resolution.

In conclusion, the study showed promising results and paves the way for moving SiPMs from photosensors to charged particles detectors with excellent time resolution. The SiPM could then represent a possible candidate for the timing layers of ALICE 3, which require a time resolution of $\simeq 20$ ps, and have other important applications in the next-generation RICH counters or in TOF counters for experiments in space.

Appendix: Cherenkov radiation

The primary interactions of charged particles with silicon happen mainly via inelastic collisions with the atomic electrons of the medium and elastic scattering from nuclei. These, however, are not the only reactions that can occur (we have seen, for example, Bremmstrahlung radiation for electrons and positrons): indeed, another possible interaction process of charged particles in silicon is the emission of Cherenkov radiation. Cherenkov radiation occurs when a charged particle in a material medium moves faster than the speed of light in that medium, which is $v_n = c/n$ with n refraction index of that medium i.e. velocity of the particle v is higher than v_n and the critical value of $\beta = v/c$ must be greater than $\beta_{th} = 1/n$.

An electromagnetic shock wave is created and the coherent wavefront formed is emitted in a conical shape at an angle which satisfies

$$\cos\theta = \frac{1}{\beta n} \tag{3}$$

as can be schematically seen in Fig.25. The cone, when projected on a planar surface, defines a ring whose radius can be measured with photosensitive sensors so θ and β of the particle can be obtained.

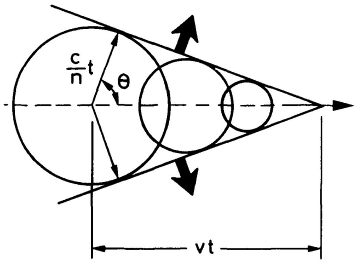

Figure 25: Cherenkov radiation consists of an electromagnetic shock wave produced when the particle travels faster than c in the medium. θ is the Cherenkov angle while $c/n = v_n$ [25].

Of interest for the detectors design is the number of photons N emitted when a particle passes through the radiating medium: in terms of wavelength λ

$$\frac{d^2N}{d\lambda dx} = \frac{2\pi\alpha z^2}{\lambda^2}\sin^2\theta \tag{4}$$

where α is the fine structure constant and z is the charge of the particle. We see then that Cherenkov radiation is mainly emitted in the UV region. If we consider a typical range of sensitivity of a photon detector in the visible and near-UV (N-UV) wavelengths 350-550nm, we see that the mean number of emitted photons is equal to

$$\frac{dN}{dx} = 2\pi\alpha z^2 \sin^2\theta \int_{\lambda_1}^{\lambda_2} \frac{d\lambda}{\lambda^2} = 475 z^2 \sin^2\theta \text{ photons/cm} \tag{5}$$

The energy loss by this process is of the order of 0.5 keV/cm.

Bibliography

[1] P. Lecoq, S. Gundacker, *SiPM applications in positron emission tomography: toward ultimate PET time-of-flight resolution*, Eur. Phys. J. Plus (2021) http://dx.doi.org/10.1140/epjp/s13360-021-01183-8.

[2] S. Gundacker, A. Heering, *The silicon photomultiplier: fundamentals and applications of a modern solid-state photon detector*, Phys. Med. Biol. 65 17TR01 (2020) https://doi.org/10.1088/1361-6560/ab7b2d.

[3] F. Carnesecchi et al., *Direct detection of charged particles with SiPMs*, Journal of Instrumentation 17(P06007) (2022) https://doi.org/10.1088/1748-0221/17/06/P06007.

[4] ALICE Collaboration, *Letter of intent for ALICE 3: A next-generation heavy-ion experiment at the LHC* CERN-LHCC-2022-009 / LHCC-I-038 (2022) https://cds.cern.ch/record/2803563.

[5] The ALICE collaboration, *The ALICE experiment at the CERN LHC*, JINST 3 S08002 (2008) https://dx.doi.org/10.1088/1748-0221/3/08/S08002.

[6] M. Lamont et al., LHC Performance Workshop (2022) Indico event 1097716 http://lhc-commissioning.web.cern.ch/schedule/LHC-long-term.htm.

[7] The ALICE collaboration, *ALICE upgrades during the LHC Long Shutdown 2*, CERN-EP-2023-009 (2023) https://doi.org/10.48550/arXiv.2302.01238.

[8] A. Andronic et al., *Heavy-flavour and quarkonium production in the LHC era: from proton-proton to heavy-ion collisions*, (2015) https://doi.org/10.1140/epjc/s10052-015-3819-5.

[9] U. Heinz, *The Little Bang: Searching for quark-gluon matter in relativistic heavy-ion collisions*, CERN-TH/2000-276 (2000) https://doi.org/10.48550/arXiv.hep-ph/0009170.

[10] M. G. Mustafa, *Quark–Gluon plasma and heavy-ion phenomenology*, Eur. Phys. J. Spec. Top.230 603–605 (2021) https://doi.org/10.1140/epjs/s11734-021-00018-y.

[11] The ALICE collaboration, *Letter of intent for an ALICE ITS upgrade in LS3*, ALICE-PUBLIC-2018-013 (2018) http://dx.doi.org/10.17181/CERN-LHCC-2019-018.

[12] R. Arnaldi et al. (NA60 Collaboration), *First Measurement of the ρ Spectral Function in High-Energy Nuclear Collisions*, Phys. Rev. Lett. 96, 162302 (2006) https://doi.org/10.1103/PhysRevLett.96.162302.

[13] ALICE Collaboration, *Direct photon production in Pb-Pb collisions at* $\sqrt{s_{NN}} = 2.76$ *TeV*, CERN-PH-EP-2015-254 (2016) https://doi.org/10.1016/j.physletb.2016.01.020.

[14] F. Low, *Bremsstrahlung of very low-energy quanta in elementary particle collisions*, Phys. Rev. 110, 974-977 (1958) https://doi.org/10.1103/PhysRev.110.974.

[15] R. Turchetta, *CMOS Monolithic Active Pixel Sensors (MAPS) for future vertex detectors* (2006) https://doi.org/10.48550/arXiv.physics/0605238.

[16] R. Turchetta et al., *CMOS Monolithic Active Pixel Sensors (MAPS): developments and future outlook*, Nuclear Inst. and Methods in Physics Research, Vol. 582, 3 (2007) https://doi.org/10.1016/j.nima.2007.07.112.

[17] D. Colella on behalf of the ALICE Collaboration, *ALICE ITS 3: the first truly cylindrical inner tracker* (2022) https://doi.org/10.1088/1748-0221/17/09/C09018.

[18] C. Lippmann, *Particle Identification* (2018) https://doi.org/10.1016/j.nima.2011.03.009.

[19] M.P. Casado on behalf of ATLAS HGTD Group, *A High-Granularity Timing Detector for the ATLAS Phase-II upgrade*, Nuclear Inst. and Methods in Physics Research, Vol. 1032 (2022) https://doi.org/10.1016/j.nima.2022.166628.

[20] CMS, *A MIP Timing Detector for the CMS Phase-2 Upgrade*, Tech. Rep. CERN-LHCC-2019-003. CMS-TDR-020 (2019) https://cds.cern.ch/record/2667167.

[21] K. Inami et al., *A TOF counter of* $\sigma \sim 10ps$ *with Cherenkov Photons and a MCP-PMT*, IEEE Symposium Conference Record Nuclear Science, Vol. 3 (2004) https://doi.org/10.1109/NSSMIC.2004.1462627.

[22] S. Korpar et al.,*A module of silicon photo-multipliers for detection of Cherenkov radiation*, NIM Vol. A613 Issue 2 pag. 195-199 (2010) https://doi.org/10.1016/j.nima.2009.11.043.

[23] Y. Tao, A. Rajapakse, A. Erickson, *Advanced antireflection for back-illuminated silicon photomultipliers to detect faint light*, Scientific Reports 12, 13906 (2022) https://doi.org/10.1038/s41598-022-18280-y.

[24] A.B. Sproul, M.A. Green, *Improved value for the Silicon intrinsic carrier concentration from 275 to 375 K*, Journal of Applied Physics 70, 846 (1991) https://doi.org/10.1063/1.349645 .

[25] W.R. Leo, *Techniques for Nuclear and Particle Physics Experiments*, 2nd Rev., Springer Berlin-Heidelberg (1994) https://doi.org/10.1007/978-3-642-57920-2.

[26] G. F. Knoll, *Radiation Detection and Measurement*, 3rd Ed., John Wiley and Sons (2000) https://doi.org/10.1103/PhysRevD.98.030001.

[27] M. Tanabashi et al. (Particle Data Group), *Review of Particle Physics*, Phys. Rev. D 98, 030001 (2018).

[28] R.L. Workman et al. (Particle Data Group) Review of Particle Physics, Prog. Theor. Exp. Phys., Vol. 2022, Issue 8, 083C01 (2022) https://doi.org/10.1093/ptep/ptac097.

[29] F. Berghmans et al., *An Introduction to Radiation Effects on Optical Components and Fiber Optic Sensors*, Optical Waveguide Sensing and Imaging (2007) http://dx.doi.org/10.1007/978-1-4020-6952-9-6.

[30] M. A. Green, *Self-consistent optical parameters of intrinsic silicon at 300 K including temperature coefficients*, Solar Energy Materials & Solar Cells 92 (2008) https://doi.org/10.1016/j.solmat.2008.06.009.

[31] G. Graaf, R. F. Wolffenbuttel, *Illumination Source Identification Using a CMOS Optical Microsystem*, IEEE Transactions on Instrumentation and Measurement 53, 2 (2004) http://dx.doi.org/10.1109/TIM.2003.822476.

[32] H. Spieler, *Semiconductor Detector Systems*, vol. v.12 of Semiconductor Science and Technology, Oxford University Press, Oxford (2005).

[33] F. Carnesecchi, *Experimental study of the time resolution for particle detectors based on MRPC, SiPM and UFSD technologies*, Università di Bologna, Physics PhD thesis (2018) http://amsdottorato.unibo.it/id/eprint/8538.

[34] H. Spieler, *Analog and Digital Electronics for Detectors*, Physics Division, Lawrence Berkeley National Laboratory Berkeley, California 94720, U.S.A.

[35] W. Shockley, *Currents to conductors induced by a moving point charge*, J. Appl. Phys. 9 (1938) https://doi.org/10.1063/1.1710367.

[36] S. Ramo, *Currents induced by electron motion*, Proceedings of the I.R.E. (1939) https://doi.org/10.1109/JRPROC.1939.228757.

[37] A. Vilà et al., *Geiger-Mode Avalanche Photodiodes in Standard CMOS Technologies*, (2012) http://dx.doi.org/10.5772/37162.

[38] S. Cova, M. Ghioni, A.L. Lacaita, C. Samori, F. Zappa, *Avalanche photodiodes and quenching circuits for single-photon detection*, Appl. Opt. 35(12), 1956–1976 (1996) https://doi.org/10.1364/AO.35.001956.

[39] G. Vignola, *Time resolution study of SiPMs as tracker elements for the ALICE 3 timing layer*, MSc Thesis, University of Bologna (2021) https://amslaurea.unibo.it/id/eprint/23512.

[40] A. Ghassemi, K. Sato, K. Kobayash, *MPPC*, Hamamatsu Literature, Cat. No. KAPD9005E04 (2022).

[41] F. Acerbi, S. Gundacker, *Understanding and simulating SiPMs*, Nuclear Inst. and Methods in Physics Research, A 926, 16–35 (2019) https://doi.org/10.1016/j.nima.2018.11.118.

[42] A. Gola et al., *NUV-Sensitive Silicon Photomultiplier Technologies Developed at Fondazione Bruno Kessler*, Sensors, 19(2), 308, (2019) https://doi.org/10.3390/s19020308.

[43] C. Piemonte et al., *Performance of NUV-HD silicon photomultiplier technology*, IEEE Trans. Electron Devices, Vol. 63 3 (2016) https://doi.org/10.1109/TED.2016.2516641.

[44] A. R. Altamura, F. Acerbi, C. Nociforo, V. Regazzoni, A. Mazzi, A. Gola, *Characterization of Silicon Photomultipliers after proton irradiation up to* $10^{12} n_{eq}/mm^2$ (2021) https://doi.org/10.1016/j.nima.2022.167284.

[45] A. Duara et al., *Experimental and extraction procedure for the electrical characterisation of silicon photomultiplier detectors*, Nuclear Instruments and Methods in Physics Research Vol. 979 (2020) https://doi.org/10.1016/j.nima.2020.164483.

[46] P. S. Marrocchesi et al., *Charged particle detection with NUV-Sensitive SiPM in a beam of relativistic ions*, IEEE Transactions of Nuclear Science, 61 5 (2014) https://ieeexplore.ieee.org/document/6910334.

[47] N. D'Ascenzo et al., *Silicon avalanche pixel sensor for high precision tracking*, JINST 9 C03027 (2014) https://doi.org/10.1088/1748-0221/9/03/C03027.

[48] F. Gramuglia et al., *Sub-*$10ps$ *Minimum Ionizing Particle detection with Geiger-Mode APDs*, Front. in Phys. 10 849237 (2022) https://doi.org/10.3389/fphy.2022.849237.

[49] TDK Lambda, Z+ Low Voltage Series datasheet (2022) https://product.tdk.com/system/files/dam/doc/product/power/switching-power/prg-power/catalog/z-plus-e-low-voltage-10v-to-100v.pdf.

[50] Keithley *Reference Manual*, Model 6487 Picoammeter/Voltage Source, 6487-901-01 Rev. B (2011) https://download.tek.com/manual/6487-901-01(B-Mar2011)(Ref).pdf.

[51] V. Chmill et al., *Study of the breakdown voltage of SiPMs*, Nuclear Instruments and Methods in Physics Research Section A: Accelerators, Spectrometers, Detectors and Associated Equipment 845 (2017) https://doi.org/10.1016/j.nima.2016.04.047.

[52] Keysight, E4990A Impedance Analyzer datasheet https://www.keysight.com/be/en/assets/7018-04256/data-sheets/5991-3890.pdf.

[53] F. Carnesecchi et al., *Beam test results of* 25 μm *and* 35 μm *thick FBK ultra fast silicon detectors*, arXiv: 2208.05717 (2022).

[54] Teledyne Lecroy Waverunner 9494M-MS datasheet https://teledynelecroy.com/oscilloscope/waverunner-9000-oscilloscopes/waverunner-9404m-ms.

[55] N1470 4CH reversible 8 kV/3 mA (8W) NIM HV Power Supply Module datasheet.

[56] F. Carnesecchi et al, *Understanding the direct detection of charged particles with SiPMs*, (2022) https://doi.org/10.48550/arXiv.2210.13244.

Aknowledgements

Vorrei ringraziare le persone che in questo ultimo anno di Università mi hanno seguita, formata e guidata con estrema gentilezza, dedizione e disponibilità.

Ringrazio innanzitutto la mia Supervisor Prof.ssa Gilda Scioli, per avere creduto in me e avermi permesso di realizzare questo progetto di tesi in un percorso che è cominciato in triennale ed è continuato, sotto la sua fondamentale guida, in magistrale.

Grazie alla mia Co-Supervisor Dott.ssa Francesca Carnesecchi per suo il continuo e importante sostegno di questi mesi.

Vorrei ringraziare il Dott. Rosario Nania per i suoi interessanti suggerimenti e preziosi consigli.

Grazie a D. Cavazza per essere un punto di riferimento in laboratorio, sia professionalmente che personalmente.

Grazie al Prof. Andrea Alici per il suo aiuto, a Bologna e durante gli studi al CERN.

Grazie al Prof. Antonino Zichichi ed alla Prof.ssa Luisa Cifarelli per la loro disponibilità e il fondamentale supporto per i progetti futuri.

Un grazie speciale a Sofia, per i piacevoli confronti e la sua gentilezza unica, e grazie mille a Gianpiero, per il suo grande aiuto e per il tempo che mi ha dedicato.

Vorrei ringraziare poi l'INFN della Sezione di Bologna e tutto il gruppo di ALICE.

Grazie di cuore alla mia famiglia tutta.

Grazie a mia madre Patrizia e a mio padre Marco, per credere in me e sostenermi sempre: siete il mio porto sicuro. Grazie a mio fratello Andrea e la sua compagna Arianna, per le serate immerse nei giochi da tavolo e le tante bellissime passioni condivise. Grazie ai miei nonni Maria, Maris e Antonia, per tutto (e di più). Grazie ai miei zii e ai miei cugini, in particolare a mia zia Paola e a mia cugina Beatrice per il loro sostegno di sempre. Grazie mille alla mia famiglia "di su": Aurora, Alberto, Leonardo (amico e compagno prezioso di studi e di tesi), Lorella e Massimo.

Grazie a tutti i miei più cari amici e amiche, con i quali condivido le più svariate attività e passioni, ai compagni di studi degli ultimi anni, in particolare Davide, e a tutto il gruppo "di Bertinoro": l'amicizia nata con ognuno di voi in questi anni è un dono.

Infine, grazie al mio più fedele compagno di studi, nonchè compagno di vita, Sebastiano. Grazie per festeggiare assieme ogni tipo di conquista, dalla più piccola alle più difficili, e grazie per donarmi serenità e felicità, ogni giorno. "*Abbiamo tutto il tempo... aroma di caffè*"